Computational Intelligence and Neuroscience

Advances in Intelligent Methods for Classification and Diagnosis of Cancer and Brain Disorder Diseases

Lead Guest Editor: Faisal Saeed
Guest Editors: Mohammed Al-Sarem and Tawfik Al-Hadhrami

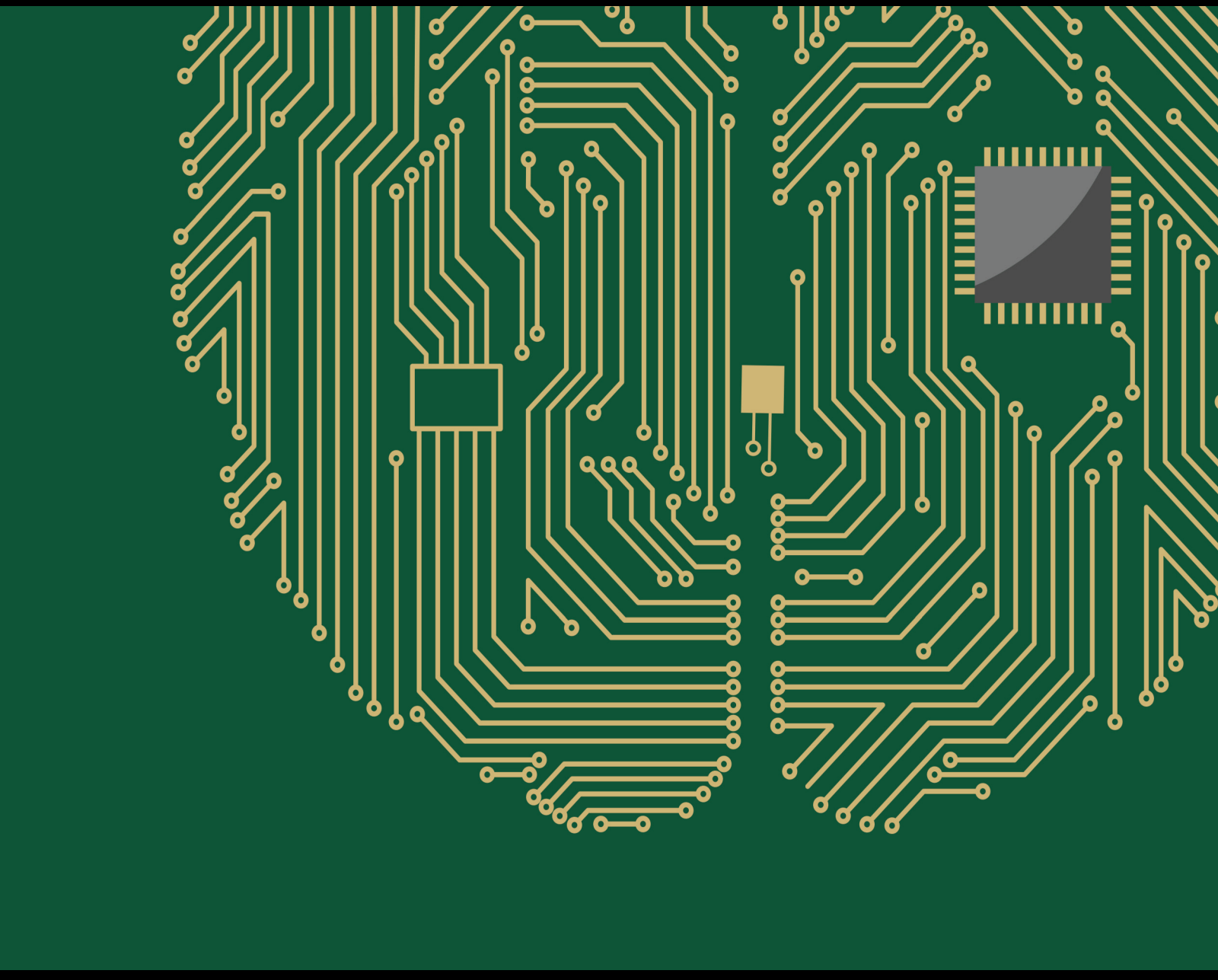

Advances in Intelligent Methods for Classification and Diagnosis of Cancer and Brain Disorder Diseases

Computational Intelligence and Neuroscience

Advances in Intelligent Methods for Classification and Diagnosis of Cancer and Brain Disorder Diseases

Lead Guest Editor: Faisal Saeed
Guest Editors: Mohammed Al-Sarem and Tawfik Al-Hadhrami

Contents

Hindawi
Computational Intelligence and Neuroscience
Volume 2023, Article ID 7282944, 12 pages
https://doi.org/10.1155/2023/7282944

Research Article

Lung Cancer Classification in Histopathology Images Using Multiresolution Efficient Nets

Sunila Anjum,[1] Imran Ahmed,[2] Muhammad Asif,[3] Hanan Aljuaid,[4] Fahad Alturise,[5] Yazeed Yasin Ghadi,[6] and Rashad Elhabob[7]

[1]*Center of Excellence in Information Technology, Institute of Management Sciences, Hayatabad, Peshawar 25000, Pakistan*
[2]*School of Computing and Information Science, Anglia Ruskin University, Cambridge, UK*
[3]*Department of Computer Science, National Textile University, Faisalabad, Pakistan*
[4]*Computer Sciences Department, College of Computer and Information Sciences, Princess Nourah bint Abdulrahman University (PNU), P.O. Box 84428, Riyadh 11671, Saudi Arabia*
[5]*Department of Computer, College of Science and Arts in Ar Rass, Qassim University, Ar Rass, Qassim, Saudi Arabia*
[6]*Department of Software Engineering/Computer Science, Al Ain University, Al Ain, UAE*
[7]*College of Computer Science and Information Technology, Karary University, Omdurman, Sudan*

Correspondence should be addressed to Rashad Elhabob; rashad@karary.edu.sd

Received 19 October 2022; Revised 7 November 2022; Accepted 29 November 2022; Published 16 October 2023

Academic Editor: Tawfik Al-Hadhrami

Histopathological images are very effective for investigating the status of various biological structures and diagnosing diseases like cancer. In addition, digital histopathology increases diagnosis precision and provides better image quality and more detail for the pathologist with multiple viewing options and team annotations. As a result of the benefits above, faster treatment is available, increasing therapy success rates and patient recovery and survival chances. However, the present manual examination of these images is tedious and time-consuming for pathologists. Therefore, reliable automated techniques are needed to effectively classify normal and malignant cancer images. This paper applied a deep learning approach, namely, EfficientNet and its variants from B0 to B7. We used different image resolutions for each model, from 224×224 pixels to 600×600 pixels. We also applied transfer learning and parameter tuning techniques to improve the results and overcome the overfitting problem. We collected the dataset from the Lung and Colon Cancer Histopathological Image LC25000 image dataset. The dataset acquisition consists of 25,000 histopathology images of five classes (lung adenocarcinoma, lung squamous cell carcinoma, benign lung tissue, colon adenocarcinoma, and colon benign tissue). Then, we performed preprocessing on the dataset to remove the noisy images and bring them into a standard format. The model's performance was evaluated in terms of classification accuracy and loss. We have achieved good accuracy results for all variants; however, the results of EfficientNetB2 stand excellent, with an accuracy of 97% for 260×260 pixels resolution images.

1. Introduction

Malignant growth has been described as a combination of related infections, including unusual cell development that continuously spreads into encompassing tissues. Different cancer types can occur in human bodies as per worldwide disease statistics [1]; lung and colon malignancies are among the most common, with lung cancer first in men and third in ladies. Colon malignancy is positioned third in men and second in ladies. The leading causes of lung cancer are tobacco and smoking, whereas the causes of colon cancer are older age, smoking, and regular use of red meat. Lung cancer subtypes are lung adenocarcinoma, lung squamous cell carcinoma, and colon adenocarcinoma [2], identified by histopathology, which studies tissues using a microscope. A histopathology report is called a biopsy report, in which the doctor identifies subtypes of cancer and their stage. The characteristics and treatments of different pathologic subtypes of cancer are dissimilar. Nevertheless, the right and on-time prognosis can execute a compelling treatment design and draw outpatient endurance.

Computer-aided diagnosis (CAD) systems can be a helpful tool for avoiding misclassification [3]. The CAD gives a modernized yield as a "second assessment" to help a pathologist's findings and helps clinical technologists and pathologists to assess malignancies more precisely. Artificial intelligence approaches have improved the precision and computerization of histopathologic slide examination. Convolutional neural networks (CNNs) are presently the best method to assemble dynamic work processes in computerized pathology [3]. When a given CNN model is adequately trained on labelled image information, it takes complex histological features from pictures through deconvolution of the picture content, which has many features and afterwards perceives these features in inconspicuous pictures. Any basic CNN model is based upon convolutional filters, pooling, and fully connected layers. Different hidden layers of CNN give various picture details level information to detect complex features.

The major goal of this work is to categorize lung and colon cancer biopsy images into five classes with subtypes of lung adenocarcinoma, squamous cell carcinoma, normal tissues, colon adenocarcinoma, and colon normal tissues using the EfficientNet model to observe the effect of the CNN model when image resolution is increased. For classifying any CNN model, a large dataset is usually required. Our chosen dataset consists of twenty-five thousand images with five classes, but it is not enough. CNN architecture faces the problem of overfitting due to the small size of the dataset. Pretrained models with fine turning can be used to prevent overfitting issues and computing power. The whole dataset is divided into three phases, training, validation, and testing, for the experiment. In this work, CNN architecture with pretrained EfficientNet variants EfficientNetB0–B7 has been used to classify into five classes for lung and colon cancer histology images.

1.1. Objectives and Contribution of the Proposed Work. The major contribution of this research work is as follows:

(1) To classify histology images into three classes of lung cancer and two classes of colon cancer with high accuracy

(2) To avoid overfitting problems and train the model with limited available resources, pretrained models with fine-tuning and transfer learning techniques are used to classify images into five categories correctly

(3) To find the model's effectiveness by increasing the resolution correspondingly, different variants of EfficientNet from B0 to B7 are trained, with each model having a different image resolution (from 224×224 pixels increased to 600×600 pixels).

(4) To make a comparison among the proposed model and variants of EfficientNet

The related work is briefly discussed in Section 2. Section 3 discusses the Materials and Methods. Results and Discussion are elaborated in Sections 4 and 5, followed by conclusion and future directions in Section 6.

2. Related Work

Various works have been found in the literature to detect, segment automatically, and classify cancerous and noncancerous from histopathology images using machine learning and deep learning techniques. Deep learning is the most recently used technique for classification tasks due to its accuracy and automatic selection of the best features. Barker et al. [4] proposed a method for cerebrum tumours in entire slide computerized pathology pictures. Ojansivu et al. [5] researched the grouping of bosom disease from histopathological images. In [6], the authors investigated different resolutions EfficientNets for sore skin grouping, joined with broad data increase, and balancing loss and considered multiresolution a significantly important parameter for the model.

In [7], the authors proposed and assessed a convolutional neural network to arrange interstitial lung infection disease patterns. The proposed network comprises five convolutional layers with two parts and Leaky ReLU, trailed by average pooling with a size equivalent to the size of the last component guides and three deep layers. In [8], lung cancer pathology subtypes are classified in CT scan images using a deep residual neural network with transfer learning techniques which achieved 85% of accuracy. In [9–12], researchers applied different models to classify lung cancer types or lung cancer from noncancer images with various deep learning models and tried to increase the model's accuracy using other datasets. Iizuka et al. [13] used the inception v3 model and the recurrent neural network to classify stomach and colon biopsy histopathology from whole slide images. The model was trained to classify adenocarcinoma, adenoma, and nonneoplastic. In addition, the authors added regularization methods and different augmentation techniques to make the algorithm more robust. Rathore et al. [14] used an SVM classifier to examine colon cancer of histopathology images in normal and malignant tissue.

The proposed approach [15] was tried on a histopathological dataset for colorectal malignancy order in light of seven sorts of CNNs. Scaling up CNN models is broadly used to improve accuracy [16]. The most basic route is the scale-up CNN model by depth [17]; these networks are simpler to advance and can acquire precision from an impressively expanded depth or scale model through width [18]. Another more uncommon, however, progressively mainstream technique is scaling up models by increasing the size of images [19]. The EfficientNet model [16] addresses all three scaling methods named compound scaling. However, the model needs more layers to build the open field and channels to catch all the fine-grained designs on the larger picture for the larger input image size. Moreover, increasing image resolution [20] compromises the largest conceivable batch size for CNN training. After reviewing the literature, this paper presented a method to classify the colon and lung histopathology images using all variants of the EfficientNet model (from B0 to B1), increasing the image resolution up to 600×600 pixels.

3. Materials and Methods

This section explains our proposed methodology, experiment, and dataset used to classify lung and colon histopathology images using EfficientNet Model variants from B0 to B7.

3.1. Images Dataset Acquisition. The dataset used in this research is taken from the Lung and Colon Cancer Histopathological Image LC25000 image dataset [21], which consists of 25,000 images with two subfolders: colon cancer folders containing 10,000 images and lung cancer folders with 15,000 images. All images are in JPEG format and are 768×768 pixels in size. The lung cancer folder contains three subfolders with two lung cancer types and benign lung tissue images. From histopathology images, cancerous and noncancerous can be identified as follows:

(1) Malignant tissue: It can be identified as dark in colour and abnormal nuclei tissue growth compared to its normal tissue image, as shown in Figure 1.

(2) Benign tissue: This region has normal growth of tissues and is light in colour.

Three functions are applied to augment the images, as explained in [21]; the first function is rotated randomly between 25% on the right and 25% on the left. The second function adds random noise to the images, and the third function is horizontal flips, which flips the image array of pixels. Using these augmentation functions, the images in the dataset are expanded for lung cancer images up to 15,000. So, in this research, the five classes, lung adenocarcinoma, lung squamous cell carcinomas, benign lung tissue, colon adenocarcinoma, and colon benign tissue, are considered to be classified. Each class contains 5,000 images. The same for colon images; make 10,000 images, each of the two categories having 5,000 images.

3.2. Preprocessing. In the preprocessing phase, we have to ensure that all images are equal in size for the best result of the CNN model. In the first step, all images are in 768×768 pixels, as shown in Figure 2. We adjusted the image resolution size as required for each EfficientNet model variant according to Table 1. As for EfficientNetB0, convert all images into equal sizes of 224×224 pixels for all training, validation, and testing stages. To avoid the imbalanced problem [22], the classification of classes is not balanced; that is, one class has more images than all other classes, so we must have an equal number of images in each class. That is why each class has an equivalent of 5,000 images in our dataset. A straightforward way to deal with surviving class irregularities in model learning is to resample the training data (a premeasure).

The whole dataset is divided for the CNN model's training, validation, and testing phases in the second step. To avoid the overfitting problem (which means not having enough data in the training phase that the model does not correctly predict the classes) and for the best accuracy results, more images are kept in a training folder of 25,000 images, 15,000 images belonging to 5 categories (colon adenocarcinoma, benign colon tissue, lung adenocarcinoma, lung benign, and lung squamous cell carcinoma). In the validation folder, we allocate 5000 images belonging to 5 classes and assign 5000 images belonging to 5 classes for testing. In the third and last step of the preprocessing phase, we make sure that all images in subfolders are correctly labelled; all images in the colon adenocarcinoma folder are labelled as "colonca1" 1 represents the number of an image, and in the same way, all images in a colon benign tissue folder are marked as "colonn1". Also, all images in three classes of lung folders are differently labelled (lungaca1, lungn1, and lungscc1); this helps our model in the ImageDataGenerator phase to train and generate labels for the training phase.

3.3. Transfer Learning. Transfer learning is a mainstream approach in computer vision-related problems; hence, we combined the pretrained models with the newly trained layer of CNN architecture. Here, we are using a deep learning pretrained EfficientNet model, where the last layer of the model performs as input data to another classifier. In addition, we utilized the ImageNet dataset for transfer learning techniques for classification, which helped us achieve better performance accuracy and saved training time. Figure 3 shows the schematic diagram for transfer learning. It can be seen that the previous model that was trained on source data is combined with the newly trained target data model with the help of transfer learning.

3.4. Proposed CNN Method. This section explains our proposed work for classifying lung and colon cancer into five classes (lung benign, lung adenocarcinomas, lung squamous cell carcinomas, colon adenocarcinomas, and colon benign), as shown in Figure 4. Transfer learning on the ImageNet dataset and the fine-tuning method means adjusting each model's last layers to achieve good accuracy and performance. The whole dataset is divided into three portions, where 80% of the data is used for training, 10% for validation, and 10% for testing. EfficientNet with different variants from B0 to B7 is used. Similar size images are used for each model, as mentioned in Table 1, so we first resize it into 224×224 pixels for EfficientNet B0 and the same for other models. After preprocessing and training, the model results are evaluated.

3.5. EfficientNet and Variants. The EfficientNet models [16] depend on straightforward and compelling compound scaling strategies. EfficientNets are a group of neural organization structures delivered by Google in 2019, planned by an enhancement methodology that amplifies the precision for a given computational expense. EfficientNets are suggested for characterization errands. They beat numerous organizations (such as DenseNet, Inception, and ResNet) on the ImageNet benchmark while running quicker. This strategy empowers the scaling up of a benchmark ConvNet to any objective asset imperative while maintaining model

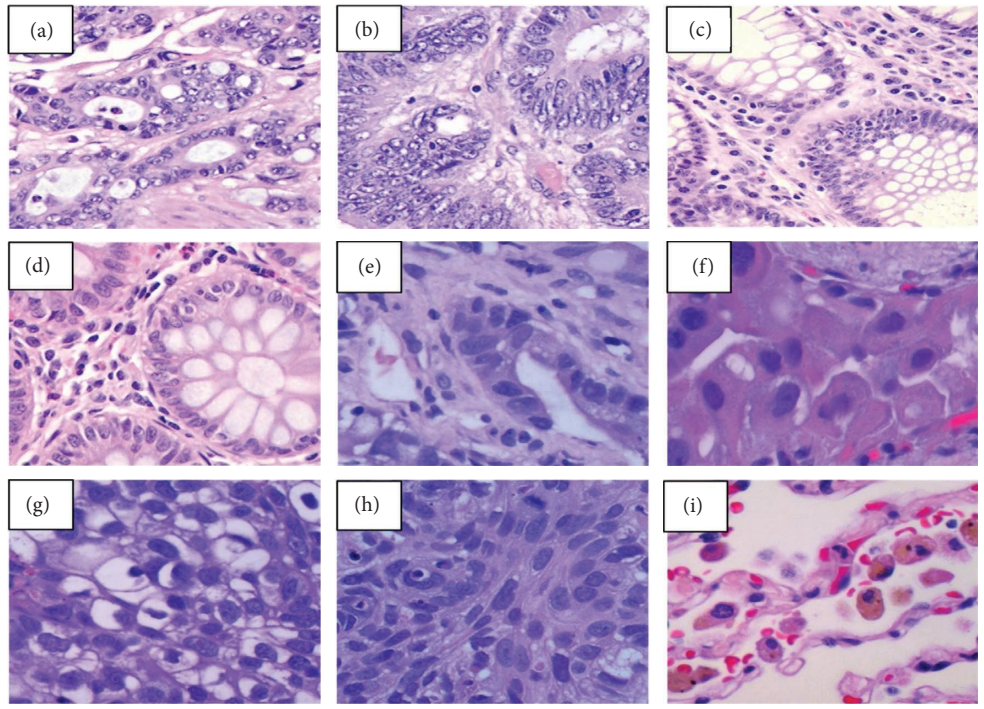

Figure 1: Image samples from LC25000 dataset image. (a, b) Colon adenocarcinoma. (c, d) Colon benign tissue. (e, f) Lung adenocarcinoma. (g, h) Lung squamous cell carcinomas. (i) Benign lung tissue.

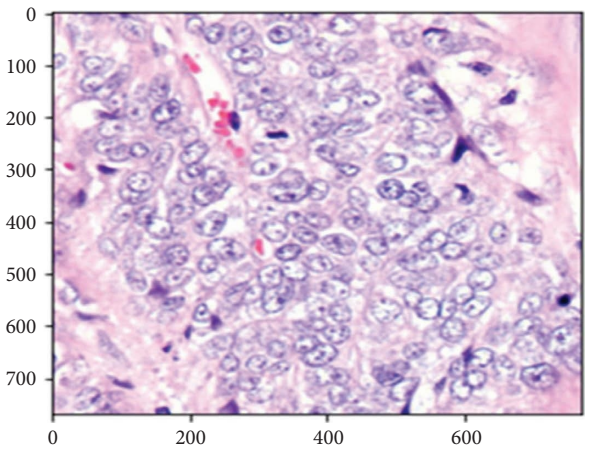

Figure 2: Index representation of the dataset image sample before preprocessing to the model's desired size.

Table 1: Different image resolutions used for each model.

Base model	Resolution
EfficientNetB0	224 × 224
EfficientNetB1	240 × 240
EfficientNetB2	260 × 260
EfficientNetB3	300 × 300
EfficientNetB4	380 × 380
EfficientNetB5	456 × 456
EfficientNetB6	512 × 512
EfficientNetB7	600 × 600

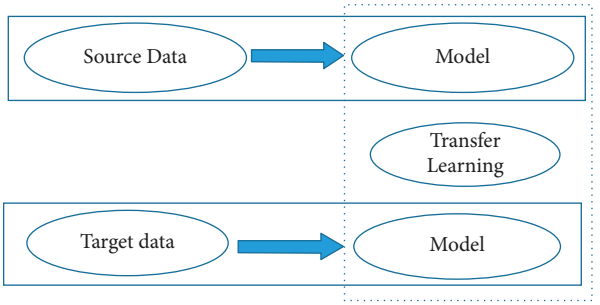

Figure 3: Transfer learning schematic diagram.

proficiency, which is utilized for moving learning datasets. As a rule, EfficientNet models accomplish higher precision and better productivity over existing CNNs, for example, AlexNet, ImageNet, GoogleNet, and MobileNetV2. Specifically, EfficientNet explores the focal inquiry: is there a standard technique to scale up ConvNets to accomplish better exactness and productivity? In this model, observational investigation, as shown in Figure 5, is essential to adjust all measurements of organization width (more filters in the layer), depth (more layers), and resolution (more $H * W$); such equilibrium can be accomplished by essentially scaling each of them with steady proportion. This model is a basic yet powerful compound scaling strategy in light of this perception. Unlike all traditional models that scale any of these elements, our approach consistently scales network width, depth, and resolution with a bunch of fixed scaling coefficients.

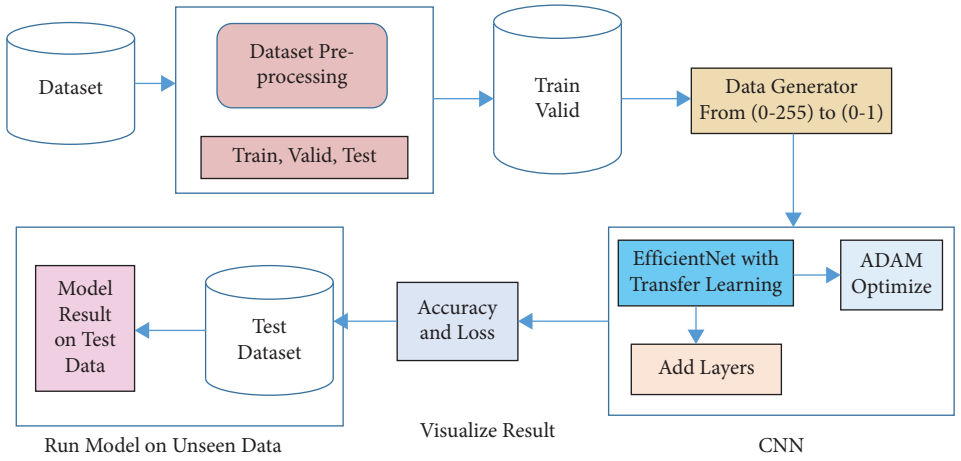

Figure 4: Block diagram of the proposed work.

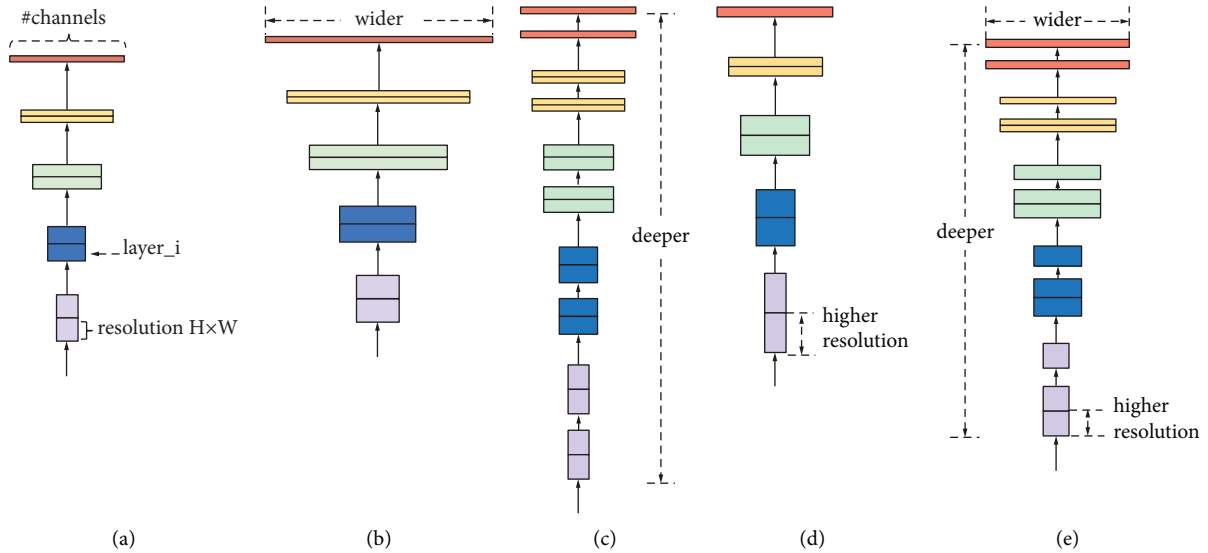

Figure 5: The basic idea of EfficientNet [16] is to carefully balance scale, the network width depth, and resolution if resources are available (https://ai.googleblog.com/2019/05/efficientnet-improving-accuracy-and.html).

A ConvNet Layer I can be characterized as a capacity:

$$Y_i = F_i(X_i), \tag{1}$$

where F_i is the operator, Y_i is the yield tensor, and X_i is the input tensor with a tensor shape (H_i, W_i, C_i), where H_i and W_i are the spatial measurements and Ci is the channel measurement. A rundown of created layers can address a ConvNet N:

$$N = F_k \odot \ldots \odot F_1 \odot F_1(X_1) = \odot J_j = 1 \ldots kF_j(X1). \tag{2}$$

The network scales the existing baseline ResNet model as described in the following equation:

$$N = \overset{\odot}{}_{i=1\ldots s} f_i^{L_i}\left(X_{(H_i W_i G_i)}\right), \tag{3}$$

where $f_i^{L_i}$ denotes layer f_i is repeated L_i times in stage $i$and $(H_i W_i G_i)$ indicates the shape of the input tensor X of a layer. Different variants of EfficientNet are available from B0 to B7. Each variant is scaled up to increase all three elements (depth, width, and resolution) from the previous one to see the model result in terms of accuracy and computational cost. Each number addresses variants with more parameters and higher accuracy, and the processing power generally increases for each addition. Attempt EfficientNetB0 first since its exactness is comparable to different networks while being absurdly quick to run and train. If you need to improve your outcomes, take a stab at utilizing greater and greater sizes of the EfficientNet design (B1⟶, B2⟶, B3⟶, and so on) until you hit the most elevated exactness for your information. Each model was pretrained on the ImageNet dataset Top1 and Top5 accuracy in Table 2.

4. Experiments

In this paper, we adopt the method to explicitly preserve the previous convolution and pooling layers, in which the model parameters of the record stacked on the dataset of ImageNet

Table 2: Top5 and Top1 accuracy of models trained on the ImageNet dataset.

Model variants	Parameters (m)	Top1 accuracy %	Top5 accuracy %
EfficientNetB0	5.3	76.3	92.3
EfficientNetB1	7.8	78.8	94.4
EfficientNetB2	9.2	79.8	94.9
EfficientNetB3	12	81.1	95.5
EfficientNetB4	19	82.6	96.3
EfficientNetB5	30	83.3	96.7
EfficientNetB6	43	84.0	96.9
EfficientNetB7	66	84.4	97.1

are pretrained to introduce the new network. Furthermore, the pretrained model carried out a new job by using parameters, fully associated layers, and Softmax activation function in combination with turning the last layers of the model using fine-tuning methods for each model to improve the accuracy and decrease loss. Thus, the network construction could adjust to the new characterization task in this manner, speeding and simplifying the learning effectiveness of the model and upgrading the inference capacity.

We have utilized all EfficientNet variants from B0 to B1 models for the transfer learning measure and added a batch normalization layer. Batch normalization incredibly speeds up the training of deep networks and builds the stability of the neural model [23] to limit overfitting by reducing the all-out number of parameters. Moreover, after flattening the layer, two dense inward layers with RELU activation function having 512 neurons to activate (change activates several neurons for each model) and dropout layers have been added. A 30% dropout rate has been picked randomly to overcome overfitting. At last, one dense output layer contains five output units for multiclass order to classify five classes of our dataset. Softmax implementation has been added to the proposed automatic finding framework.

We give input shape 224×224 size to the EfficientNetB0 model in which the dataset is divided into three parts. The training set consists of 20,000 images for five classes; validation consists of 2500; and the testing set also has 2500 images and then initializes weight as ImageNet. We keep the batch size minimum as the model takes minimum training time. Therefore, the batch size is set to 30 for the training and validation path. We change the resolution in every model as variants improve from the previous model and change the resolution size to check the model's performance efficiency.

4.1. Parameter Adjustment. Parameter adjustment incredibly affects the exhibition of the model since they straightforwardly administer the model's training. Also, fine-tuning can avoid overfitting and the structure of a summed-up model. Therefore, in our study, for the correct classification of lung and colon cancer histology images into five classes, a more effective CNN pretrained model, EfficientNet, is chosen. Our proposed method for this model consists of two parts.

(1) First, we download and import EfficientNet and then specify the model variants.

(2) Fine-tuned, fully connected layers.

In the first step, variants of EfficientNet (EfficientNetB0, EfficientNetB1, EfficientNetB2, EfficientNetB3, EfficientNetB4, EfficientNetB5, EfficientNetB6, and EfficientNetB7) are added with setting weight to ImageNet. In the fully connected layer (FCL), "Softmax" is used as an activation function. The reason for using Softmax is that the classification is categorical.

One major problem we faced during training the model was that training accuracy was not good and loss also increased. To overcome this, the last layer's parameters are adjusted to improve accuracy. The parameters are turned accordingly; when the model gives us more loss than accuracy in some variants, the dropout function is increased, in this way, the overfitting problem is reduced, and loss is decreased.

4.2. Implementation Details. All models are trained for 100 epochs using Adam. Categorical cross-entropy is used for the loss function in multiclass classification, one class in many possible categories. Batch size and learning rate are received depending on every network's GPU memory necessities. All the software and libraries utilized in the proposed work are open source. The perusers should use Google Colab Notebook to replicate the outcomes using the GPU run time. This product can be used without costs, since Google gives it to explore exercises utilizing a Tesla K80 GPU of 12 GB. The EfficientNet models are pre-prepared, scaled CNN models that can be used for transfer learning in picture characterization issues. The model was created by Google AI in May 2019 and is accessible through GitHub vaults. This work has been performed using Python. The neural network library "Keras" develops, compiles, and assesses the proposed methodology. The Python programming language rendition 2.7 (counting libraries, for example, numpy, cv2, pandas, and matplotlib) was utilized for all parts of this undertaking. The model was trained and tested on the framework of the window. The performance can also depend on how many medical images are loaded for training and validation.

5. Results and Discussion

To assess the model's performance, as per the attributes of the network model, the accuracy rate and loss rate are utilized as the evaluation measures. The normal exactness of the model is characterized as follows [24]:

$$\text{Accuracy} = \frac{R_A}{R} * 100. \tag{4}$$

In (4), R represents the total number of images in the training and validation phase, and R_A represents correctly classified images. The model runs for 100 epochs, with seven iterations for training and three for validation in each epoch to improve the model performance. As in the start of model training, the validation loss and training loss value is high, 40

Table 3: The model evaluation results in terms of classification loss and accuracy.

Efficient net variants	Training		Validation		Testing		Model training time
	Accuracy	Loss	Accuracy	Loss	Accuracy	Loss	
B0	0.95	0.37	0.93	0.37	0.96	0.34	09 minutes
B1	0.96	0.11	0.96	0.06	0.96	0.11	08 minutes
B2	0.97	0.07	0.07	0.97	0.97	0.07	07 minutes
B3	0.95	0.18	0.95	0.08	0.95	0.18	3 hours 17 minutes
B4	0.96	0.11	0.14	0.94	0.11	0.96	2 hours 33 minutes
B5	0.94	0.33	0.93	0.20	0.95	0.28	36 minutes
B6	0.93	0.22	0.96	0.21	0.94	0.47	2 hours 45 minutes
B7	0.95	3.05	0.92	2.79	0.95	2.75	54 minutes

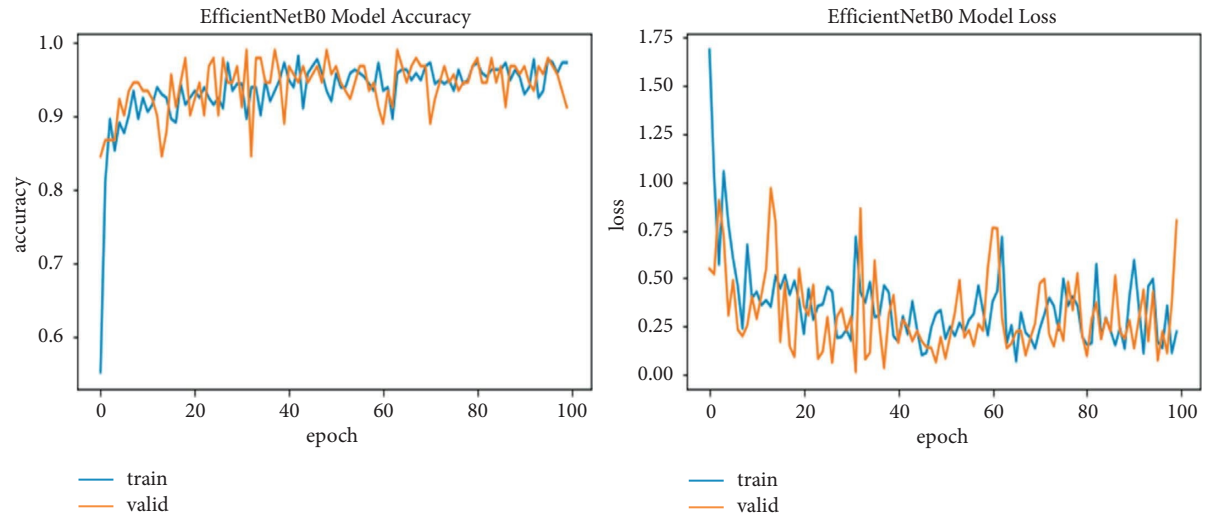

Figure 6: EfficientNetB0 training and validation plot of accuracy and loss.

or 50%, and then gradually decreases in each epoch. The result of every model is described in Table 3. Training results for EfficinetNetB0 are 95% accuracy and 0.37 loss, having 224×224 image resolution; EfficinetNetB1 is 96% accuracy and 0.11 loss for 240×240 image size; EfficinetNetB2 is 97% accuracy and 0.07 loss for having 260×260 resolution; for B3, B4, B5, B6, and B7 accuracies are 95, 94, 93, and 95% and losses are 0.18, 0.33, 0.22, and 3.05, increasing the image resolution. So, from this result, we can say that the B2 model gives us good accuracy with less loss, and image resolution is also not very minimal. B6 and B7 also have good results in terms of their image resolution size and effectiveness in being run with a Colab GPU in less time than other studies that take days to train on this resolution size and have some good physical hardware attached to the GPU.

We explore all variants of efficient models for different image resolutions for the classification of lung and colon histopathology images into five classes (colon adenocarcinoma, benign colon tissue, lung adenocarcinoma, lung benign, and lung squamous cell carcinomas). In previous studies, these model variants were not explored for histopathology image classification, and we consider that input resolution is an important parameter that was not considered in previous studies. For a long time, small image sizes have been considered for convolutional neuron network models to increase model performance effectively. A similar study [6] increased input resolution to 528×528 pixels, and we increased it to 600×600 pixels. When the image resolution increases, more features are extracted with more fine details than fewer resolution images (as the visualization graph from B0 to B7 is shown in Figures 6–13). Our results predict that by increasing the input size, the performance does not decrease. Still, the loss is a little bit high for low-resolution sizes. Validation loss rates for B7 drop from 52.51%, 5.11%, and 2.55% after 1, 30, and 99 epochs. But this loss can also be overcome with the availability of increased memory and computation power for running more epochs.

The other measure we consider for evaluating these models' performance is the time taken to train a model for 100 epochs. The time taken by each model depends upon the Internet speed and the availability of the GPU in Colab. Sometimes the Colab is not assigning GPU to our notebook or cannot connect with the host, so we run it without GPU, and it takes many hours to train the model. Convolutional neural organizations (CNN) are neural organizations that are especially fit for picture classification. It has been, for instance, effectively utilized for picture classification orders [25–27]. A typical CNN design contains convolutional, pooling, and completely associated layers. Moderately novel procedures, for example, batch standardization [23],

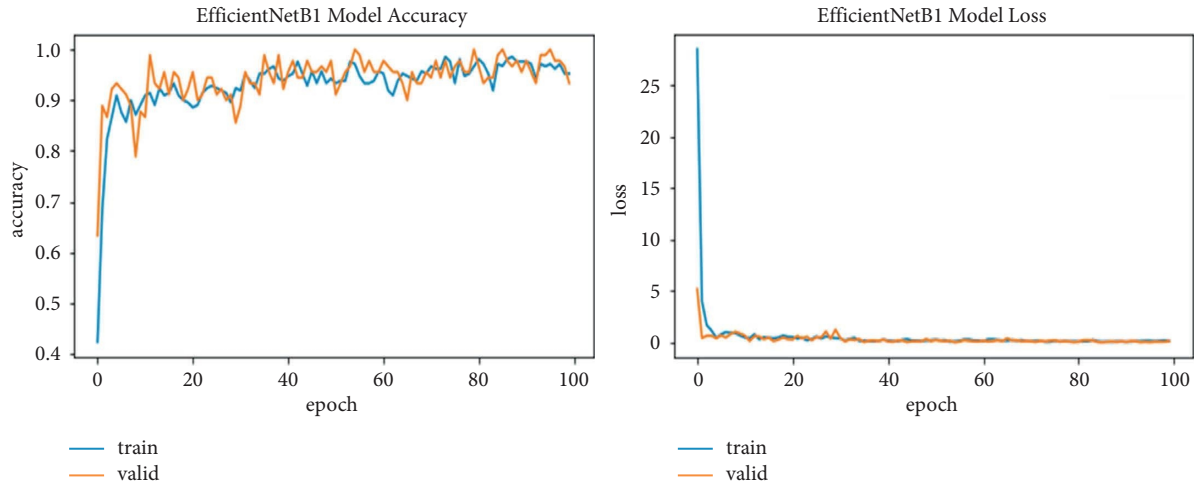

Figure 7: EfficientNetB1 training and validation plot of accuracy and loss.

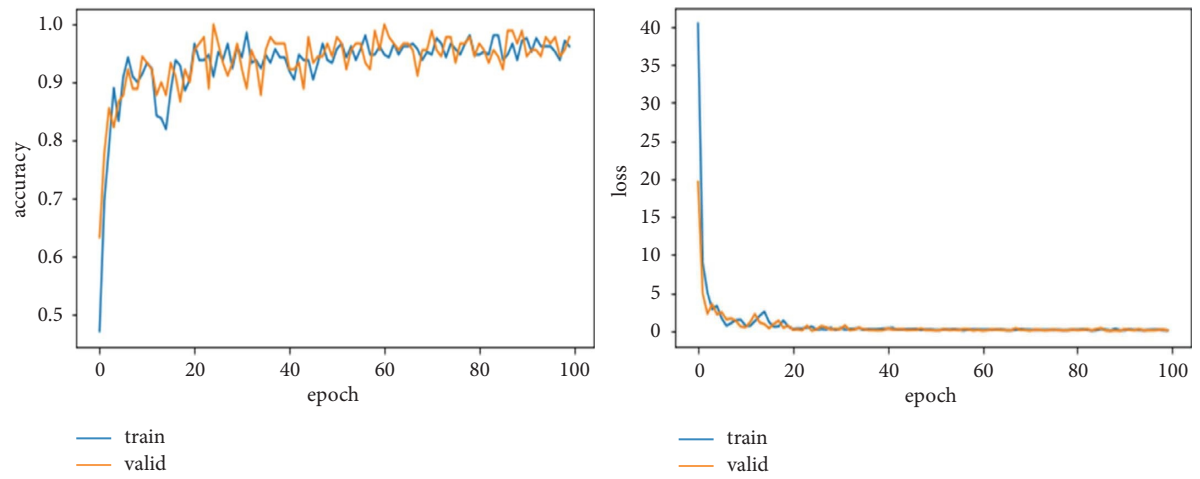

Figure 8: EfficientNetB2 model training and validation plot of accuracy and loss.

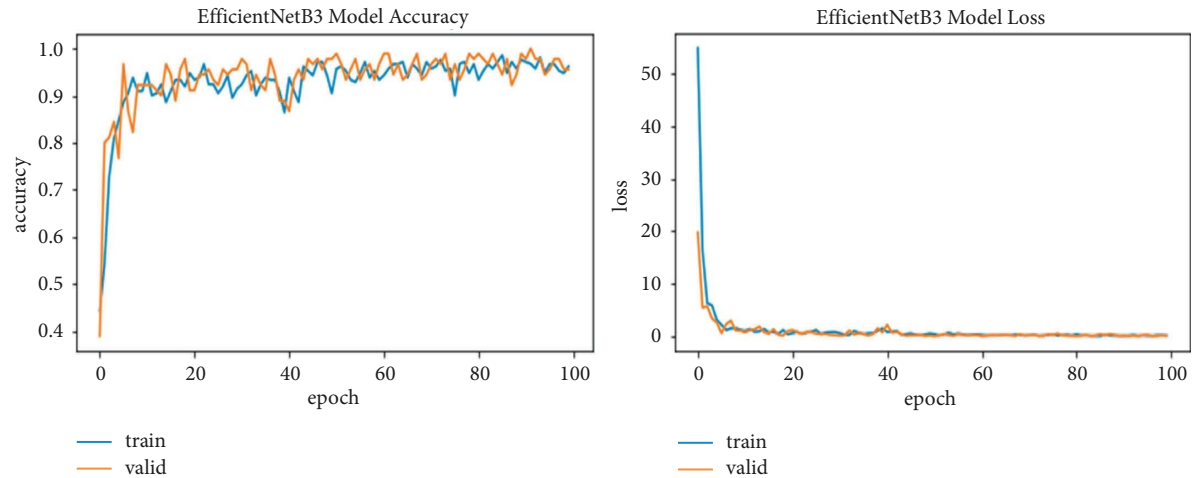

Figure 9: EfficientNetB3 model training and validation plot of accuracy and loss.

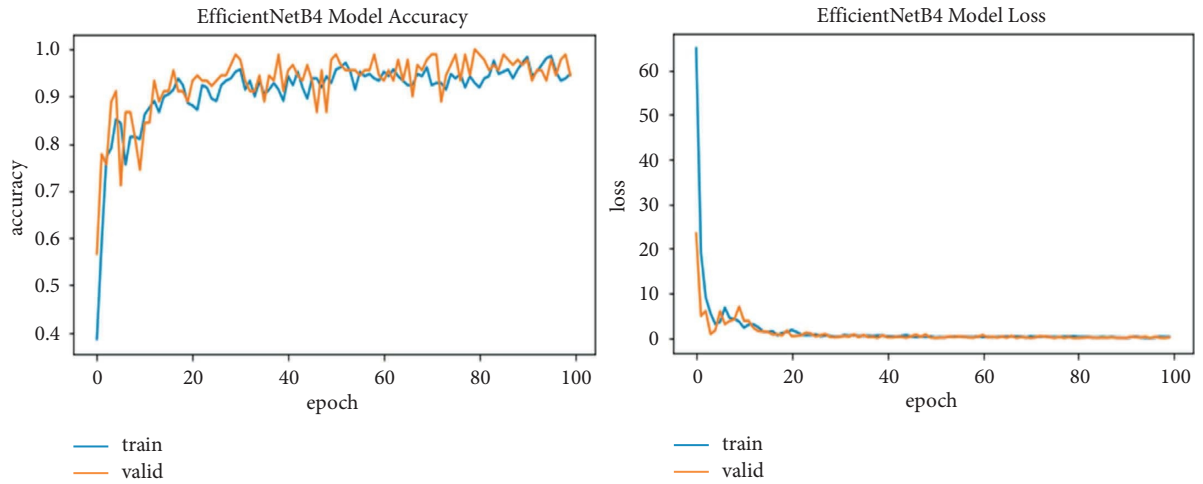

Figure 10: EfficientNetB4 model training and validation plot of accuracy and loss.

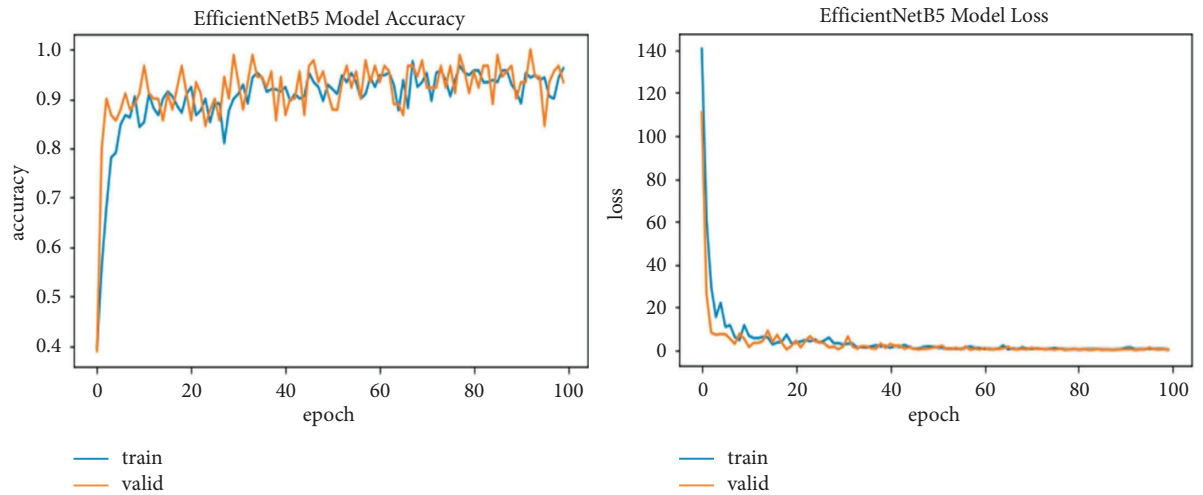

Figure 11: EfficientNetB5 model training and validation plot of accuracy and loss.

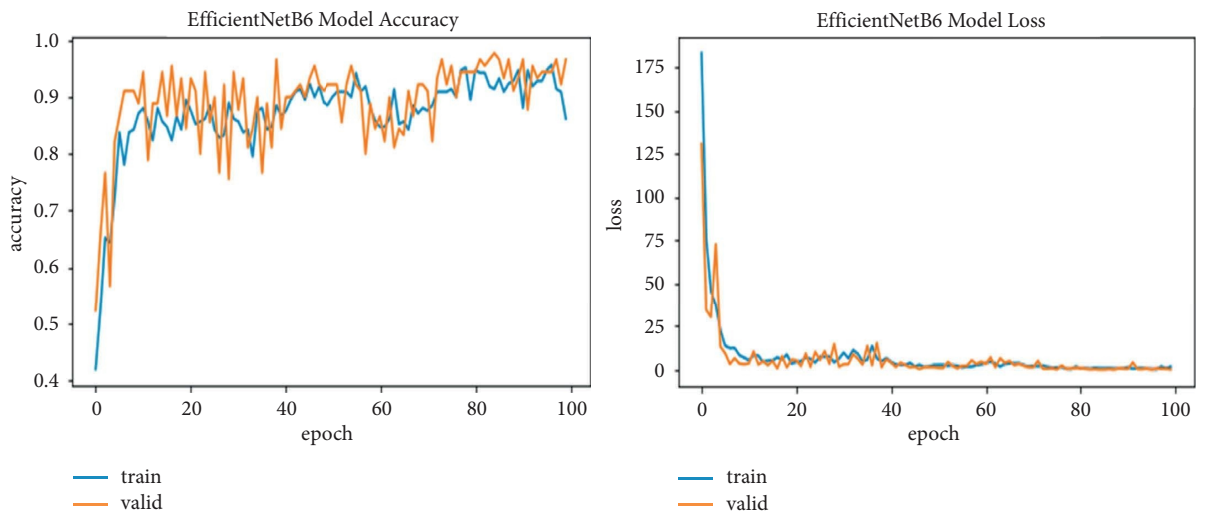

Figure 12: EfficientNetB6 model training and validation plot of accuracy and loss.

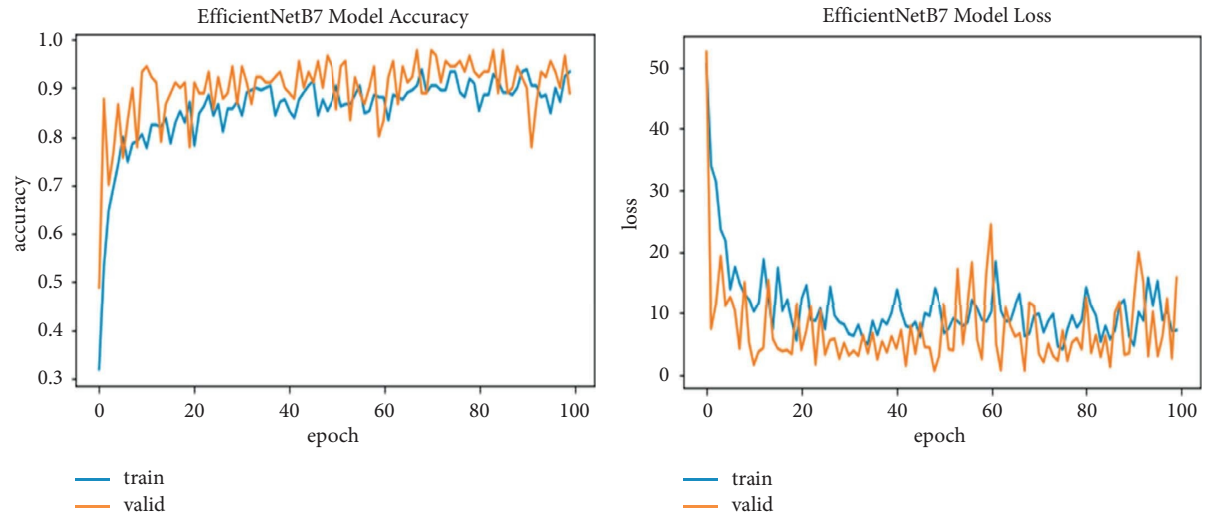

Figure 13: EfficientNetB7 model training and validation plot of accuracy and loss.

Table 4: Comparison with state-of-the-artwork.

Architectures	Parameters	Input size	Classification	Accuracy result (%)
EfficientNetB4 [29]	17 million	Not specified	Binary and multiclass for COVID-19 diagnosis	96
DCNN [3]	60 million	256 × 256	Three classes of lung cancer subtypes	71.1
Residual neural network [8]	0.27 million	50 × 50	Lung cancer type from CT scan images	85.71
Inception-v3 [13]	23 million	512 × 512	Gastric and colonic from histopathological	96
SC-CNN [30]	Not specified	27 × 27	Nuclei in colon cancer histology images	68
EfficientNetB2 (our approach)	9.2 million	260 × 260	For histopathology images of lung and colon cancer (five classes)	97.24

dropout [28], and alternate way associations [17], can, moreover, be utilized to build classification precision. In light of the outcomes, we see that the EfficientNet models, all variants with transfer learning methods, yield better results than the previous model with a simple minimum image size and many other classifier models in calculating malignancy expectation. However, on-time and accurate prognoses are challenging because of the malignancy's intricacy and high mortality. Accordingly, improving the forecast exactness by applying computer-aided diagnosis methods is very helpful for malignancy treatment.

5.1. Comparison with State-of-the-Artwork. In Table 4, EfficientNet variants B2 are compared with the published state-of-the-art methods used for lung and colon classification of histopathology images to prove the superiority of our approach. The EfficientNet model gives good accuracy for maximum resolution and has a minimum number of parameters compared to other models. In the literature, no one attempts to classify the lung and colon cancer images accurately [29]. In [27], the authors classified COVID-19 from X-ray pictures using EfficientNetB4, which can categorize binary and multiclass data. The deep convolutional neural network [3, 31, 32] has 60 million parameters to classify lung cancer subtypes (adenocarcinoma, squamous cell carcinoma, and small cell carcinoma), and we classify five classes. Reference [3] built up a mechanized characterization plot for cellular breakdowns in the lungs using microscopic images to utilize a deep convolutional neural organization (DCNN), an effective deep learning method. The DCNN utilized for grouping comprises three convolutional layers, three pooling layers, and two completely associated layers. Therefore, from these studies, we can say that our model result efficiently classifies the cancer images.

6. Conclusion and Future Work

Contrasted and shallow learning techniques, deep learning has numerous focal points in dissecting pathology images, including clarification of feature definition, power in perceiving complex objects, efficiency through equal calculation, and reasonableness for transfer learning. This paper has tested the EfficientNet model for all variants to classify lung and colon cancer histopathology images. This model aims to scale a CNN model in not just one element but in all three features, namely, depth, width, and resolution, according to available resources in a principled way. This is the first study considering lung and colon image classification and the pretrained EfficientNet model. All variants with different resolutions started at 224 × 224 in the B0 model and increased to 600 × 600 in the B7 model. Each model's last layer is adjusted for better performance, and different dropouts prevent overfitting. The experiment was performed on the LC25000 dataset, having lung and colon images of five

classes. The classification accuracy for training the models B0, B1, B2, B3, B4, B5, B6, and B7 are 95.87, 96.26, 97.24, 95.63, 96.83, 94.31, 93.76, and 95.59%. Our model performed well in terms of training time and computational power. We run our model in the minimum time on a personal computer utilizing Google Colab using GPU without accessing a physical GPU attached to the computer. We plan to extend the work by experimenting with more images of different sizes. We also intend to increase the number of classes based on the availability of the data, which may lead to an increase in the accuracy of the model.

Data Availability

Data are available upon reasonable request to the corresponding author.

Conflicts of Interest

The authors declare that they have no conflicts of interest to report regarding the present study.

Acknowledgments

This research was funded by Princess Nourah bint Abdulrahman University Researchers Supporting Project number (PNURSP2022R54), Princess Nourah bint Abdulrahman University, Riyadh, Saudi Arabia.

References

[1] F. Bray, J. Ferlay, I. Soerjomataram, R. L. Siegel, L. A. Torre, and A. Jemal, "Global cancer statistics 2018: GLOBOCAN estimates of incidence and mortality worldwide for 36 cancers in 185 countries," *CA: A Cancer Journal for Clinicians*, vol. 68, no. 6, pp. 394–424, 2018.

[2] S. Hong, Y. Mok, C. Jeon, S. H. Jee, and J. M. Samet, "Tuberculosis, smoking and risk for lung cancer incidence and mortality," *International Journal of Cancer*, vol. 139, no. 11, pp. 2447–2455, 2016.

[3] A. Teramoto, T. Tsukamoto, Y. Kiriyama, and H. Fujita, "Automated classification of lung cancer types from cytological images using deep convolutional neural networks," *BioMed Research International*, vol. 2017, Article ID 4067832, 6 pages, 2017.

[4] J. Barker, A. Hoogi, A. Depeursinge, and D. L. Rubin, "Automated classification of brain tumor type in whole-slide digital pathology images using local representative tiles," *Medical Image Analysis*, vol. 30, pp. 60–71, 2016.

[5] V. Ojansivu, N. Linder, E. Rahtu et al., "Automated classification of breast cancer morphology in histopathological images," *Diagnostic Pathology*, vol. 8, no. S1, pp. 1–4, 2013, September.

[6] N. Gessert, M. Nielsen, M. Shaikh, R. Werner, and A. Schlaefer, "Skin lesion classification using ensembles of multi-resolution EfficientNets with meta data," *MethodsX*, vol. 7, Article ID 100864, 2020.

[7] M. Anthimopoulos, S. Christodoulidis, L. Ebner, A. Christe, and S. Mougiakakou, "Lung pattern classification for interstitial lung diseases using a deep convolutional neural network," *IEEE Transactions on Medical Imaging*, vol. 35, no. 5, pp. 1207–1216, 2016.

[8] S. Wang, L. Dong, X. Wang, and X. Wang, "Classification of pathological types of lung cancer from CT images by deep residual neural networks with transfer learning strategy," *Open Medicine*, vol. 15, no. 1, pp. 190–197, 2020.

[9] K. H. Yu, C. Zhang, G. J. Berry et al., "Predicting non-small cell lung cancer prognosis by fully automated microscopic pathology image features," *Nature Communications*, vol. 7, no. 1, p. 12474, 2016.

[10] S. Wang, T. Wang, L. Yang et al., "ConvPath: a software tool for lung adenocarcinoma digital pathological image analysis aided by a convolutional neural network," *EBioMedicine*, vol. 50, pp. 103–110, 2019.

[11] J. W. Wei, L. J. Tafe, Y. A. Linnik, L. J. Vaickus, N. Tomita, and S. Hassanpour, "Pathologist-level classification of histologic patterns on resected lung adenocarcinoma slides with deep neural networks," *Scientific Reports*, vol. 9, no. 1, pp. 3358–8, 2019.

[12] Z. Li, Z. Hu, J. Xu et al., "Computer-aided diagnosis of lung carcinoma using deep learning-a pilot study," 2018, https://arxiv.org/abs/1803.05471.

[13] O. Iizuka, F. Kanavati, K. Kato, M. Rambeau, K. Arihiro, and M. Tsuneki, "Deep learning models for histopathological classification of gastric and colonic epithelial tumours," *Scientific Reports*, vol. 10, no. 1, pp. 1504–1511, 2020.

[14] S. Rathore, M. Hussain, M. Aksam Iftikhar, and A. Jalil, "Novel structural descriptors for automated colon cancer detection and grading," *Computer Methods and Programs in Biomedicine*, vol. 121, no. 2, pp. 92–108, 2015.

[15] N. Dif and Z. Elberrichi, "A new deep learning model selection method for colorectal cancer classification," *International Journal of Swarm Intelligence Research*, vol. 11, no. 3, pp. 72–88, 2020.

[16] M. Tan and Q. Le, "Efficientnet: rethinking model scaling for convolutional neural networks," in *Proceedings of the International Conference on Machine Learning*, pp. 6105–6114, PMLR, Baltimore, MD, USA, May 2019.

[17] K. He, X. Zhang, S. Ren, and J. Sun, "Deep residual learning for image recognition," in *Proceedings of the IEEE conference on computer vision and pattern recognition*, pp. 770–778, Las Vegas, NV, USA, June 2016.

[18] S. Zagoruyko and N. Komodakis, "Wide residual networks," 2016, https://arxiv.org/abs/1605.07146.

[19] Y. Huang, Y. Cheng, A. Bapna et al., "Gpipe: efficient training of giant neural networks using pipeline parallelism," 2018, https://arxiv.org/abs/1811.06965.

[20] S. S. Basha, S. R. Dubey, V. Pulabaigari, and S. Mukherjee, "Impact of fully connected layers on performance of convolutional neural networks for image classification," *Neurocomputing*, vol. 378, pp. 112–119, 2020.

[21] A. A. Borkowski, M. M. Bui, L. B. Thomas, C. P. Wilson, L. A. DeLand, and S. M. Mastorides, "Lung and colon cancer histopathological image dataset (lc25000)," 2019, https://arxiv.org/abs/1912.12142.

[22] Q. Dong, S. Gong, and X. Zhu, "Imbalanced deep learning by minority class incremental rectification," *IEEE Transactions on Pattern Analysis and Machine Intelligence*, vol. 41, no. 6, pp. 1367–1381, 2019.

[23] S. Ioffe and C. Szegedy, "Batch normalization: accelerating deep network training by reducing internal covariate shift," in *Proceedings of the International conference on machine learning*, pp. 448–456, PMLR, Hong Kong, China, June 2015.

[24] J. Liu, M. Wang, L. Bao, and X. Li, "EfficientNet based recognition of maize diseases by leaf image classification," in

*Journal of Physics: Conference Series*vol. 1693, no. 1, IOP Publishing, Article ID 012148, December 2020.

[25] A. Krizhevsky, I. Sutskever, and G. E. Hinton, "ImageNet classification with deep convolutional neural networks," *Communications of the ACM*, vol. 60, no. 6, pp. 84–90, 2017.

[26] D. C. Ciresan, U. Meier, J. Masci, L. M. Gambardella, and J. Schmidhuber, "Flexible, high performance convolutional neural networks for image classification," in *Proceeding of the Twenty-second international joint conference on artificial intelligence*, Catalonia Spain, June 2011.

[27] D. Ciregan, U. Meier, and J. Schmidhuber, "Multi-column deep neural networks for image classification," in *Proceedings of the 2012 IEEE conference on computer vision and pattern recognition*, pp. 3642–3649, IEEE, Providence, RI, USA, June 2012.

[28] N. Srivastava, G. Hinton, A. Krizhevsky, I. Sutskever, and R. Salakhutdinov, "Dropout: a simple way to prevent neural networks from overfitting," *Journal of Machine Learning Research*, vol. 15, no. 1, pp. 1929–1958, 2014.

[29] G. Marques, D. Agarwal, and I. de la Torre Díez, "Automated medical diagnosis of COVID-19 through EfficientNet convolutional neural network," *Applied Soft Computing*, vol. 96, Article ID 106691, 2020.

[30] K. Sirinukunwattana, S. E. A. Raza, Y. W. Tsang, D. R. Snead, I. A. Cree, and N. M. Rajpoot, "Locality sensitive deep learning for detection and classification of nuclei in routine colon cancer histology images," *IEEE Transactions on Medical Imaging*, vol. 35, no. 5, pp. 1196–1206, 2016.

[31] A. Gertych, Z. Swiderska-Chadaj, Z. Ma et al., "Convolutional neural networks can accurately distinguish four histologic growth patterns of lung adenocarcinoma in digital slides," *Scientific Reports*, vol. 9, no. 1, p. 1483, 2019.

[32] J. Deng, W. Dong, R. Socher, L. J. Li, K. Li, and L. Fei-Fei, "Imagenet: a large-scale hierarchical image database," in *Proceedings of the 2009 IEEE conference on computer vision and pattern recognition*, pp. 248–255, IEEE, Miami, FL, USA, June 2009.

Hindawi
Computational Intelligence and Neuroscience
Volume 2022, Article ID 9475162, 23 pages
https://doi.org/10.1155/2022/9475162

Research Article

An End-to-End Cardiac Arrhythmia Recognition Method with an Effective DenseNet Model on Imbalanced Datasets Using ECG Signal

Hadaate Ullah,[1] **Md Belal Bin Heyat**,[2,3,4] **Faijan Akhtar**,[5] **Sumbul**,[6] **Abdullah Y. Muaad**,[7] **Md. Sajjatul Islam**,[8] **Zia Abbas**,[3] **Taisong Pan**,[1] **Min Gao**,[1] **Yuan Lin**,[1,9] **and Dakun Lai**[10]

[1]*State Key Laboratory of Electronic Thin Films and Integrated Devices, School of Materials and Energy, University of Electronic Science and Technology of China, Chengdu 610054, Sichuan, China*
[2]*IoT Research Center, College of Computer Science and Software Engineering, Shenzhen University, Shenzhen 518060, Guangdong, China*
[3]*Centre for VLSI and Embedded System Technologies, International Institute of Information Technology, Hyderabad 500032, Telangana, India*
[4]*Department of Science and Engineering, Novel Global Community Educational Foundation, Hebersham 2770, NSW, Australia*
[5]*School of Computer Science and Engineering, University of Electronic Science and Technology of China, Chengdu 610054, Sichuan, China*
[6]*Department of Ilmul Qabalat wa Amraze Niswan (Gynecology and Obstetrics), National Institute of Unani Medicine, Rajiv Gandhi University of Health Sciences, Ministry of Ayush, Bengaluru, Karnataka, India*
[7]*IT Department, Sana'a Community College, Sana'a 5695, Yemen*
[8]*College of Computer Science, Data Intelligence and Computing Art Lab, Sichuan University, Chengdu 610065, China*
[9]*Medico-Engineering Corporation on Applied Medicine Research Center, University of Electronic Science and Technology of China, Chengdu 610054, Sichuan, China*
[10]*Biomedical Imaging and Electrophysiology Laboratory, School of Electronic Science and Engineering, University of Electronic Science and Technology of China, Chengdu 610054, Sichuan, China*

Correspondence should be addressed to Md Belal Bin Heyat; belalheyat@gmail.com, Abdullah Y. Muaad; abdullahmuaad9@gmail.com, Yuan Lin; linyuan@uestc.edu.cn, and Dakun Lai; dklai@uestc.edu.cn

Received 10 May 2022; Revised 25 July 2022; Accepted 17 August 2022; Published 29 September 2022

Academic Editor: Tawfik Al-Hadhrami

Electrocardiography (ECG) is a well-known noninvasive technique in medical science that provides information about the heart's rhythm and current conditions. Automatic ECG arrhythmia diagnosis relieves doctors' workload and improves diagnosis effectiveness and efficiency. This study proposes an automatic end-to-end 2D CNN (two-dimensional convolution neural networks) deep learning method with an effective DenseNet model for addressing arrhythmias recognition. To begin, the proposed model is trained and evaluated on the 97720 and 141404 beat images extracted from the Massachusetts Institute of Technology-Beth Israel Hospital (MIT-BIH) arrhythmia and St. Petersburg Institute of Cardiological Technics (INCART) datasets (both are imbalanced class datasets) using a stratified 5-fold evaluation strategy. The data is classified into four groups: N (normal), V (ventricular ectopic), S (supraventricular ectopic), and F (fusion), based on the Association for the Advancement of Medical Instrumentation® (AAMI). The experimental results show that the proposed model outperforms state-of-the-art models for recognizing arrhythmias, with the accuracy of 99.80% and 99.63%, precision of 98.34% and 98.94%, and $F_{1\text{-score}}$ of 98.91% and 98.91% on the MIT-BIH arrhythmia and INCART datasets, respectively. Using a transfer learning mechanism, the proposed model is also evaluated with only five individuals of supraventricular MIT-BIH arrhythmia and five individuals of European ST-T datasets (both of which are also class imbalanced) and achieved satisfactory results. So, the proposed model is more generalized and could be a prosperous solution for arrhythmias recognition from class imbalance datasets in real-life applications.

1. Introduction

With the advancement of computerized and automatic electrocardiogram (ECG) analysis, it is widely used in detecting and diagnosing heart diseases, assisting cardiologists with long-term ECG recordings and analysis. One significant indicator of heart disease is the detection of heartbeats, which is an essential factor in detecting arrhythmias. Arrhythmias are irregularities in heart conduction with electrical impulses, resulting in a disturbance in heart rate (irregular rhythm) [1], which necessitates careful, rapid, and frequent examination. In this case, automatic and computerized systems can be more useful. A traditional automatic arrhythmia recognition system includes (i) preprocessing [2], (ii) features extraction such as beat segmentation [3], QRS complex [4], R-peak or R-R interval [5], wavelet transform (WT) [5], time-frequency [6], morphological learning [6], and (iii) classification such as artificial neural network (ANN) [7], support vector machine (SVM) [8], decision tree (DT) [9, 10], and random forest (RF) [8] steps. However, despite a good number of shallow learning methods (features engineering techniques) with promising results for identifying arrhythmias from ECG signals, these are unable to properly describe the optimal features of signals and are prone to overfitting [11]. Furthermore, dealing with unbalanced data while yielding satisfactory results remains difficult [12]. Several researchers attempted to solve these problems by optimizing classifiers' generalization capabilities [13]. Due to the limited nonlinear fitting, the learning parameters in machine learning face a challenge during training to extract all features from ECG. As a result, the pattern recognition performance of classifiers in traditional methods from ECG signals is typically insufficient in the context of big data-driven [14]. Considering the aforementioned challenges of machine learning approaches [15, 16], an effective recognition method that takes a different approach is highly desired in arrhythmia diagnosis.

Deep learning approaches for arrhythmia recognition, such as deep neural networks (DNNs) [17], convolution neural networks (CNNs) [18, 19], recurrent neural networks (RNNs) [18], long short-term memory (LSTM) [20], and combining of these approaches [21], have recently gained popularity [22, 23]. Aside from arrhythmia recognition, deep learning approaches have received a lot of attention recently in other applications, such as emotion recognition from electroencephalography (EEG) [24–28]. Although high-level features learned from ECG inputs of such developed deep learning models automatically perform feature extraction and recognition, satisfactory performance of arrhythmia diagnosis remains a challenge. The major factors behind this challenge are as follows: (i) some patterns of ECG are hard to detect in deep learning because of extensive volume of data demanding for training the deep networks with the target domain, even it is hard to recognize by experienced physicians [17] in some cases, and (ii) deep networks tends to vanishing gradient problems during training. The first challenge could be addressed by a mechanism known as "transfer learning," in which experienced learning from the upstream dataset (large volume dataset) is transferred into the downstream dataset (target dataset), and pretrained weights from the upstream dataset are used as the target dataset's initial weights [29]. This mechanism could easily solve the deep network overfitting problem. A few contributions to the literature address the transfer learning mechanism for detecting abnormalities in ECG signals [30–33]. In this type of approach, there is no requirement to develop a model from scratch.

However, the appearance of ResNet [34] in deep learning marked a turning point in CNN models. ResNet's interesting developments include shortcut and skip connections between the front and back layers, which aid in resolving vanishing gradient problems. Following the benefits of ResNet, DenseNet [35] introduces an intriguing connectivity pattern among the layers known as "dense connections" for the further improvement of ResNet, in which feature maps for each layer in a dense block are followed by all of its previous layers, with direct connections from low- to high-level layers. As a result, the second challenge of recognizing arrhythmias with satisfactory results could be overcome by developing a model based on the dense connections mechanism. In this study, an end-to-end 2D CNN method with an effective DenseNet model was proposed to recognize arrhythmias from ECG automatically, taking into account the potential benefits of a CNN-based DenseNet model addressing the aforementioned challenge in cardiac arrhythmia recognition. Recently, 2D CNN approaches for arrhythmias recognition have gained popularity because of the transformation of sequential data of beats into their corresponding beat images, which alleviates the time strict alignment problem of beats ignoring the score of fiducial points. The duration and amplitude of various waves of an ECG signal, such as RR intervals, QRS complex, P-wave, and T-wave, are highly sensitive to its dynamic and morphology features. ECG signals from time series data could be transformed into 2D images in a variety of ways, such as time-frequency (short-time Fourier transform (STFT) [36], continuous wavelet transform (CWT) [37, 38], discrete wavelet transform (DWT)), frequency spectrum, own developed python module [39].

Besides, some interesting contributions are introduced in the literature addressing dense connections mechanism for ECG classifications. Rubin et al. [40] proposed a densely connected CNN for atrial fibrillation (AF) detection from ECG by combining the SQI (signal quality index) algorithm to assess the noisy instances in ECG. Importantly, this work discussed an additional challenge of the imbalance problem in private or publicly available arrhythmia datasets, which may significantly impact the accuracy of arrhythmia diagnosis in real-life applications. Importantly, this work discussed an additional challenge of the imbalance problem in private or publicly available arrhythmia datasets, which may significantly impact the accuracy of arrhythmia diagnosis in real-life applications. Some interesting contributions have been demonstrated in the literature for resolving the challenge [12, 41–43]. We have used the weighted categorical cost function [44] to handle the imbalanced data in this study due to the function's several advantages. In this study, a novel and end-to-end 2D CNN-based deep learning

method is proposed for cardiac arrhythmia recognition with improved performance, taking into account the aforementioned challenges and opportunities. The following are the key contributions near the end:

(i) A 2D CNN model is developed to recognize arrhythmias with greater accuracy than state-of-the-art models on imbalanced datasets.

(ii) The proposed model expresses model generalization because it was tested on four datasets without changing any hyperparameters, and the model architecture and results are consistent.

(iii) This achievement is due to the use of some diverse regularization strategies: batch normalization (BN) [45], call-back features [46], weighted random sampler [47], Adam optimizer [48], on-the-fly augmentation [49], and appropriate initialization of layers [50] of the model in the method.

The rest of the paper is expressed as follows. The proposed methodology is presented in Section 2 with details. Results and discussions with study limitations and prospects are included in Section 3. Finally, Section 4 concludes the study.

2. Methods and Materials

2.1. Dataset Description

2.1.1. MIT-BIH Arrhythmia Database. MIT-BIH arrhythmia database: The MIT-BIH arrhythmia database is a widely used benchmark database for evaluating the performance of arrhythmia detectors. It contains 48 records from 47 subjects (25 males aged 32 to 89 and 22 females aged 23 to 89) with 30-minute two-channel ambulatory Holter ECG recordings. The recordings are sampled at 360 Hz per channel with an 11-bit resolution over a 10 mV range. Its first channel describes the upper signal, MLII (a modified limb lead II), and its second channel describes the lower signal, modified lead V1 (rarely as V2 or V5, and only once as V4), with electrodes placed on the chest in both cases. In the upper signal, normal QRS complexes are more visible. As a result, the upper signal lead is chosen in our study. Records 102 and 104 are involved with patient surgical dressings and records 102, 104, 107, and 217 are involved with paced beats, so we excluded these records from our experiment.

2.1.2. INCART 12-Lead Arrhythmia Database. INCART contains a total of 75 annotated records extracted from the 32 Holter recordings. Every record is thirty minutes long, holds the twelve standard leads, and is sampled at 257 Hz with varying gains from 250 to 1100 per mV. The records were accumulated from the patients who were undergoing tests on coronary artery diseases. Most of them had ventricular ectopic beats, and nobody had pacemakers. ECGs from subjects with arrhythmias, coronary artery disease, ischemia, and conduction abnormalities were preferred for incorporation into the database. Leads II and V1 are two of the 12 standard leads that appear more frequently in this dataset. In the lead II, QRS complexes are more noticeable. As a result, lead II is chosen in this study, similar to the MIT-BIH arrhythmia database. The dataset is used in this study to test the generalization of the proposed model.

2.1.3. MIT-BIH Supraventricular Arrhythmia Database. This database contains 78 two-lead ECG recordings with a sampling rate of 128 Hz, each with half an hour. The annotation of recordings was performed with the Marquette Electronics 8000 Holter scanner firstly, and it was corrected and reviewed later with a medical student. The original labeling was modified in accordance with AAMI recommendations. It is a supplementary dataset of MIT-BIH arrhythmia that is chosen only for testing or evaluating the performance of the proposed model in this study. Only five records, 800, 828, 849, 867, and 873, are considered for transfer learning, and one record, 873, is considered for testing the performance of the proposed model.

2.1.4. European ST-T Database. The database includes 79 patients' ambulatory ECG recordings from 90 annotated snippets. There were 8 women and 70 males, aged 55 to 84, in the study. Each two-hour record includes two lead signals sampled at 250 samples per second with 12-bit resolution across a nominal 20-millivolt input range. After digitization, the sample values were rescaled with reference to calibration signals in the original analog recordings to ensure a uniform scale of 200 analog-to-digital-converter units per millivolt for all signals. Each record is documented by concise clinical reports. These reports, which are stored in the header (.hea) files associated with each recording, summarize pathology, medications, electrolyte imbalance, and technical information. Two cardiologists annotated each record beat by beat, looking for changes in ST segment and T-wave morphology, rhythm, and signal quality. ST segment and T-wave changes in both leads were identified (using predefined criteria that were applied consistently in all cases), and their onsets, extrema, and ends were annotated. Only five records, e0103, e0121, e0202, e0413, and e0614, are considered for transfer learning, and one record, e0121, is considered for testing the performance of the proposed model.

2.2. Method Overview. Herein, an arrhythmia recognition framework is made. To begin, annotated data from the MIT-BIH arrhythmia, St. Petersburg INCART 12-lead, MIT-BIH supraventricular arrhythmia, and European ST-T database datasets are selected to categorize the arrhythmias into four classes of interest. The raw data instances are then segmented into available beats and transformed into RGB (Red, Green, and Blue) images via the preprocessing step. The proposed method makes use of the transformed images as input. This framework's model architecture is based on the structure (DenseNet) in [35] to perform recognition. Three dense blocks are created in this model, each with five inner layers, followed by a transition layer to extract the features from our preprocessed images. Finally, preprocessed images are classified as N, S, V, and F (based on AAMI) with two fully

connected (FC) layers and a softmax classifier. Based on AAMI recommendations, the class mappings of all datasets are as follows: (1) N-normal, (2) V-ventricular ectopic, (3) S-supraventricular ectopic, (4) F-fusion, and (5) Q-unknown. Because of the involvement of paced and unclassified beats, the *Q* class is not considered in this study. The overall method includes three subsections: (1) data preprocessing, (2) feature extraction and recognition based on the proposed DenseNet model, and (3) model evaluation. We have evaluated the proposed method with the strategies (experiments): E_1-experiment 1 (5-fold stratified cross-validation (CV) on MIT-BIH dataset), E_2-experiment 2 (5-fold stratified CV on INCART dataset, for the generalization purpose of the proposed model), E_3-experiment 3 (MIT-BIH as the training and MIT-BIH supraventricular arrhythmia is only for evaluation), E_4-experiment 4 (INCART as the training and MIT-BIH supraventricular arrhythmia is only for evaluation), E_5-experiment 5 (learned experiences from MIT-BIH arrhythmia dataset by the proposed model are transferred into MIT-BIH supraventricular arrhythmia dataset using transfer learning mechanism), and E_6-experiment 6 (learned experiences from INCART dataset by the proposed model are transferred into MIT-BIH supraventricular arrhythmia dataset), E_7-experiment 7 (MIT-BIH as the training and European ST-T database is only for evaluation), E_8-experiment 8 (INCART as the training and European ST-T database is only for evaluation), E_9-experiment 9 (learned experiences from MIT-BIH arrhythmia dataset by the proposed model are transferred into European ST-T dataset using transfer learning mechanism), and E_{10}-experiment 10 (learned experiences from INCART dataset by the proposed model are transferred into European ST-T dataset). In the transfer learning mechanism, learned knowledge from a large volume of dataset is transferred into a small volume of dataset (target dataset, which is unseen) during the evaluation. The developed model is fine-tuned in this mechanism by randomly initializing the weights of FC layers remaining the same target classes (N, S, V, and F). Transfer learning is a promising technique for dealing with the challenge of large volume training datasets in deep learning. As a result, the technique is more useful in real-world applications, particularly in remote health monitoring sensor devices. The complete framework with the stratified K-fold cross-validation of the proposed method for E_1, E_2, E_3, E_4, E_7, and E_8 is demonstrated in Figure 1(a). However, the model is in only evaluation mode in the case of E_3, E_4, E_7, and E_8 and tested with the MIT-BIH supraventricular (E_3 and E_4) and European ST-T (E_7 and E_8) datasets. Figure 1(b) illustrates the workflow of the proposed method using a transfer learning mechanism in the case of E_5, E_6, E_9, and E_{10}.

2.3. Data Preprocessing. Following segmentation, 1D ECG signals are transformed into 2D RGB beat images, fed as input to the developed 2D DenseNet model, segregating various characteristics in the images. Every record in our chosen datasets contains the signals, annotation, and header files for the ECG signals. After downloading the data for each dataset, the annotation file is obtained from these files using Python's Glob module. The individual heartbeats are then segmented from the QRS complexes of ECG signals by slicing each beat using the R-peak wave detection algorithm. This algorithm is more accurate than others in the literature [19]. Once R-peaks are detected, a single beat is traced by taking into account 250 ms (90 sampling points) before and after the R-peak. The distance is sufficient to represent a beat while excluding neighbor heartbeats from an ECG signal [51]. This study's datasets do not all have the same sampling frequency. As a result, the dataset records must be resampled before segmentation. We completed the beats segmentation task using the WFDB Toolbox and the Biosppy Python module at a sampling frequency of 250 Hz. A CSV file of heartbeat sequences for each beat category was received. The Python Matplotlib module and OpenCV are used to convert the segmented beats from the CSV files into their equivalent RGB images of 128128 pixels. Finally, for the four class labels, we received 97720 (N-87311, S-2706, V-7080, and F-623) and 141404 (N-129585, S-1712, V-10001, and F-106) extracted beat images from the MIT-BIH and INCART datasets, respectively. The total of 10244 (N-9797, S-368, V-64, and F-15) and 1673 (N-1622, S-13, V-23, and F-15) beat images for five (800, 828, 849, 867, and 873) records and one (873) record are received from the MIT-BIH supraventricular dataset, respectively. Besides, the European ST-T dataset yielded 44169 (N-43516, S-168, V-364, and F-121) and 10828 (N-10595, S-79, V-91, and F-63) beat images for five (e0103, e0121, e0202, e0413, and e0614) records and one (e0121) record, respectively. Figure 2(a) shows the segmentation of beats, while Figures 2(b) to 2(f) show the transformed beats images. The transformed images are fed into the developed model for feature extraction. A high-level feature vector is generated from these extracted features, and arrhythmia recognition is performed using a softmax classifier.

2.4. Features Extraction Based on Proposed DenseNet and CNN Classifier. Deep learning approaches, particularly several CNNs, have recently emerged as the dominant techniques for image classification [52]. CNNs carry out convolution operations between kernels and tensors. RGB images are used as the input to the developed model. As a result, it should have three channels to represent the intensities of three primary colors (red, green, and blue). The kernels in the convolution operation can be considered as the filters that detect edges, shapes, and other patterns in the input ECG beat images. One major flaw in CNNs is that information may disappear while training the network, a phenomenon known as the "vanishing gradient problem," as the network's layers become deeper. Though there are several primary approaches to solving the problem, such as layer-wise pretraining and proper activation function selection, dense connections in the DenseNet [35] are a promising mechanism compared to such approaches. DenseNet provided state-of-the-art performance with no degradation despite stacking hundreds of layers. This architecture signifies that the CNNs are deeper and more effective. The DenseNet architecture consists of a series of

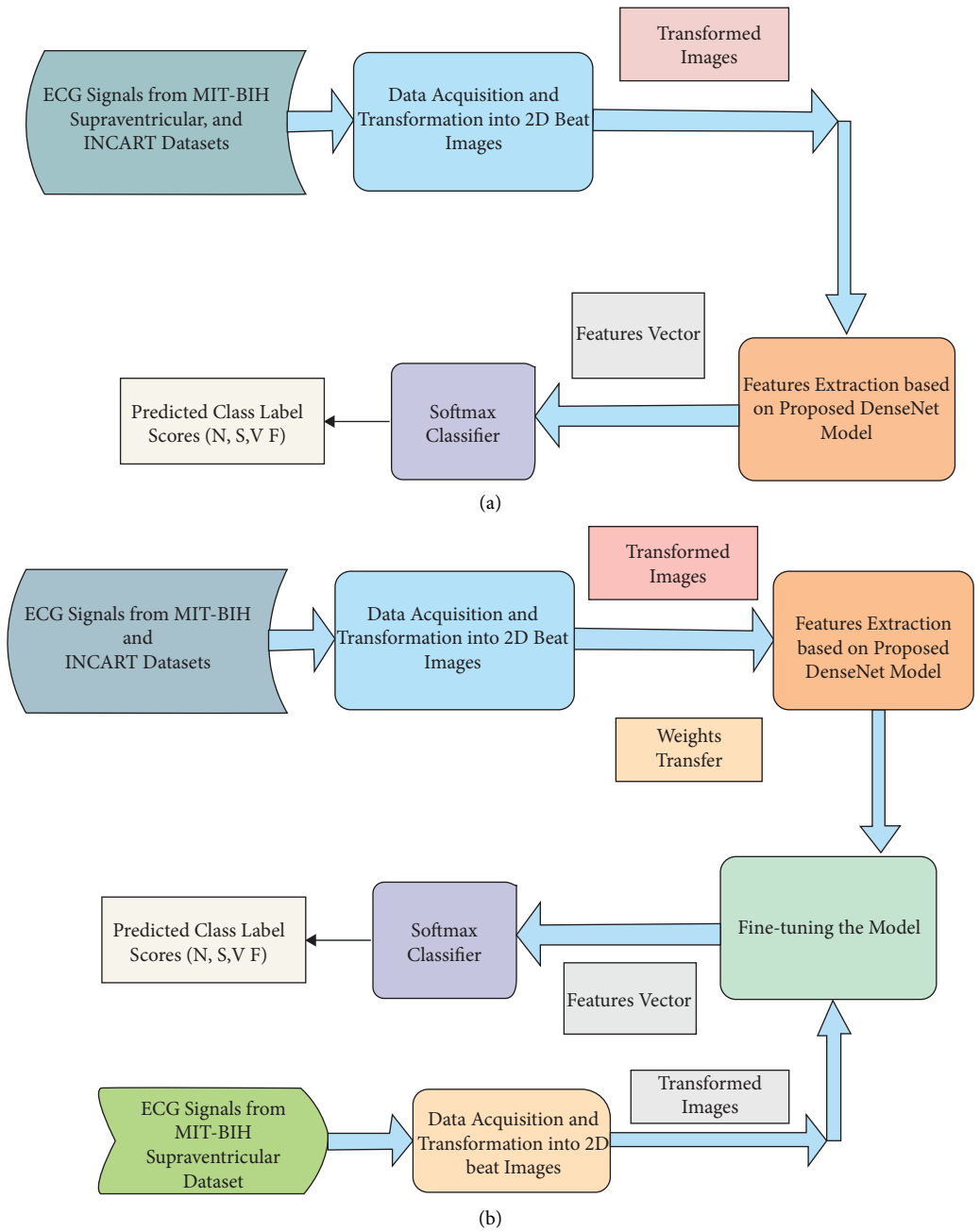

Figure 1: The workflow of the proposed method (a) with stratified K-fold cross-validation (in case of E_3, E_4, E_7, and E_8, the model is in only evaluation mode); (b) using transfer learning mechanism (in case of E_5, E_6, E_9, and E_{10}).

dense blocks and transition layers [35]. Transition layers facilitate the downsampling, which is required to change the size of features map in CNNs. DenseNet's architecture differs from other CNNs in that it allows for more narrowing layers, which is controlled by a hyperparameter called "growth rate" k. Each layer holds a k features map at its output. In this study, the minimal optimum configuration consists of three dense blocks, each of which contains five convolutional layers with nonlinear activation functions, ReLUs, and BN, followed by a transition layer, depicted in Figure 3. Each convolutional layer generates 32 feature maps (number of output channels), which are concatenated to all previous convolutional feature maps in the depth direction. Figure 4 illustrates the concept indicating the reused feature maps from all the preceding layers in a dense block with five layers. For instance, the input channel of the second convolutional layer is 32 (first convolutional layer output), but the input channel of the third convolutional layer is 64 ($32^*2 = 64$ for the two prior convolutional layers) and generates 32 output channels, and so on. The produced feature map through the convolving of learnable filters/output channel numbers across the input images is fed to ReLU, a nonlinear activation function. The convolution output channel number as the base value is set to 32. No

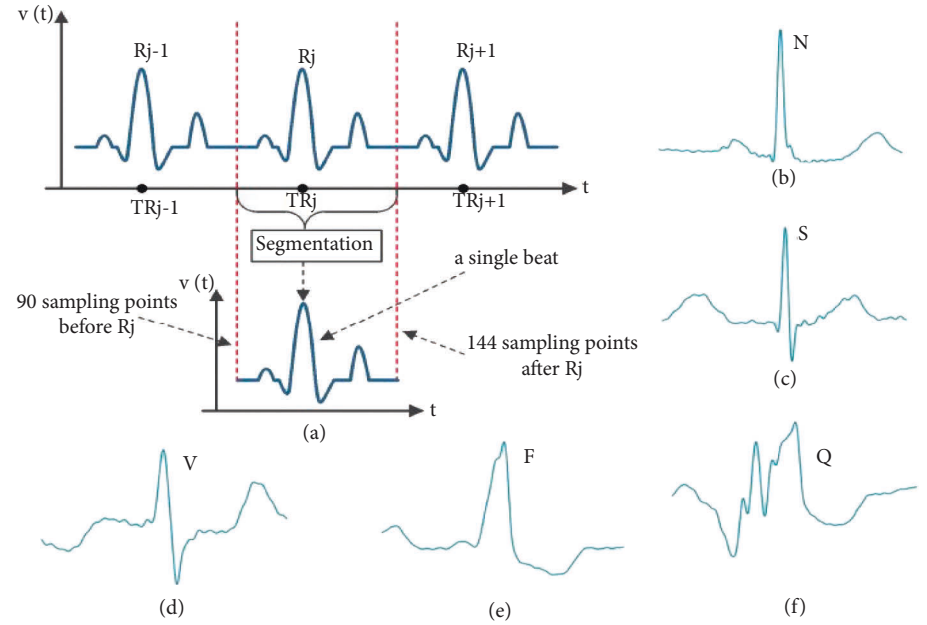

FIGURE 2: ECG signal representation such as (a) heartbeat segmentation demonstration, (b) normal beat, (c) supraventricular ectopic beat, (d) ventricular ectopic beat, (e) fusion beat, and (f) unknown beat.

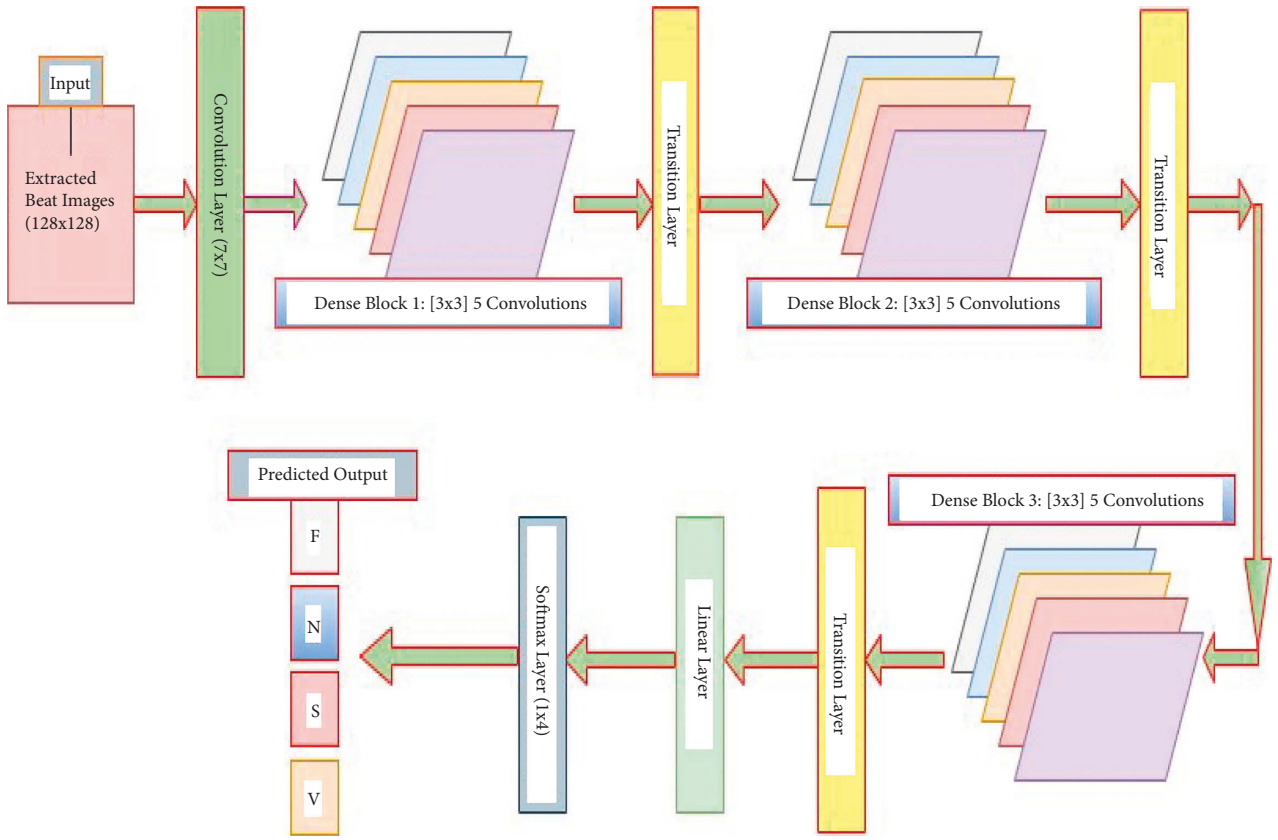

FIGURE 3: The proposed DenseNet model structure with three dense blocks.

further significant enhancement is achieved with greater channel numbers, dense blocks, and transition layers. This probably happened due to the small volume of preprocessed images during training the network compared to ImageNet.

The convolutional layers are the prime components of CNNs, where major functions of CNNs are performed. Large filter 7×7 is considered at the starting of the model in the convolution layer with a spatial downsampling of

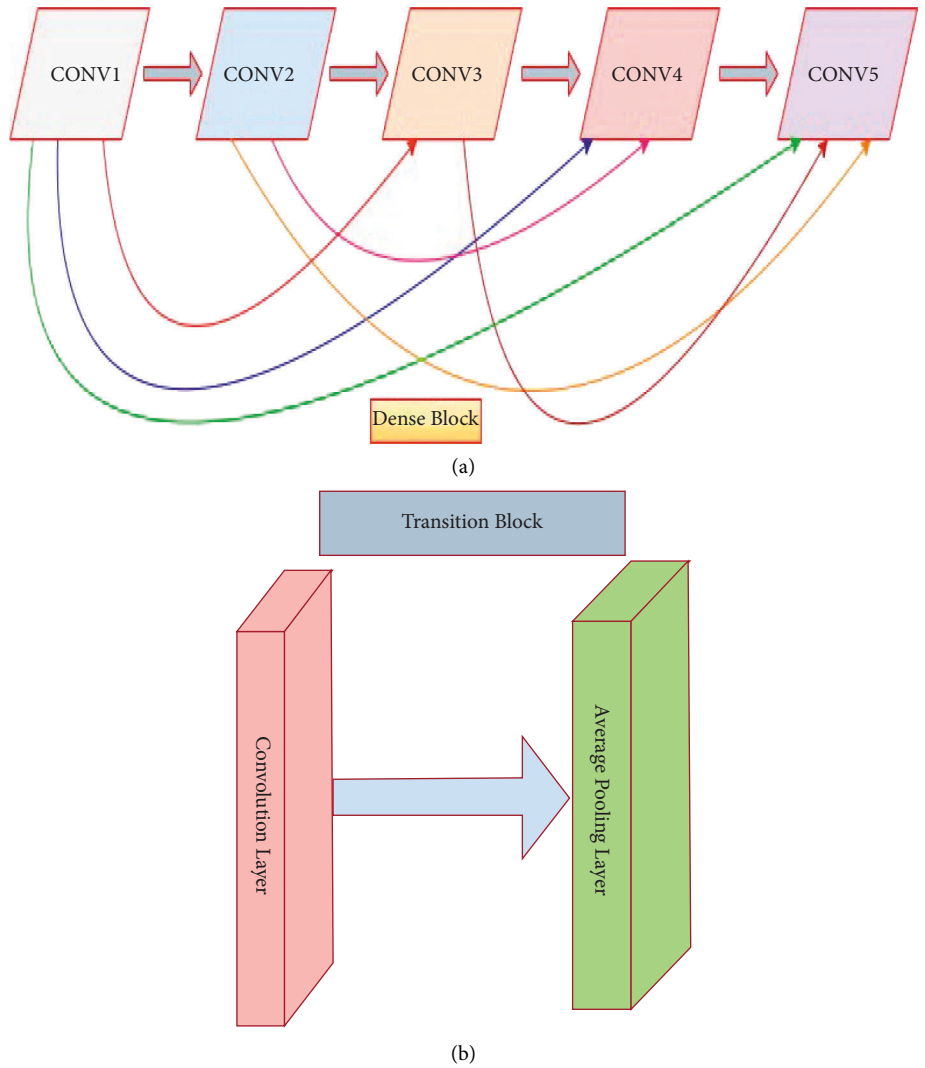

FIGURE 4: (a) Internal structure of a dense block, where every convolutional layer receives the outputs from all prior layers as the input, and (b) structure of a transition block.

striding of 2 to conceal the inconsequent features from images. In the preprocessed images, the desired features appear in the narrow part of the full image. And hence, the subsequent convolution layers in the dense blocks with a small size of 3×3 and no spatial downsampling are chosen to extract the locally replicated features. As a result, the computational cost of the model is reduced. The employed ReLUs in the dense blocks and transition layers help to suppress vanishing gradient problems during training. BN [45] layers are used to accelerate the training. As a result, the learnable parameters converge with the imminent possible time of training. It also suppresses the sensitivity and interior covariate shift of training in the direction of weight initialization. This is one kind of regularization technique to reduce overfitting during the training phase. The weights during training are made with the gradient-based back-propagation mechanism.

As shown in Figure 3, a transition layer is embodied after each block as the adjacent two blocks that minimize the computational complication with a bottleneck structure. It reduces the dimension of the feature map by removing the learnable parameters. The transition layer receives activations from all of the dense block's preceding kernels. It consolidates them using convolution and pooling operations. Its primary functions are convolution and pooling. Conv., BN, ReLU, and average pooling layers are included in each transition layer. Each transition layer's average pooling layer calculates the average for each patch of feature maps and extracts average spatial high-level features. It also serves as a translation-invariant to help filters and kernels detect the morphological shapes of input images. No learnable parameters are produced from this layer. The output shape of the last pooling layer in the final transition layer is $64 \times 16 \times 16$ with a kernel size of 2×2 and stride of 2, as shown in Table 1. The convolutional layer with a 1×1 kernel size in the transition layer is used to capture the information across the channel features and deliver the identical output feature maps of 32 in the convolutional layer for the next

Table 1: The developed DenseNet model's internal architecture, including relevant hyperparameters. ReLU, BN, fully connected, and softmax layers are not shown here.

Dense blocks	Layers name	Output size	Kernel size	# Filters	Stride	Padding
Primary convolution layer	Conv2d-1	128 × 128	7 × 7	64	2	3
Dense_Block-1	Conv2d-4	128 × 128	3 × 3	32	1	1
	Conv2d-6	128 × 128	3 × 3	32	1	1
	Conv2d-9	128 × 128	3 × 3	32	1	1
	Conv2d-12	128 × 128	3 × 3	32	1	1
	Conv2d-15	128 × 128	3 × 3	32	1	1
Transition layer -1	Conv2d-19	128 × 128	1 × 1	128	1	0
	AvgPool2d-22	64 × 64	2 × 2	128	2	0
Dense_Block-2	Conv2d-25	64 × 64	3 × 3	32	1	1
	Conv2d-27	64 × 64	3 × 3	32	1	1
	Conv2d-30	64 × 64	3 × 3	32	1	1
	Conv2d-33	64 × 64	3 × 3	32	1	1
	Conv2d-36	64 × 64	3 × 3	32	1	1
Transition layer -2	Conv2d-40	64 × 64	1 × 1	128	1	0
	AvgPool2d-43	32 × 32	2 × 2	128	2	0
Dense_Block-3	Conv2d-46	32 × 32	3 × 3	32	1	1
	Conv2d-48	32 × 32	3 × 3	32	1	1
	Conv2d-51	32 × 32	3 × 3	32	1	1
	Conv2d-54	32 × 32	3 × 3	32	1	1
	Conv2d-57	32 × 32	3 × 3	32	1	1
Transition layer -3	Conv2d-61	32 × 32	1 × 1	64	1	0
	AvgPool2d-64	16 × 16	2 × 2	64	2	0

block, which goes through the average pooling layer with subsampling. The transition layer can also play the compression preface to control the model size by a factor θ, called compression in the $0 < \theta m \leq 1$ range. If a dense block has m feature maps, the following transition layer produces θm output feature maps. In our experiment, we have fixed $\theta = 1$ to keep the number of feature maps unchanged across the transition layers. After passing all blocks and transition layers, the feature map of the last average pooling layer is reduced to $64 \times 16 \times 16$, which goes to linear layers for the classification. The output of the linear layer contains the high-level model ascertainment. These layers learn the features vector so that the softmax layer can properly recognize the preprocessed images. The final linear layer's output channel numbers are set to the required number of classes and fed through the softmax activation function for the final predicted labels. In our study, two linear layers are used to ensure that the model learns input patterns correctly. Finally, at the model's end, a softmax layer is included to recognize the arrhythmia labels using numerical processing.

2.5. Cost Function and Evaluation Metrics. The cost function or cross-entropy loss is used to assess how well a model is trained. It represents the difference between training samples and predicted labels, thus scoring the training loss. It bridges the gap between measured labels and targets. The function displays the training efficiency of a model. A gradient-descent-based optimizer with a learning rate controls the loss of cost function. Adagrad, Adam, and Adadelta are a few well-known optimizers. Adam optimizer function is used in our experiment, which gets to the optimal points faster than others [48]. This weighted categorical cost function is better suited to dealing with imbalanced data [44, 53]. The MIT-BIH, INCART, MIT-BIH Supraventricular, and European ST-T datasets are more unbalanced. As a result, we chose this function in our study to address the class biasing issue. Let w represent the vector weights of the prescribed classes, with a large w_i value corresponding to a high penalty applied to the incorrect label predictions. The weighted categorical cost function is as follows:

$$CE = -\frac{1}{D}\sum_{j}^{D}\sum_{i}^{C} w_i t_{ij} \log p_{ji}. \tag{1}$$

where D represents the training samples, and C narrates the class numbers. As for the example, if t_j holds the class i, $t_{ji} = 1$ and p_{ji} will be the predicted probability; otherwise, $t_{ji} = 0$.

The performance of our proposed method is evaluated with four metrics: precision, recall, $F_{1\text{-score}}$, and accuracy, which are expressed in (2) to (5) [54–56], where TP, FP, TN, and FN are the true positive, false positive, true negative, and false negative, respectively. TP represents the beat recognition result in which positive is represented as positive, whereas FN represents the result in which positive is represented as negative. TN, on the other hand, defines the beat identification result in which the negative is evaluated as negative, whereas FP defines the result in which the negative is evaluated as positive. The recall and precision parameters could be used to specify the model's sensitivity and exactness. $F_{1\text{-score}}$ is used to capture the accuracy by summing up the recall and precision for every predicted class sample. Finally, accuracy assesses the method performance across all beat classes. The metrics equations are as follows:

$$precision = \frac{TP}{TP + FP}. \quad (2)$$

$$recall = \frac{TP}{TP + FN}. \quad (3)$$

$$F_{1-score} = 2 \times \frac{precision \times recall}{precision + recall} = \frac{2TP}{2TP + FP + FN}. \quad (4)$$

$$Accuracy = \frac{TP + TN}{TP + FP + TN + TF}. \quad (5)$$

2.6. Experimental Details. All experiments are carried out in PyTorch open-source framework on Windows 10 with Intel Corei5-7400 CPU @ 3.00 GHz, 8 GB RAM, and an NVIDIA GeForce RTX 2070 graphic card with 8 GB memory. For proper initialization, an intelligent weight initialization mechanism for the available layers in the model is required, which aids the model in alleviating biasing. Layer weights could be expressed as kernels and groups of kernels that form a single layer. The proposed model employs the Kaiming normal distribution [50] to initialize the weights in all convolution layers. All BN layers' biases and weights are initialized with the constants 0 and 1, respectively. The Xavier initializer and a constant 0 are used to initialize the weights and biases of fully connected layers, respectively. The primary goal of using these initializers is to balance the gradients scale across all kernels. The performance of a model is highly dependent on the training to testing sets ratio. As a result, the random split technique is used to partition the entire set of preprocessed images into a validation set. The K-fold cross-validation strategy is used to train and evaluate the model. A validation set is typically required to confirm whether or not the model has achieved sufficient accuracy using the training and testing set ratio settings in the training module. Without the validation set, the model could have become overfit. In the hold-out evaluation strategy, K-fold cross-validation is a promising technique for resolving such changing issues as training and testing set ratio. In this strategy, the samples are randomly grouped into the total k-fold, and k splits are generated. We used stratified 5-fold cross-validation in our study. As a result, in each split, one fold serves as the validation or testing set, while the remaining four folds serve as the training set. In this case, 10% of the total extracted beat images are preserved for testing, while the remaining 90% are used for model training, resulting in a training and testing splitting ratio of 9 : 1.5-folds reducing the computation cost while increasing the likelihood of samples from each class entering each fold. Furthermore, a stratified K-fold ensures that samples from each class enter each fold, reducing the class imbalance problem more effectively than K-fold. The initial learning rate and batch size are set to 0.001 and 32. To optimize the cross-entropy loss, a gradient descent optimizer with a learning rate scheduler is required. In this study, the Adam optimizer [48] with the PyTorch REDUCELRONPLATEAU scheduler is chosen to achieve the desired performance. If the validation loss becomes a plateau for 5 consecutive epochs, the learning rate is reduced by 0.1. During the training process, a weighted random sampler [47] is also used to ensure the representativeness of the equal samples from each class. To achieve the optimal training time, an appealing regularization technique called early stopping [46] is used. If the validation loss remains constant for the next eight epochs, the training is terminated, and the overfitting is reduced. In the training module, the transformed 2D RGB images are simply rotated randomly by 6 degrees before being converted into tensors; this technique is known as "on-the-fly augmentation" of data. This is also a likely factor in reducing model overfitting during training. Finally, the delivered accuracy of our proposed method in E_1 and E_2 on the extracted beat images from the MIT-BIH and INCART arrhythmia datasets is 99.80% and 99.63%, respectively. Furthermore, E_3, E_4, E_5, E_6, E_7, E_8, E_9, and E_{10} achieve accuracy of 99.70%, 99.94%, 99.70%, 99.87%, 99.90%, 99.95%, 99.87%, and 99.95%, respectively.

3. Results and Discussion

3.1. Classification Results. In this study, extracted heartbeat images from ECG signals from four publicly available imbalanced datasets are used to detect arrhythmias in cardiac patients. It is attempted to improve the detection performance by looking into issues where the developed CNN models for arrhythmia recognition are incompetent. A confusion matrix, depicted in Figure 5(a), could express the performance details of all metrics on the MIT-BIH arrhythmia dataset (E_1). The confusion matrix is non-normalized row-wised. The entries in the diagonal correctly represent beat recognition, while the entries in the off-diagonal express the beat misclassification rate. The rows of Figure 5(a) show that the 87150 N, 7061 V, 2691 S, and 620 F beats are correctly classified out of 87311, 7080, 2706, and 623 beats, respectively. Only 161 N, 19 V, 15 S, and 3 F beats are incorrectly classified. Despite class imbalance issues in the MIT-BIH arrhythmia dataset, it indicates the intended accuracy in each class. The overall accuracy, $F_{1\text{-score}}$, recall, and precision achieved in standard testing are 0.9980, 0.9891, 0.9996, and 0.9834, respectively. Table 2 shows a summary of all metrics (average accuracy, precision, recall, and $F_{1\text{-score}}$) from the confusion matrix (shown in Figure 5(a)) received in E_1. This table clearly shows that the average values for all metrics are close to the overall values, indicating that the developed training module for testing the experiments has generalized. The average accuracy, $F_{1\text{-score}}$, recall, and precision achieved are 0.9990, 0.9892, 0.9963, and 0.9823. The table also shows that the F beat identification precision is low compared to other beats, resulting in a lower F_{1_score}. Figure 5(b) depicts the loss curves used in this experiment for model training and testing. The training loss curve is nearly stable after 61 epochs, whereas the testing loss curve changes abruptly at the start and is nearly stable after 61 epochs, analogous to the training loss curve. The model is halted after 123 epochs due to the use of an early stopping feature during training and evaluation, even though the total number of epochs is set to 200. As a result, the developed

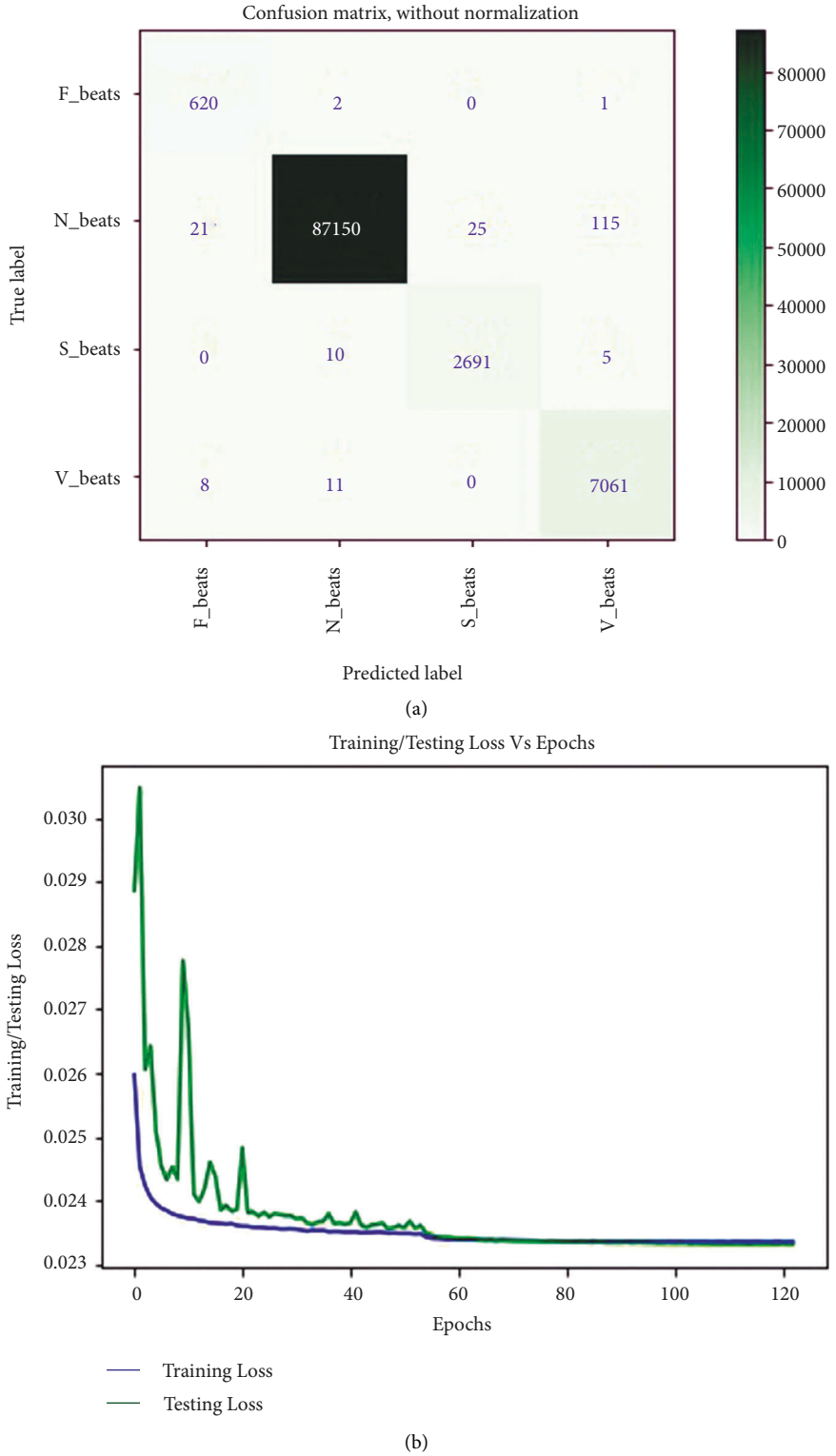

Figure 5: (a) Confusion matrix from MIT-BIH arrhythmia dataset in E_1, and (b) training and testing loss curve for E_1.

model efficiently completes the training and evaluation process without encountering any overfitting issues. In this experiment, the minimum validation loss is 0.0233. Finally, we can say that the model produced the desired level of achievement on our preprocessed images from the MIT-BIH arrhythmia dataset.

A confusion matrix was used to figure out the performance details of all matrices on the INCART arrhythmia dataset (E_2), shown in Figure 6(a). According to the rows of the confusion matrix, the 129124 N, 9964 V, 1685 S, and 106 F beats are correctly classified out of 129585, 10001, 1712, and 106 beats, respectively. Only 461 N, 37 V, and 27 S

Table 2: A summary of metrics from confusion matrix depicted in Figure 5(a).

Accuracy(%)		Precision (%)		Recall (%)		F_{1score} (%)	
N	99.81	N	99.97	N	99.82	N	99.90
S	99.96	S	99.08	S	99.45	S	99.26
V	99.86	V	98.32	V	99.73	V	99.02
F	99.97	F	95.53	F	99.52	F	97.49
Average	99.90	Average	98.23	Average	99.63	Average	98.92

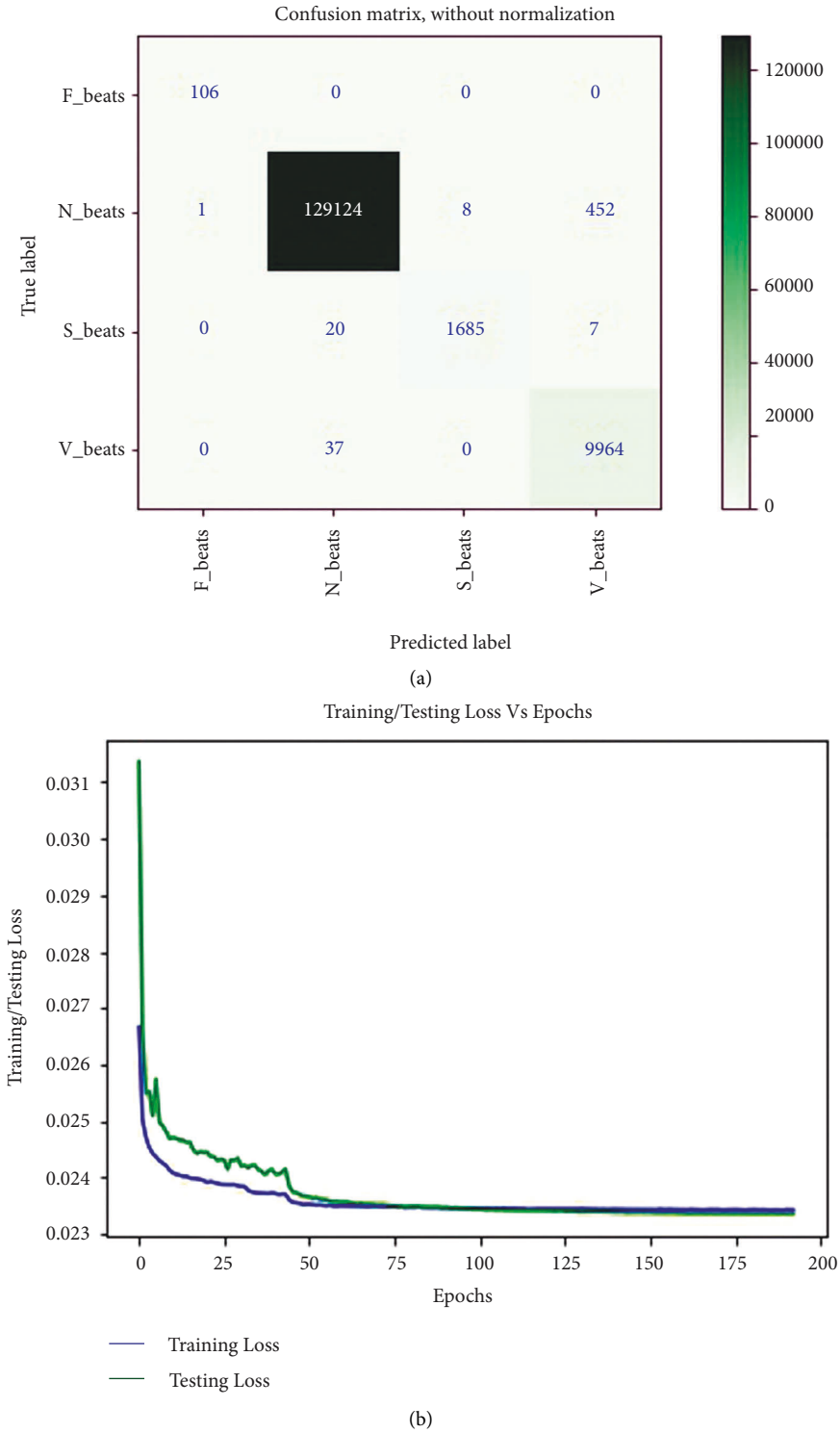

Figure 6: (a) Confusion matrix from INCART arrhythmia dataset in E_2, and (b) training and testing loss curve for E_2.

Table 3: A summary of metrics from confusion matrix depicted in Figure 6(a).

Accuracy (%)		Precision (%)		Recall (%)		F_{1score} (%)	
N	99.63	N	99.96	N	99.64	N	99.80
S	99.98	S	99.53	S	98.42	S	98.97
V	99.65	V	95.60	V	99.63	V	97.57
F	99.99	F	99.07	F	100.0	F	99.53
Average	99.81	Average	98.54	Average	99.42	Average	98.97

beats are incorrectly classified; all F beats are correctly classified. It also expresses the desired accuracy in each class despite the INCART dataset's class imbalance issues. The overall accuracy, $F_{1\text{-score}}$, recall, and precision achieved in standard testing are 0.9963, 0.9891, 0.9942, and 0.9894, respectively. Table 3 shows a summary of all metrics (average accuracy, precision, recall, and $F_{1\text{-score}}$) from the confusion matrix (shown in Figure 6(a)) received in E_2. It is also clear from this table that the average values for all metrics are close to the overall values. Average accuracy, $F_{1\text{-score}}$, recall, and precision obtained are 0.9981, 0.9897, 0.9942, and 0.9854, respectively. The table also shows that the precision for V beat identification is low in comparison to other beats, resulting in a lower $F_{1\text{-score}}$. Figure 6(b) depicts the loss curves for the model's training and testing. The training loss curve is nearly stable near 75 epochs, whereas the testing loss curve changes abruptly at the beginning and remains nearly stable after 75 epochs, analogous to the training loss curve. Despite the fact that the epoch is set to 200, the model stops at 193 epochs. The model successfully completes the training and evaluation process with no overfitting issues. In this experiment, the minimum validation loss is 0.0234. As a result, the model achieved the desired level of accuracy on our preprocessed images from the INCART arrhythmia dataset. The delivered results of all the measured matrices and minimum validation loss from both experiments are depicted in Table 4. From Tables 2–4, it is observed that the average and overall values for all measured metrics in both experiments are almost the same despite data and features variability of ECG signals in both datasets (MIT-BIH and INCART). This also indicates the generalization of the proposed model.

The graphs for the three matrices such as accuracy, $F_{1\text{-score}}$, and recall in E_1 and E_2, respectively, are shown in Figures 7(a) and 7(b). It is clear from these graphs that the values of these matrices grew as the number of epochs increased and became nearly steady from 61 epochs in E_1 (Figure 7(a)) and 75 epochs in E2 (Figure 7(b)). The initial changes in the graphs are sudden since it takes some time for the testing samples to adapt to the trained model.

The trained model on MIT-BIH in E_1 and INCART in E_2 is also tested in E_3 and E_4, respectively, with MIT-BIH supraventricular. The reached evaluated average values of all performance metrics (average accuracy, precision, recall, and $F_{1\text{-score}}$) in E_3 and E_4 are figured out by the achieved confusion matrices, demonstrated in Figures 8(a) and 8(b), respectively. A summary of all reached metrics from the confusion matrices depicted in Figures 8(a) and 8(b) is illustrated in Table 5. The obtained average accuracy, $F_{1\text{-score}}$, recall, and precision from Figure 8(a) are 0.9985, 0.9639, 0.9992, and 0.9375, respectively, whereas from Figure 8(b), the reached average accuracy, $F_{1\text{-score}}$, recall, and precision are 0.9997, 0.9919, 0.9998, and 0.9844, respectively. The overall achieved accuracy, $F_{1\text{-score}}$, recall, and precision in E_3 are 0.9970, 0.9639, 0.9992, and 0.9375 respectively, while in E_4, the overall reached accuracy, $F_{1\text{-score}}$, recall, and precision are 0.9994, 0.9919, 0.9998, and 0.9844, respectively, demonstrated in Table 6. Tables 5 and 6 show that the average and overall values for all measured metrics in both experiments are almost identical, which also expresses the generalization of the proposed model.

Table 4: The comparison of all evaluation metrics and validation loss for both experiments.

Evaluation matrices/validation loss	E_1	E_2
Recall	0.9963	0.9942
$F_{1\text{-score}}$	0.9891	0.9891
Accuracy	0.9980	0.9963
Precision	0.9834	0.9894
Minimal validation loss	0.0233	0.0234

The trained model on MIT-BIH (E_1) and INCART (E_2) datasets is scored by E_5 and E_6, respectively, with MIT-BIH supraventricular using a transfer learning mechanism. The reached evaluated average values of all performance metrics (average accuracy, precision, recall, and $F_{1\text{-score}}$) in E_5 and E_6 could be figured out from the achieved confusion matrices, demonstrated in Figures 9(a) and 9(b), respectively. A summary of all metrics from the confusion matrices depicted in Figures 9(a) and 9(a) is illustrated in Table 7. The average accuracy, $F_{1\text{-score}}$, recall, and precision in E_5 are 0.9983, 0.9892, 0.9927, and 0.9859, respectively, whereas in E_6, the reached average accuracy, $F_{1\text{-score}}$, recall, and precision are 0.9994, 0.9955, 0.9970, and 0.9939, respectively. The overall achieved accuracy, $F_{1\text{-score}}$, recall, and precision in E_5 are 0.9970, 0.9892, 0.9927, and 0.9859, respectively. In contrast, the overall reached accuracy, $F_{1\text{-score}}$, recall, and precision are 0.9987, 0.9954, 0.9971, and 0.9939, respectively in E_6, demonstrated in Table 8. From Tables 7 and 8, it is also observed that the average and overall values for all measured metrics in both experiments are nearly identical, indicating that the proposed model is generalizable. The loss curves (training and testing) for E_5 are shown in Figure 10(a). The curves are almost stable to 40 epochs. The model is halted at only 72 epochs due to the use of early stopping feature in our developed training and testing module. It is also observed from Figure 10(a) that the developed model completes the training and validation process without facing any overfitting issues with the minimum validation loss of 0.0236. A similar scenario is also observed in Figure 10(b) for E_6,

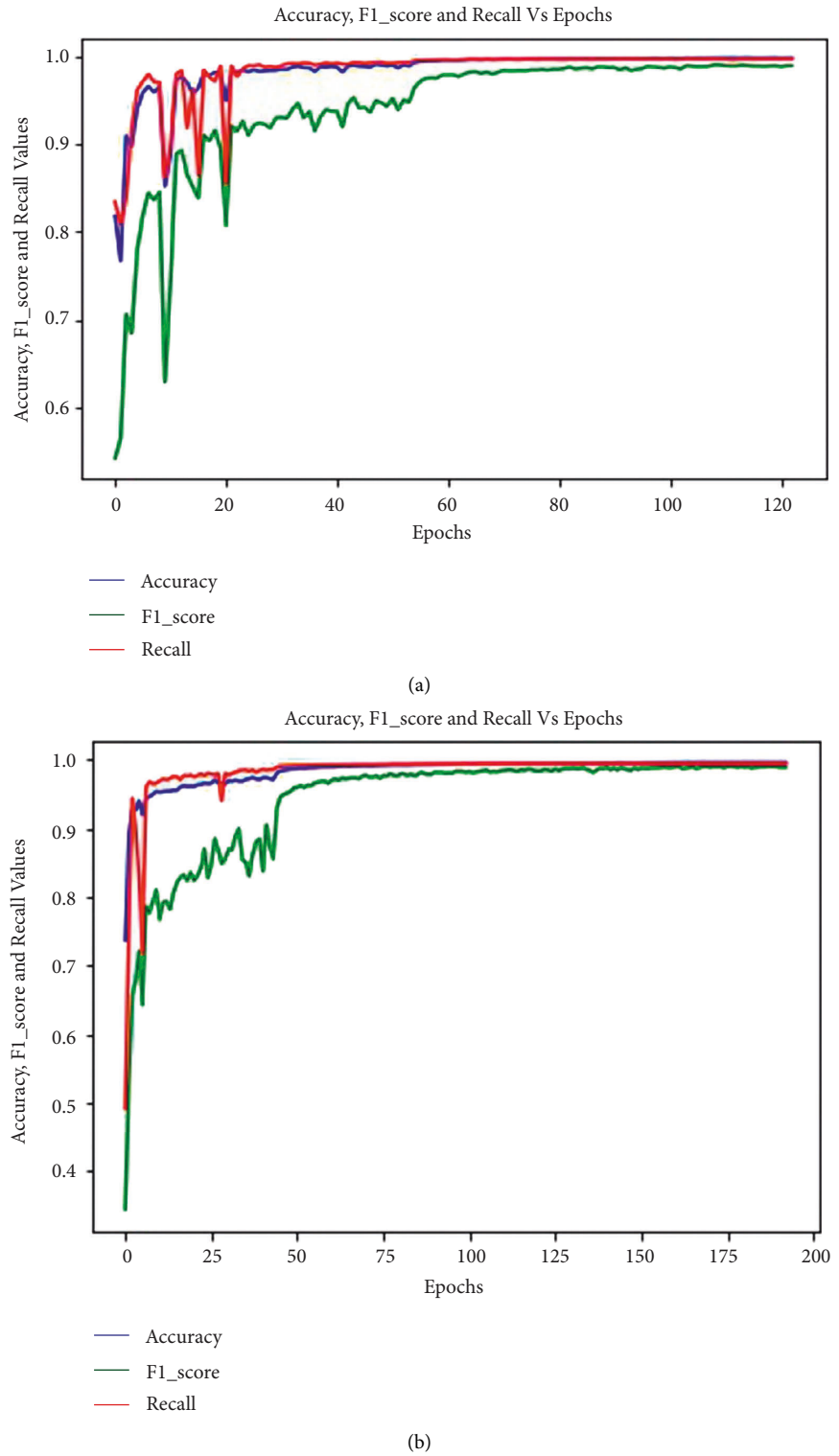

Figure 7: Graphs for the three matrices such as accuracy, $F_{1\text{-score}}$, and recall in (a) E_1 and (b) E_2.

where the loss curves almost remained stable from 60 epochs. The model is halted at 78 epochs with the same minimum validation loss.

The trained model on MIT-BIH in E_1 and INCART in E_2 is evaluated with the European ST-T database in E_7 and E_8, respectively. The achieved confusion matrices, as seen in Table 9, quantify the reached evaluated average values of all performance metrics (average accuracy, precision, recall, and $F_{1\text{-score}}$) in E_7 and E_8. In E_7, the overall accuracy, $F_{1\text{-score}}$, recall, and precision are 0.9990, 0.9664, 0.9802, and 0.9523,

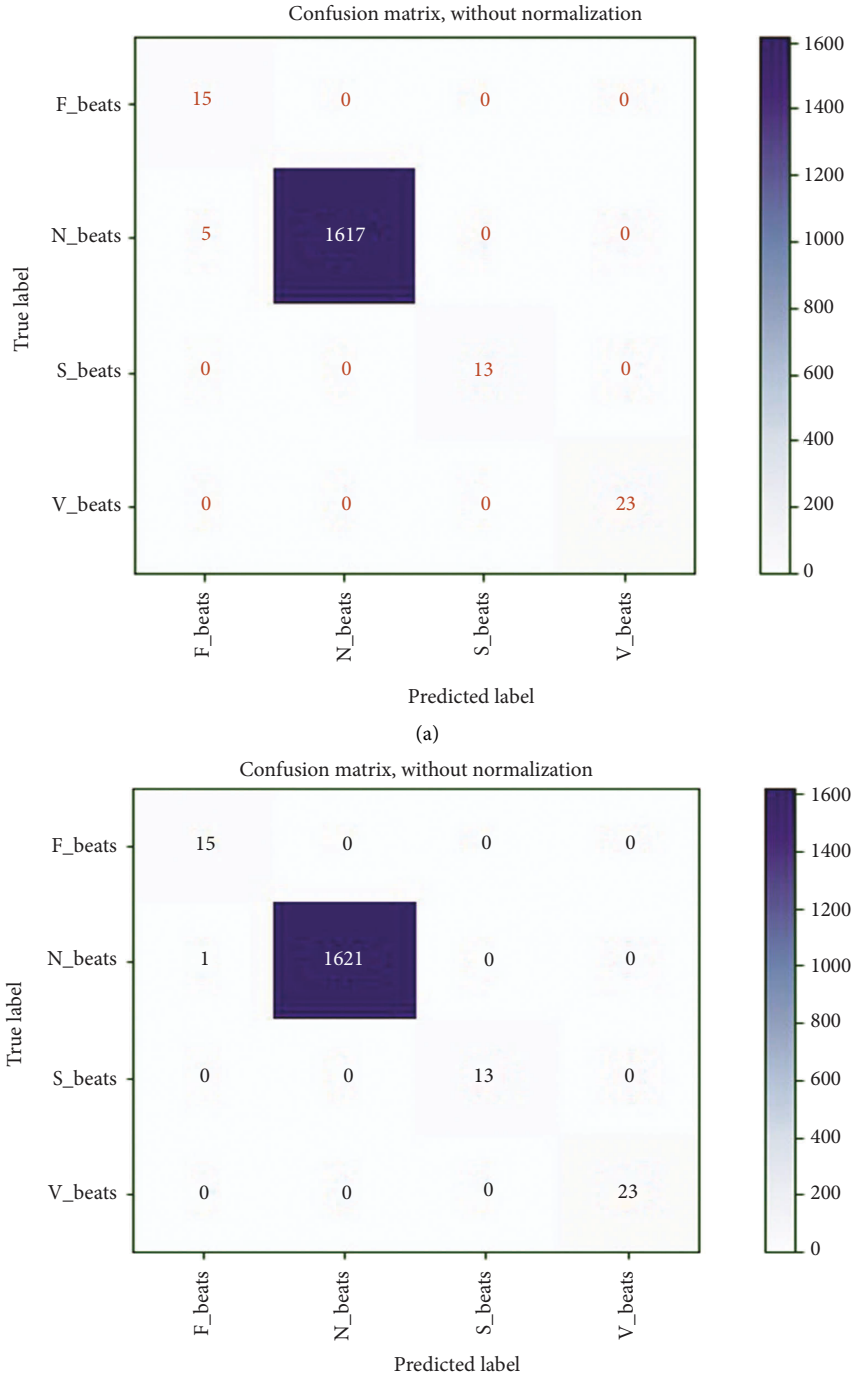

Figure 8: Reached confusion matrix in (a) E_3 and (b) E_4.

respectively, whereas in E_8, the overall accuracy, $F_{1\text{-score}}$, recall, and precision are 0.9995, 0.9802, 0.9865, and 0.9742. Using a transfer learning technique, the trained models on the MIT-BIH (E_1) and INCART (E_2) datasets were further scored by E_9 and E_{10} using the European ST-T database, respectively. The achieved confusion matrix, shown in Table 10, could be used to determine the evaluated average values of all performance indicators (average accuracy, precision, recall, and $F_{1\text{-score}}$) in E_9 and E_{10}. When comparing to E_9, the overall attained accuracy, $F_{1\text{-score}}$, recall, and precision in E_9 are 0.9987, 0.9839, 0.9912, and 0.9733, respectively, while these are 0.9995, 0.9901, 0.9959, and 0.9847 in E_{10}. Figure 11(a) depicts the loss curves (training and testing) for E_9. The curves are nearly stable after 40 epochs. Because of the early stopping feature, the model is halted after only 72 epochs. It is also clear from Figure 11(a) that the developed model successfully completes the training and validation processes with a validation

Table 5: A summary of all evaluated metrics from confusion matrix depicted in Figures 8(a) and 8(b).

Accuracy (%)		Precision (%)		Recall (%)		F_{1score} (%)	
For E_3							
N	99.70	N	100.0	N	99.69	N	99.85
S	100.0	S	100.0	S	100.0	S	100.0
V	100.0	V	100.0	V	100.0	V	100.0
F	99.70	F	75.00	F	100.0	F	85.71
Average	99.85	Average	93.75	Average	99.92	Average	96.39
For E_4							
N	99.94	N	100.0	N	99.94	N	99.97
S	100.0	S	100.0	S	100.0	S	100.0
V	100.0	V	100.0	V	100.0	V	100.0
F	99.94	F	93.75	F	100.0	F	96.77
Average	99.97	Average	98.44	Average	99.98	Average	99.19

Table 6: The comparison of all reached metrics in E_3 and E_4.

Evaluation matrices	E_3	E_4
Recall	0.9992	0.9998
$F_{1\text{-score}}$	0.9639	0.9919
Accuracy	0.9970	0.9994
Precision	0.9375	0.9844

loss of 0.0236. A similar scenario is shown in Figure 11(b) for E_{10}, where the loss curves are nearly stable after 85 epochs and the model is stopped at 78 epochs with the same minimum validation loss.

3.2. Discussions. In this section, we will first discuss the issues of why our proposed deep approach provides satisfactory results in arrhythmia recognition. First, deep CNNs have learned the dominant features with their convolution layers, and the outcome is investigated with the resulting classifier. Furthermore, the class activation map from the CNN-based models could be easily reached for the visual analysis compared to RNN and LSTM employed for the sequential modeling. Visual analysis is a significant factor in medical diagnosis. Second, the most crucial stage of the experiment is segmenting and transforming ECG signals into beat images, where R-peak detection or beat segmentation is reached based on a well-known and influential algorithm (Pan-Tompkins) on the arrhythmia datasets. Third, DenseNet architecture has some inspirable benefits compared to other CNN architectures, such as being easy to train by delivering the promoted stream of information, reusing features, fewer parameters to train, and alleviating vanishing gradient problems. Forth, some diverse mechanisms are used such as early stopping [46] and on-the-fly augmentation [49] that help to stop overfitting of the model, weighted random sampler [47] to reduce the class imbalance problem, Adam optimizer [48] to converge the model quickly with the minimum validation loss, and proper initialization of model layers [50]. In addition, data imbalance problems negatively affect the performance of a model. So, in this study, we have used a simple class weighting strategy to resolve the issue of data imbalance. The smaller the class size scores, the more considerable the class weight from the training samples. That class weight is utilized to measure the weighted loss during training so that loss from the smaller class is more significant than the larger class. The strategy is also more apparent from our expressed used loss function in Section 2.5. Previously, some researchers attempted to resolve the class imbalance problem in different ways. Al Rahhal et al. [41] addressed a scenario to handle the data imbalance problem using the focal loss technique [42]. An interesting study by Rajesh and Dhuli [12] with three-level data preprocessing approaches: ROU (random oversampling and undersampling), DBB (distribution-based balancing), and synthetic minority oversampling technique with random undersampling (SMOTE + RU) was observed to handle the data imbalance problem. Our employed cross-entropy loss function can also handle such data imbalance issues. It is demonstrated in [57] that, without using the class weighting strategy, the model's performance is not improved with only focal loss. Moreover, many prior promising models in this sense demand enormous in-depth domain ideas for the preprocessing and feature extraction. On the other hand, our proposed method needs the minimum skill in preprocessing and feature extraction while obtaining better performance even compared to deep learning approaches, as demonstrated in Table 11. The developed model extracts desirable activation on intensity, edge, and shape of the peak of our preprocessed beat images. The background is not so important here because extracted beats appear only in a small portion of the image. The satisfactory performance of the developed model represents the learned features from the images after training. The model is well correlated and embedded with the desired classes concerning the high dimensional (mapped in two dimensions) feature space, which is more evident from the confusion graph and evaluated matrices. So, we are assuming that the averaging procedure of representation performs well. The morphological and dynamic characteristics of all datasets are analogous despite data and features variability of ECG signals, and identical experimental dealing is performed on all datasets. Furthermore, the reached performance results on all datasets with the developed model are almost identical, as illustrated in Tables 2 to 10. This expresses the generalization of the developed model.

We have compared our findings with [12, 36–39, 58, 59, 61, 62] in Table 11, where the authors employed almost similar approaches with our works in case of 2D CNN. In the table, we have only placed the results from E_1 and E_2. The results demonstrate that our developed DenseNet outperforms compared to others. It represents the effectiveness of the developed model. $F_{1\text{-score}}$ is an effective performing metric compared to accuracy on imbalanced datasets, justifying the sensitivity and exactness of a model, where recall and precision are summed up as the harmonic mean. It is observed from the table that the scores of all measured metrics in both experiments on MIT-BIH and INCART datasets, respectively, are almost identical, which indicates the generalization of the proposed method. From Table 11, it is also shown that all 2D CNN approaches deliver better results compared to 1D CNN as well as hand-crafted features

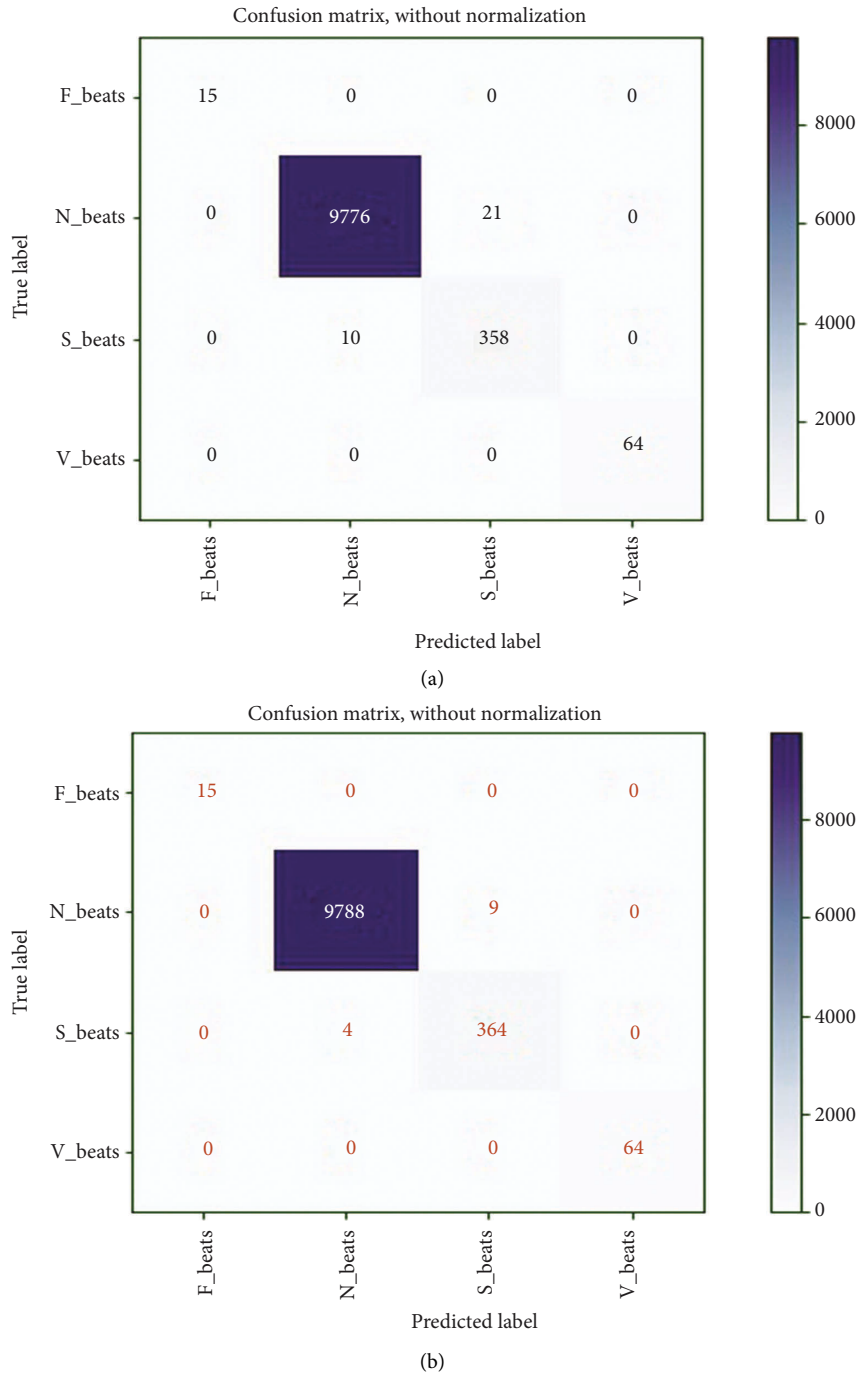

Figure 9: Reached confusion matrix in (a) E_5 and (b) E_6.

engineering techniques. We have also tested our proposed method in 1D CNN form (with time series data) following experiments 1 and 2. The achieved results in both experiments are poor compared to all experiments (E_1–E_{10}) in 2D CNN. The reached accuracies are 97.56% and 97.65%, respectively, following E_1 and E_2. 1D CNNs are less versatile than 2D CNNs. So, the transformation mechanism of sequential data of beats into their equivalent beat images is a promising strategy. Indeed, it is not practicable to thoroughly compare our study with the previous studies because various strategies are used in the preprocessing stage and model designing. R-R intervals or R-peaks, duration, and amplitude of the QRS complex of ECG are highly sensitive to its dynamic and morphology. The transformation-based method reduces the problem of strict time alignment; it ignores the scoring of fiducial points of heartbeats. The nonlinear and nonstationary characteristics of ECG heartbeats due to the heart's episodic/irregular electrical conduction are the significant factors behind such problems. Moreover, heartbeat-based arrhythmias are classified mainly

Table 7: A summary of all evaluated metrics from confusion matrix depicted in Figures 9(a) and 9(b).

Accuracy(%)		Precision (%)		Recall (%)		F_{1score} (%)	
For E_5							
N	99.67	N	99.90	N	99.79	N	99.84
S	99.67	S	94.46	S	97.28	S	95.85
V	100.0	V	100.0	V	100.0	V	100.0
F	100.0	F	100.0	F	100.0	F	100.0
Average	99.83	Average	98.59	Average	99.27	Average	98.92
For E_6							
N	99.87	N	99.96	N	99.90	N	99.93
S	99.87	S	97.59	S	98.91	S	98.25
V	100.0	V	100.0	V	100.0	V	100.0
F	100.0	F	100.0	F	100.0	F	100.0
Average	99.94	Average	99.39	Average	99.70	Average	99.55

Table 8: The comparison of all reached metrics in E_5 and E_6.

Evaluation matrices/validation loss	E_5	E_6
Recall	0.9927	0.9971
$F_{1\text{-score}}$	0.9892	0.9954
Accuracy	0.9970	0.9987
Precision	0.9859	0.9939
Minimal validation loss	0.0236	0.0236

into two categories, (i) tachycardia and life-threatening ventricular fibrillation that need early diagnosing and treatment with the defibrillator, and (ii) non-life-threatening arrhythmias but require further treatment. AAMI divides non-life-threatening arrhythmias into five classes (N, S, V, F, and Q), where each beat category significantly differs in morphology from others and holds some subclasses with various shapes that introduce a massive challenge for physicians to diagnose manually. The N class includes normal (N), right bundle branch block (RBBB), left bundle branch block (LBBB), atrial escape (e), and nodal (junctional) escape (j) beats; S class includes aberrant atrial premature (a), supraventricular premature (S), nodal (junctional) premature (J), and atrial premature (A) beats; V class includes ventricular escape (E) and premature ventricular contraction-PVC (V) beats; F class only includes the only fusion of normal and ventricular (F) beats; Q class includes paced (/), unclassified (Q), and fusion of normal and paced (f) beats but this class is not considered in our study due to the involvement of paced and unclassified beats. Moreover, an automatic diagnosis with deep learning methods compensates the manual interpretations effectively and efficiently and visual errors of physicians with reduced workloads and medical costs. Our study of automatic arrhythmia recognition is based on AAMI recommendations and provides the desired outcomes. It is observed from the confusion matrix graphs in Figures 5(a), 6(a), 8, and 9 and Tables 9 and 10 that N is more noticeable compared to the remaining beats; again V and S beats are more remarkable than F. It exposes that their ratios are misbalancing, but the proposed method classifies each category properly without biasing towards their majority class.

Experiments 3, 4, 7, and 8 show that the proposed model is only tested with two different unseen datasets (MIT-BIH supraventricular and European ST-T) after training with MIT-BIH and INCART datasets. The outcomes of both experiments are satisfactory, which expresses the model's effectiveness. As a result, the proposed method could prosper in wearable devices such as medical bracelets, wristwatches, and vests for instantaneous cardiac conditions. It could also be a booming approach in telemedicine due to its lightweight compared to fundamental DenseNets (DenseNet-121, DenseNet-169, DenseNet-201, and DenseNet-264) [35]. The lightweight of the proposed model also indicates its more usefulness in storage constraint devices such as mobile, portable/wearable healthcare devices. Transfer learning is becoming popular nowadays due to handling the challenge of huge data demanding for deep model training (the most private and publicly available datasets are currently of small volume). In this approach, the model is not trained from scratch, so it helps to reduce the overfitting problem of a deep model [32] and enhance the computational efficiency. The mechanism could also be a prosperous solution for storage constraint devices in real-life applications. We evaluated our proposed method using this mechanism in experiments 5, 6, 9, and 10. We achieved satisfactory findings by considering only five records/individuals from a different dataset. We have also evaluated the proposed model with ten records/individuals from the same dataset and received almost the same results, which also expresses the model's generalization.

However, there are a few open challenges instead of achieving satisfactory results with our proposed method. First is the intrapatient paradigm in E_1, E_2, E_3, E_4, E_7, and E_8, where the same patient heartbeats are likely to arrive in training and testing sets. This circumstance may lead to biased results. The patient-specific study could be the solution to this challenge. Second, arrhythmia recognition based on a single beat has some limitations to a few extents as the relevant distinction. Short segments from the ECG signals or adaptive beat size length segmentation could be the interpretation of this issue. Third, there is no doubt that it is computationally intensive, so it is more applicable for offline applications in medicals and clinics compared to resource constraint devices. A method's computational efficiency varies with the hardware configuration of the utilized PC. Deep learning-based methods require high computational complexity compared to morphological-based techniques. Hence, these are slower in real-life applications [63]. So, it is suggested that deploying deep learning-based methods in real-life applications where bid data dealing is required is more feasible. Forth is efficiency; it will be hard to deploy our proposed method into portable healthcare devices for real-life applications. In that case, designing the lightweight deep model is directed, or models compression techniques such as weight sharing and knowledge distillation are used. Fifth is integration with expert features; it is hard to integrate a trained deep model with the existing expert features. To handle the issue, domain expert knowledge could be directed to design a deep model. Sixth is noise robustness: a deep method that automatically extracts all features from the

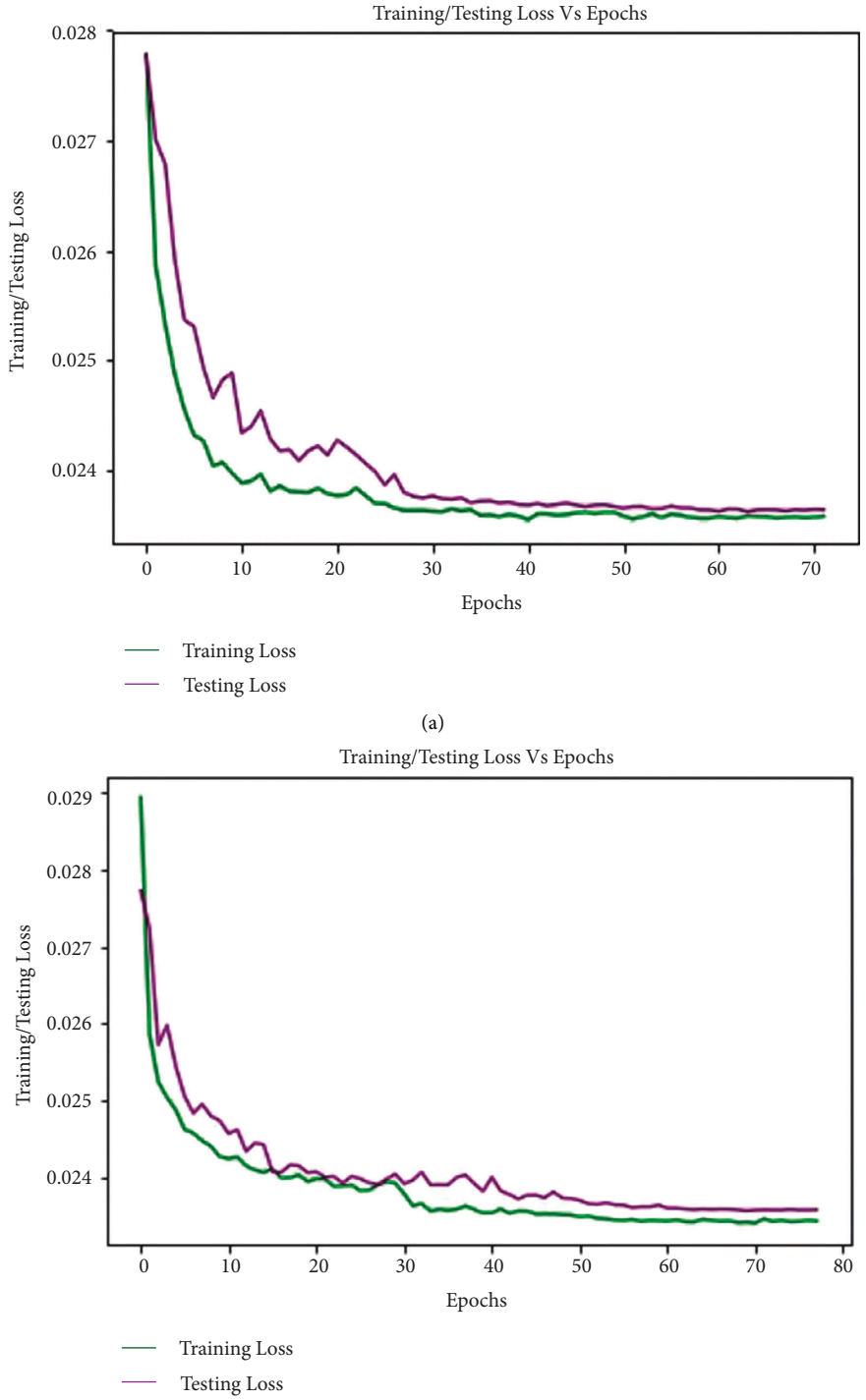

Figure 10: Training and testing loss curve for (a) E_5 and (b) E_6.

signals, including different types of real-world noises, which may lead to incorrect results. So, some researchers tried to resolve the issue by fitting denoising/filtering techniques before commencing data into the input of deep models, but some valuable information could be omitted in that case [64]. So, any denoising/filtering technique is not employed on the raw information in our study. Finally, the major failure case of our proposed method is the inability to identify all categories of images correctly available in real worlds including the identification of all beat images properly, which is demonstrated in Figures 5(a), 6(a), 8, and 9 and Tables 9 and 10. However, 2D CNN-based deep method is a promising direction for diagnosing various categories of cardiovascular diseases in offline and online approaches.

Table 9: The reached confusion matrix and average values of evaluated metrics in E_7 and E_8.

		Predicted label				Accuracy (%)	Precision (%)	Recall (%)	F_{1_score} (%)
		F	N	S	V				
E_7									
True label	F	62	0	0	1	99.92	95.27	98.03	96.62
	N	0	10585	10	0				
	S	4	0	75	0				
	V	0	1	0	90				
E_8									
True label	F	62	0	1	0	99.94	97.41	98.68	98.03
	N	0	10590	5	0				
	S	2	0	77	0				
	V	0	1	0	90				

Table 10: The reached confusion matrix and average values of evaluated metrics in E_9 and E_{10}.

		Predicted label				Accuracy (%)	Precision (%)	Recall (%)	F_{1_score} (%)
		F	N	S	V				
E_7									
True label	F	119	0	0	2	99.89	97.37	99.15	98.38
	N	2	43500	10	4				
	S	0	0	166	2				
	V	0	2	0	362				
E_8									
True label	F	120	0	0	1	99.98	98.51	99.58	99.03
	N	1	43506	6	3				
	S	0	1	167	0				
	V	0	0	1	363				

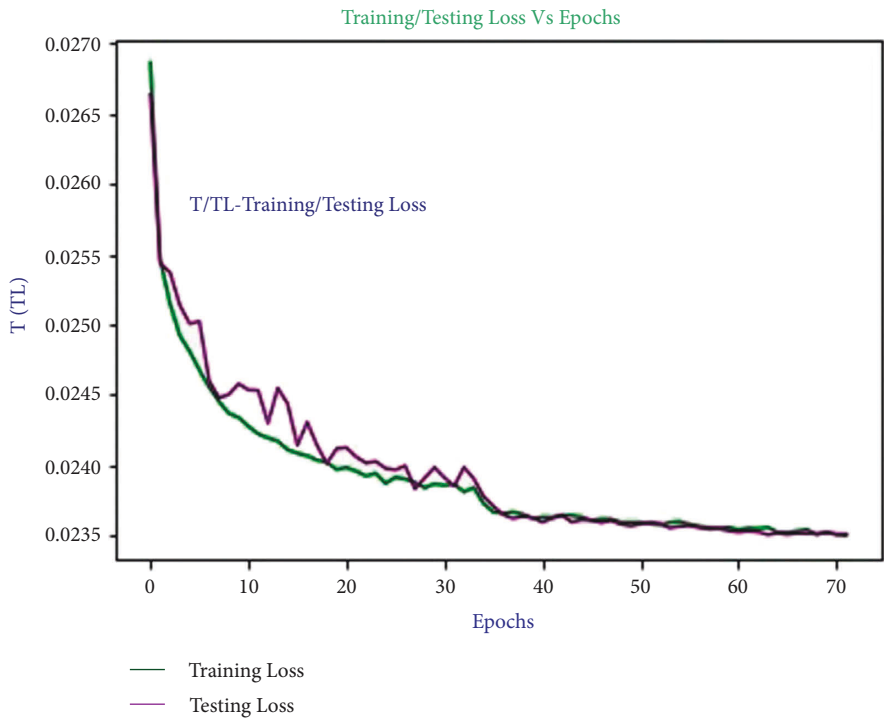

(a)

Figure 11: Continued.

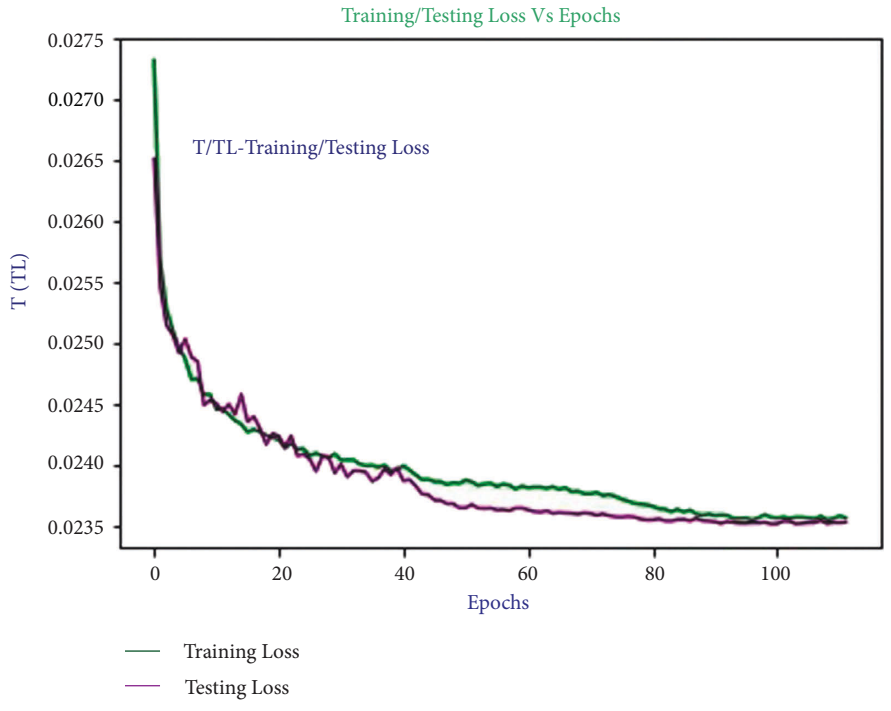

(b)

Figure 11: Training and testing loss curve for (a) E_9 and (b) E_{10}.

Table 11: Comparative table of our work with the previous approaches.

Classifier type/approach	Class categories	Accuracy	Precision	Recall	$F1$-score
2D CNN (proposed) (on MIT-BIH-E_1)	4	99.80**	98.34**	99.63**	98.91**
2D CNN (proposed) (on INCART-E_2)	4	99.63**	98.94**	99.42**	98.91**
2D CNN [36]	8	98.92*	—	97.26*	98.00*
		99.11**	—	97.91**	98.00**
2D CNN [39]	8	99.05*	—	97.85*	—
		98.90**	—	97.20**	
2D CNN [39] AlexNet	8	98.85*	—	97.08*	—
		98.81**	—	96.81**	
2D CNN [39] VGGNet	8	98.63*	—	96.93*	—
		98.77**	—	97.26**	
2D CNN [37]	4	98.50*	—	—	—
2D CNN [38]	8	99.02**	—	—	—
2D CNN [58]	5	99.00*	—	—	—
2D CNN [59]	5	99.70**	—	99.70**	—
2D CNN [60]	5	99.62*	—	92.24*	94.00*
1D CNN [36]	8	97.80*	—	—	—
1D CNN [58]	5	90.93*	—	—	—
1D CNN [38]	5	97.38*	—	—	—
CNN-LSTM [61]	5	98.10*	—	97.50*	—
LSTM, FL [62]	8	99.26*	—	99.26*	—
DBB, AdaBoost [12]	5	99.10*	—	97.90*	—

**with augmentation on-the-fly or manual, *without augmentation, FL: focal loss, DBB: distribution-based balancing.

4. Conclusions

In this study, a 2D CNN method with an effective DenseNet is proposed for arrhythmias recognition on four different imbalanced datasets with various experiments. The findings from all experiments demonstrate that the proposed method outperforms the performance of state-of-the-art models, which validates the proposed method's effectiveness and generalization. The key convenience of the developed model is that each layer can access the gradients directly from the input signals and loss function, resulting in improved gradients and information flow across the network with various regularization techniques. These regularizing effects alleviate the overfitting challenges on classification tasks

with the confined training data sizes. Moreover, our experimental results from all experiments illustrate that the proposed model provides satisfactory results in resolving the class imbalance issue of all used datasets. The findings also indicate that the performance of the developed model remains almost identical despite using various strategies in various experiments for four heterogeneous datasets. This expresses better applicability and scalability of the proposed method. So, the proposed method could be a helpful tool for cardiologists' clinical decision support systems in offline or online approaches. The factors behind such successes are (i) because of using indicated regularization techniques, (ii) advantages of the fundamental DenseNets model compared to others such as features reusing, the punctuation of features propagation, and less trained parameters to be required, (iii) proper segmentation and transformation of beat images, and (iii) because of using weighted categorical cost function and weighted random sampler in all experiments. In the future, we will look into a hybrid model incorporating LSTM with the developed model. We have also planned to conduct a study with the clinical data or data from our developed flexible sensor to test the proposed method, which will be more applicable in real-life applications. It is also possible to employ the study in other biomedical engineering applications, especially in neurological diseases such as Alzheimer's, epilepsy.

Data Availability

The data used to support the findings of the study are available from the Mr. Hadaate Ullah (hadaate@std.uestc.edu.cn) upon request.

Conflicts of Interest

The authors declare that there are no conflicts of interest.

Authors' Contributions

H.U., M.B.B.H., and F.A. were assigned in the conceptualization, designing, validation, revision, and drafting; S., A.Y.M., and M.S.I. were assigned in the data collection, critically reviewing, and proofreading; Z.A., T.P., M.G., Y.L, and D.L. were assigned in the guidance and proofreading. All authors have read and agreed to the published version of the manuscript.

Acknowledgments

The authors are thankful to Prof. Wu, Prof. Naseem, Prof. Singh, Prof. Chandel, Dr Renu Rana, Dr Ijaz Gul, and Dr Nasir Ilyas for the useful discussion in the improvement of the article. The authors also acknowledge IoT Research Center, College of Computer Science and Software Engineering, Shenzhen University, Shenzhen, and State Key Laboratory of Electronic Thin Films and Integrated Devices, School of Materials and Energy, and School of Computer Science and Engineering, University of Electronic Science and Technology of China, Chengdu, for providing good environment for this work. This work was supported by the National Natural Science Foundation of China (Grant nos. U2001207, 61872248, 61825102, 61771100, and 62001083), Guangdong NSF (Grant no. 2017A030312008), Shenzhen Science and Technology Foundation (Grant nos. ZDSYS20190902092853047 and R2020A045), the Project of DEGP (Grant no. 2019KCXTD005), the Guangdong "Pearl River Talent Recruitment Program" (Grant no. 2019ZT08X603), the Science and Technology Department of Sichuan Province (Grant no. 2021YFG0322), the Science and Technology Research Program of Chongqing Municipal Education Commission (Grant no. KJZD-K202114401), Fundamental Research Funds for the Central Universities, UESTC (Grant no. ZYGX2021YGLH002), and Sichuan Science and Technology Program (Grant no. 2021YFH0093).

References

[1] N. Keidar, Y. Elul, A. Schuster, and Y. Yaniv, "Visualizing and quantifying irregular heart rate irregularities to identify atrial fibrillation events," *Frontiers in Physiology*, vol. 12, Article ID 637680, 2021.

[2] S. A. Malik, S. A. Parah, and B. A. Malik, "Power line noise and baseline wander removal from ECG signals using empirical mode decomposition and lifting wavelet transform technique," *Health Technology*, vol. 12, no. 1, pp. 745–756, 2022.

[3] C. Bock, P. Kovacs, P. Laguna, J. Meier, and M. Huemer, "Ecg beat representation and delineation by means of variable projection," *IEEE Transactions on Biomedical Engineering*, vol. 68, no. 10, pp. 2997–3008, 2021.

[4] M. Lee and J. H. Lee, "A robust fusion algorithm of LBP and IMF with recursive feature elimination-based ECG processing for QRS and arrhythmia detection," *Applied Intelligence*, vol. 52, no. 1, pp. 939–953, 2022.

[5] S. Saxena, R. Vijay, G. Saxena, and P. Pahadiya, "Classification of cardiac signals with automated R-peak detection using wavelet transform method," *Wireless Personal Communications*, vol. 123, no. 1, pp. 655–669, 2022.

[6] A. Chandrasekar, D. D. Shekar, A. C. Hiremath, and K. Chemmangat, "Detection of arrhythmia from electrocardiogram signals using a novel Gaussian assisted signal smoothing and pattern recognition," *Biomedical Signal Processing and Control*, vol. 73, Article ID 103469, 2022.

[7] M. Alfaras, M. C. Soriano, and S. Ortin, "A fast machine learning model for ECG-based heartbeat classification and arrhythmia detection," *Frontiers in Physiology*, vol. 7, p. 103, 2019.

[8] S. Bhattacharyya, S. Majumder, P. Debnath, and M. Chanda, "Arrhythmic heartbeat classification using ensemble of random forest and support vector machine algorithm," *IEEE Transaction. Artificial. Intelligent.*vol. 2, no. 3, pp. 260–268, 2021.

[9] D. Lai, M. B. B. Heyat, F. I. Khan, and Y. Zhang, "Prognosis of sleep bruxism using power spectral density approach applied on EEG signal of both EMG1-EMG2 and ECG1-ECG2 channels," *IEEE Access*, vol. 7, pp. 82553–82562, 2019.

[10] M. B. B. Heyat, D. Lai, F. I. Khan, and Y. Zhang, "Sleep bruxism detection using decision tree method by the combination of C4-P4 and C4-A1 channels of scalp EEG," *IEEE Access*, vol. 7, pp. 102542–102553, 2019.

[11] U. R. Acharya, S. L. Oh, Y. Hagiwara et al., "A deep convolutional neural network model to classify heartbeats,"

Computers in Biology and Medicine, vol. 89, pp. 389–396, 2017.

[12] K. N. V. P. S. Rajesh and R. Dhuli, "Classification of imbalanced ECG beats using re-sampling techniques and AdaBoost ensemble classifier," *Biomedical Signal Processing and Control*, vol. 41, pp. 242–254, 2018.

[13] M. S. Iqbal, R. Abbasi, M. B. Bin Heyat et al., "Recognition of mRNA N4 acetylcytidine (ac4C) by using non-deep vs. Deep learning," *Applied Sciences*, vol. 12, no. 3, pp. 1344–1416, 2022.

[14] W. Yan and Z. Zhang, "Online automatic diagnosis system of cardiac arrhythmias based on MIT-BIH ECG database," *Journal of Healthcare Engineering*, vol. 2021, Article ID 1819112, 9 pages, 2021.

[15] B. N. Teelhawod, F. Akhtar, M. B. B. Heyat et al., "Machine learning in E-health: a comprehensive survey of anxiety," in *Proceedings of the International Conference on Data Analytics for Business and Industry, ICDABI 2021*, pp. 167–172, Sakheer, Bahrain, October 2021.

[16] F. Akhtar, M. B. B. Heyat, J. P. Li, P. K. Patel, and B. Guragai, "Role of machine learning in human stress: a review," in *Proceedings of the 2020 17th International Computer Conference on Wavelet Active Media Technology and Information Processing, ICCWAMTIP*, pp. 170–174, Chengdu, China, December. 2020.

[17] A. Y. Hannun, P. Rajpurkar, M. Haghpanahi et al., "Cardiologist-level arrhythmia detection and classification in ambulatory electrocardiograms using a deep neural network," *Nat. Med.*vol. 25, no. 1, pp. 65–69, 2019.

[18] S. Lyu and J. Liu, "Convolutional recurrent neural networks for text classification," *Journal of Database Management*, vol. 32, no. 4, pp. 65–82, 2021.

[19] H. Ullah, M. B. Bin Heyat, H. AlSalman et al., "An effective and lightweight deep electrocardiography arrhythmia recognition model using novel special and native structural regularization techniques on cardiac signal," *Journal of Healthcare Engineering*, vol. 2022, Article ID 3408501, 18 pages, 2022.

[20] Ö. Yildirim, "A novel wavelet sequence based on deep bidirectional LSTM network model for ECG signal classification," *Computers in Biology and Medicine*, vol. 96, pp. 189–202, 2018.

[21] C. Chen, Z. Hua, R. Zhang, G. Liu, and W. Wen, "Automated arrhythmia classification based on a combination network of CNN and LSTM," *Biomedical Signal Processing and Control*, vol. 57, Article ID 101819, 2020.

[22] B. Guragai, "A survey on deep learning classification algorithms for motor imagery," in *Proceedings of the 2020 International Conference on Microelectronics, ICM*, pp. 1–4, Aqaba, Jordan, December 2020.

[23] A. Y. Muaad, H. Jayappa, M. A. Al-antari, and S. Lee, "ArCAR: a novel deep learning computer-aided recognition for character-level Arabic text representation and recognition," *Algorithms*, vol. 14, no. 7, p. 216, 2021.

[24] B. Bin Heyat, Y. M. Hasan, and M. M. Siddiqui, "EEG signals and wireless transfer of EEG Signals," *Int. J. Adv. Res. Comput. Commun. Eng.*vol. 4, no. 12, pp. 10–12, 2015.

[25] M. Algarni, F. Saeed, T. Al-Hadhrami, F. Ghabban, and M. Al-Sarem, "Deep learning-based approach for emotion recognition using electroencephalography (EEG) signals using Bi-directional long short-term memory (Bi-LSTM)," *Sensors*, vol. 22, no. 8, p. 2976, 2022.

[26] M. B. B. Heyat, F. Akhtar, and S. Azad, "Comparative analysis of original wave and filtered wave of EEG signal used in the prognostic of bruxism medical sleep syndrome," *International Journal of Trend in Scientific Research and Development*, vol. 1, no. 1, pp. 7–9, 2016.

[27] O. AlShorman, M. Masadeh, M. B. B. Heyat et al., "Frontal lobe real-time EEG analysis using machine learning techniques for mental stress detection," *Journal of Integrative Neuroscience*, vol. 21, no. 1, p. 20, 2022.

[28] M. B. B. Heyat, F. Akhtar, M. H. Khan et al., "Detection, treatment planning, and genetic predisposition of bruxism: a systematic mapping process and network visualization technique," *CNS & Neurological Disorders - Drug Targets*, vol. 20, no. 8, pp. 755–775, 2021.

[29] O. El Gannour, S. Hamida, B. Cherradi et al., "Concatenation of pre-trained convolutional neural networks for enhanced covid-19 screening using transfer learning technique," *Electronics*, vol. 11, no. 1, p. 103, 2021.

[30] F. Akhtar, P. K. Patel, M. B. B. Heyat et al., "Smartphone addiction among students and its harmful effects on mental health, oxidative stress, and neurodegeneration towards future modulation of anti-addiction therapies: a comprehensive survey based on slr, Research questions, and network visualization techniques," *CNS & Neurological Disorders - Drug Targets*, vol. 21, 2022.

[31] M. B. Bin Heyat, F. Akhtar, A. Khan et al., "A novel hybrid machine learning classification for the detection of bruxism patients using physiological signals," *Applied Sciences*, vol. 10, no. 21, pp. 7410–7416, 2020.

[32] H. Ullah, Y. Bu, T. Pan et al., "Cardiac arrhythmia recognition using transfer learning with a pre-trained DenseNet," in *Proceedings of the 2021 IEEE 2nd International Conference on Pattern Recognition and Machine Learning (PRML)*, pp. 347–353, Chengdu, China, July 2021.

[33] K. Weimann and T. O. F. Conrad, "Transfer learning for ECG classification," *Scientific Reports*, vol. 11, no. 1, p. 5251, 2021.

[34] K. He, X. Zhang, S. Ren, and J. Sun, "Deep residual learning for image recognition," in *Proceedings of the 2016 IEEE Conference on Computer Vision and Pattern Recognition (CVPR)*, pp. 770–778, Las Vegas, NV, USA, June 2016.

[35] G. Huang, Z. Liu, L. Van Der Maaten, and K. Q. Weinberger, "Densely connected convolutional networks," in *Proceedings of the 2017 IEEE Conference on Computer Vision and Pattern Recognition (CVPR)*, pp. 2261–2269, Honolulu, HI, USA, July 2017.

[36] A. Ullah, S. M. Anwar, M. Bilal, and R. M. Mehmood, "Classification of arrhythmia by using deep learning with 2-D ECG spectral image representation," *Remote Sensing*, vol. 12, no. 10, p. 1685, 2020.

[37] P. Xu, H. Liu, X. Xie, S. Zhou, M. Shu, and Y. Wang, "Interpatient ECG arrhythmia detection by residual attention CNN," *Computational and Mathematical Methods in Medicine*, vol. 2022, Article ID 2323625, 13 pages, 2022.

[38] A. Ullah, S.S. Rehman, and R. M.M. Mehmood, "A hybrid deep CNN model for abnormal arrhythmia detection based on cardiac ECG signal," *Sensors*, vol. 21, no. 3, pp. 951–1013, 2021.

[39] T. J. Jun, H. M. Nguyen, D. Kang, D. Kim, D. Kim, and Y. H. Kim, "ECG Arrhythmia Classification Using a 2-D Convolutional Neural Network," 2018, http://arxiv.org/abs/1804.06812.

[40] J. Rubin, S. Parvaneh, A. Rahman, B. Conroy, and S. Babaeizadeh, "Densely connected convolutional networks for detection of atrial fibrillation from short single-lead ECG recordings," *Journal of Electrocardiology*, vol. 51, no. 6, pp. S18–S21, 2018.

[41] M. M. Al Rahhal, Y. Bazi, H. Almubarak, N. Alajlan, and M. Al Zuair, "Dense convolutional networks with focal loss and image generation for electrocardiogram classification," *IEEE Access*, vol. 7, pp. 182225–182237, 2019.

[42] T. Y. Lin, P. Goyal, R. Girshick, K. He, and P. Dollar, "Focal loss for dense object detection," *IEEE Transactions on Pattern Analysis and Machine Intelligence*, vol. 42, no. 2, pp. 318–327, 2020.

[43] C. Du, P. X. Liu, and M. Zheng, "Classification of imbalanced electrocardiosignal data using convolutional neural network," *Computer Methods and Programs in Biomedicine*, vol. 214, Article ID 106483, 2022.

[44] K. R. M. Fernando and C. P. Tsokos, "Dynamically weighted balanced loss: class imbalanced learning and confidence calibration of deep neural networks," *IEEE Transactions on Neural Networks and Learning Systems*, vol. 33, no. 7, pp. 2940–2951, 2022.

[45] S. Ioffe and C. Szegedy, "Batch normalization: accelerating deep network training by reducing internal covariate shift," in *Proceedings of the 2015 32nd International Conference on Machine Learning*, vol. 1, pp. 448–456, Lille, France, July 2015.

[46] S. Garatti and M. C. Campi, "Complexity is an effective observable to tune early stopping in scenario optimization," *IEEE Transactions on Automatic Control*, p. 1, 2022, https://ieeexplore.ieee.org/document/9721591.

[47] M. Shekelyan, G. Cormode, P. Triantafillou, A. Shanghooshabad, and Q. Ma, "Weighted Random Sampling over Joins," 2022, https://arxiv.org/pdf/2201.02670.pdf.

[48] D. P. Kingma and J. L. Ba, "Adam: A Method for Stochastic Optimization," in *Proceedings of the 3rd International Conference on Learning Representations, ICLR 2015*, May 2015.

[49] T. K. Lam, M. Ohta, S. Schamoni, and S. Riezler, "On-the-fly aligned data augmentation for sequence-to-sequence ASR," *Interspeech 2021*, vol. 6, pp. 4481–4485, 2021.

[50] K. He, X. Zhang, S. Ren, and J. Sun, "Delving deep into rectifiers: surpassing human-level performance on imagenet classification," in *Proceedings of the 2015 IEEE International Conference on Computer Vision (ICCV)*, no. 1, pp. 1026–1034, Santiago, Chile, December 2015.

[51] R. Ghorbani Afkhami, G. Azarnia, and M. A. Tinati, "Cardiac arrhythmia classification using statistical and mixture modeling features of ECG signals," *Pattern Recognition Letters*, vol. 70, pp. 45–51, 2016.

[52] A. Y. Muaad, H. Jayappa Davanagere, J. V. B. Benifa et al., "Artificial intelligence-based approach for misogyny and sarcasm detection from Arabic texts," *Computational Intelligence and Neuroscience*, vol. 2022, no. 1, 9 pages, Article ID 7937667, 2022.

[53] D. Jahin, I. J. Emu, S. Akter, M. J. Patwary, M. A. S. Bhuiyan, and M. H. Miraz, "A novel oversampling technique to solve class imbalance problem: a case study of students' grades evaluation," in *Proceedings of the 2021 International Conference on Computing, Networking, Telecommunications & Engineering Sciences Applications (CoNTESA)*, Tirana, Albania, October 2021.

[54] A. K. Nawabi, S. Jinfang, R. Abbasi et al., "Segmentation of drug-treated cell image and mitochondrial-oxidative stress using deep convolutional neural network," *Oxidative Medicine and Cellular Longevity*, vol. 2022, Article ID 5641727, 14 pages, 2022.

[55] M. B. Bin Heyat, F. Akhtar, S. J. Abbas et al., "Wearable flexible Electronics based cardiac electrode for researcher mental stress detection system using machine learning models on single lead electrocardiogram signal," *Biosensors*, vol. 12, no. 6, p. 427, 2022.

[56] A. Sultana, K. Rahman, M. B. B. Heyat, Sumbul, F. Akhtar, and A. Y. Muaad, "Role of inflammation, oxidative stress, and mitochondrial changes in premenstrual psychosomatic behavioral symptoms with anti-inflammatory, antioxidant herbs, and nutritional supplements," *Oxidative Medicine and Cellular Longevity*, vol. 2022, Article ID 3599246, 29 pages, 2022.

[57] D. Chen, D. Li, X. Xu, R. Yang, and S. K. Ng, "Electrocardiogram classification and visual diagnosis of atrial fibrillation with DenseECG," 2021, https://arxiv.org/abs/2101.07535.

[58] J. Huang, B. Chen, B. Yao, and W. He, "ECG arrhythmia classification using STFT-based spectrogram and convolutional neural network," *IEEE Access*, vol. 7, pp. 92871–92880, 2019.

[59] M. Degirmenci, M. A. Ozdemir, E. Izci, and A. Akan, "Arrhythmic Heartbeat Classification Using 2D Convolutional Neural Networks," *Irbm*, 2021, https://www.sciencedirect.com/science/article/pii/S1959031821000488.

[60] Y. Zhang, J. Li, S. Wei, F. Zhou, and D. Li, "Heartbeats classification using hybrid time-frequency analysis and transfer learning based on ResNet," *IEEE Journal of Biomedical and Health Informatics*, vol. 25, no. 11, pp. 4175–4184, 2021.

[61] S. L. Oh, E. Y. Ng, R. S. Tan, and U. R. Acharya, "Automated diagnosis of arrhythmia using combination of CNN and LSTM techniques with variable length heart beats," *Computers in Biology and Medicine*, vol. 102, pp. 278–287, 2018.

[62] J. Gao, H. Zhang, P. Lu, and Z. Wang, "An effective LSTM recurrent network to detect arrhythmia on imbalanced ECG dataset," *Journal of Healthcare Engineering*, vol. 2019, Article ID 6320651, 10 pages, 2019.

[63] S. M. P. Dinakarrao, A. Jantsch, and M. Shafique, "Computer-aided arrhythmia diagnosis with bio-signal processing: a survey of trends and techniques," *ACM Computing Surveys*, vol. 52, no. 2, pp. 1–37, 2020.

[64] R. S. Andersen, A. Peimankar, and S. Puthusserypady, "A deep learning approach for real-time detection of atrial fibrillation," *Expert Systems with Applications*, vol. 115, pp. 465–473, 2019.

Hindawi
Computational Intelligence and Neuroscience
Volume 2022, Article ID 9957514, 11 pages
https://doi.org/10.1155/2022/9957514

Research Article

Comparison of Predator-Prey Model and Hawk-Dove Game for Modelling Leukemia

Mariam Sultana,[1] **Fareeha Sami Khan**,[1] **M. Khalid**,[1] **Areej A. Al-moneef**,[2] **Ali Hasan Ali**,[3,4] **and Omar Bazighifan**[5]

[1]*Department of Mathematical Sciences, Federal Urdu University of Arts, Science & Technology, University Road, Gulshan-e-Iqbal Campus, Karachi-75300, Pakistan*
[2]*Department of Mathematical Sciences, College of Science, Princess Nourah Bint Abdulrahman University, P.O. Box 84428, Riyadh 11671, Saudi Arabia*
[3]*Department of Mathematics, College of Education for Pure Sciences, University of Basrah, Basrah, Iraq*
[4]*Doctoral School of Mathematical and Computational Sciences, University of Debrecen, H-4002 Debrecen, Pf. 400, Hungary*
[5]*Department of Mathematics, Faculty of Education, Seiyun University, Hadhramout 50512, Yemen*

Correspondence should be addressed to Omar Bazighifan; o.bazighifan@gmail.com

Received 7 June 2022; Revised 24 August 2022; Accepted 30 August 2022; Published 22 September 2022

Academic Editor: Faisal Saeed

Game theory is an excellent mathematical tool to describe the interaction between the immune system and cancerous leukocytes (*c.leu*). The feature of cancerous leukocytes to differentiate and mutate to give rise to leukemia is in the domain of ecological models as well. In this work, the dynamic of leukemia is described and compared by two models: firstly by a simple probabilistic mathematical model using the zero-sum two player game of Hawk and Dove, and secondly by Leslie Predator Prey model of ecology. The main goal of this study is to compare the results of both models and then discuss the treatment of leukemia i.e., Hematopoietic Stem cell transplant with the best model among them. Hawk and Dove model also describes the cell to cell interaction of cancerous leukocytes and healthy leukocytes (*leu*) after diagnoses and the condition of the patient before and after treatments. In this work, Hematopoietic Stem cell transplant is discussed by using concepts of a zero-sum three player game. Also, both models will be characterized by determining the stability properties, identifying basins of attraction, and locating the equilibrium points to see, at what extent the patient's survival is possible with leukemia in its body. Results for both models will be presented graphically.

1. Introduction

In blood there are several types of diseases that can occur, among them is "hematological malignancy." This term refers to the type of malignancy that can affect lymph nodes, bone marrow, and blood as well. Among hematological malignancy, leukemia was discovered in 1847 by Rudolf Virchow. In Leukemia, the production of a certain kind of white blood cells known as "the blasts" increases, and the normal function of blood and bone marrow gets disturbed. Leukemia is mainly categorized into four types: Acute lymphocytic leukemia (ALL), Chronic lymphocytic leukemia (CLL), Acute myelogenous leukemia (AML), and Chronic myelogenous leukemia (CML). Leukemia, up to some extent, is regarded as the treatable disease in the medical world. For this cause, medical and all other branches of science and technology have been continuously trying to find the cure and efficient drugs to tackle this disease in order to relieve the curb and misery of mankind. To examine the root causes and their therapies, there are plenty of approaches. With the available scientifically obtained data from computer aided models, the mathematical and statistical approach has paved the way for new useful medical investigations. Research on Leukemia is underway. Furth & Makhn [1] showed in

history, the transmission of leukemia in mice, for the very first time. Later on, many mathematical models and treatments were suggested based on intercellular interactions by [2–4]. A further detailed model demonstrated the interactions of myeloblasts with neutrophils, T-cells and leukemia and also provided the treatment model for acute myeloblastic leukemia chemotherapy, see [5]. The model was proposed by Helen & Natasha [6] based on the usual differential equations explaining the interaction of effector T-cell, a naive T-cell in chronic myelogenous leukemia. Huge changes in the growth and death rates of chronic myelogenous leukemia cells can be observed in the results.

Recently, some authors investigated that the patients prognosis of acute myeloid leukemia is due to cytokine-independent leukemic cell proliferation see [7]. Miguel [8] & Rodriguesa et.al [9], also contributed their results for cancer metabolism and presented a detailed mathematical model for chemoimmunotherapy for lymphocytic leukemia describing its normal conditions and stability analysis of immunotherapy. Leukemia and tumor based on several other mathematical models were studied by a few more researchers such as [10–13]. On the other hand, many other models related to differential equations were studied recently by several authors, see [14–26].

It is important to mention here, that all discussed models were furnished either with differential equations or numerical methods but the use of Game theory for a such complex disease is a recent advancement. Game theory is very effective in describing the interaction between the immune system and cancer leukocytes. Whereas the interrelation of stem cell after the transplant with leukocytes against cancerous leukocytes or with cancerous leukocytes against leukocytes is in the domain of evolutionary game theory.

In this century, a new arising treatment of leukemia i.e., stem-cell transplantation has gained the interest of researchers of different fields. By the hematopoietic stem-cell idea, Pappenheim [27] initiated stem-cell biology. Since they are capable of differentiating into the main three major life cells, but also replicating into another cell of their own kind, until the end of life, the process of differentiation of the same DNA continues. This treatment was first performed by Main & Prehn [28] in the mice. Stem-cells have a history that is very fascinating. The researchers observed after the discovery of stem-cells that leukemia tumours have the ability to develop in vitro and vivo colonies, see [29]. This finding and other postulates led to the result that, just as other normal cells differentiate, stem-cells have the capacity to indefinitely differentiate themselves. Cancer stem-cells were first investigated by Lapidot et.al [30] in acute myeloid leukemia and Cobaleda et.al [31] for acute lymphocytic leukemia. These studies captured the interest of mathematicians so many mathematical models have been developed for the treatment of different diseases. Boni et.al [32] suggested a model using evolutionary game theory for the interaction of stem-cells in bioactive scaffolds (i.e., cardiac muscles that lose elasticity). Mneimneh et. al [33] described a game-theoretic and stochastic survivability mechanism against induced attacks in cognitive radio networks. Torkaman et. al [34, 35] developed a system for classifying leukemia based on a cooperative game based on the population of Iran.

With all the available treatments yet, a leukemia patient can not be treated completely but his survival is possible with long term treatments such as chemotherapy, immunotherapy, radiation, and stem cell transplantation. But in all these treatments the major drawback is that these medicines while targeting the *c.leu*destroy the immune system of the patient too. It is yet a challenge to find a such cure that can only target the cancerous cells and improve the life quality of such patients by lessening their pain and suffering. Therefore, this paper is very important in understanding the cell-cell interaction for medical science to gain capabilities of improving the diagnostic techniques and improve survival rate and quality of medicines.

This paper combines the evolutionary game theory and ecology, predator-prey model with life threatening disease i.e., leukemia. The main goal of this study is to apply replicator dynamics and the Leslie predator-prey model to the dynamics of leukemia see Figure 1. Then, treatment of leukemia i.e., stem cell transplant is discussed with the concept of evolutionary game theory because it is easier to formulate the cell to cell interaction by this methodology instead of the Leslie Predator Prey model see Figure 2.

In this paper, significant contributions have been made in both directions: (1) in terms of the formal analysis of this disease, this work has focused on the proposed extension model of an existing formalism. The viability and effectiveness of this proposal are corroborated by the application of both formalism to the analysis. (2) With regard to the design of leukemia dynamics, this approach is based on applying population dynamics, and to generate a mathematical model which can be proven rationally within an underlying game theoretical framework.In this paper, Section 2 is about showing leukemia in a fast time scale using the replicator dynamics model. Section 3 describes the leukemia Dynamics by the Predator Prey model. Section 4 is about a patient's condition after stem-cell transplant therapy in view of replicator dynamics. Section 5 discusses the results of replicator dynamics for Hematopoietic Stem-Cell Transplantation. Also, discusses the numerical values of parameters (i.e cell count of each cell type) among calculations to show the graphical illustrations. Section 6 is the discussion of the results. In Section 7, Conclusion and Future Work is given.

2. Leukemia Dynamics by Hawk and Dove Game

The principles of game theory provide a common framework for creating structures and, eventually, comprehending several significant cancer problems. A game can be defined as a set of comparisons and the opportunity to play the game in line with the game's rules. The classical game theory is founded on a set of strictly defined axioms about game structures. It is assumed in game theory that each player or agent has predefined goals, choices, and interests, which are described by a function called the "utility function." Again, utility refers to the most gains that players may receive as an

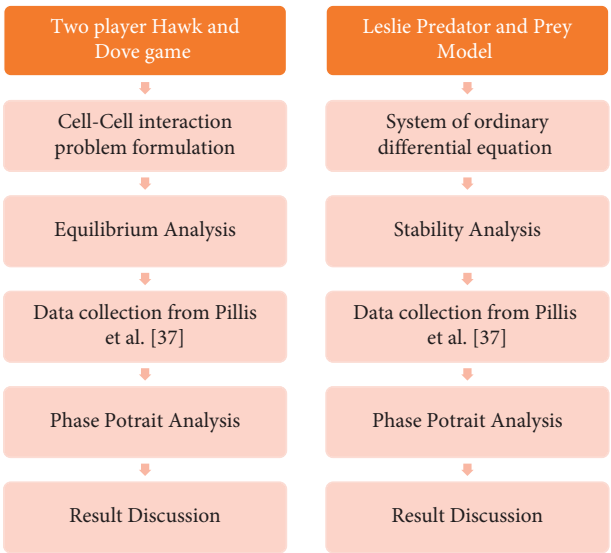

Figure 1: Flow chart of the methodology for mathematical modeling of leukemia.

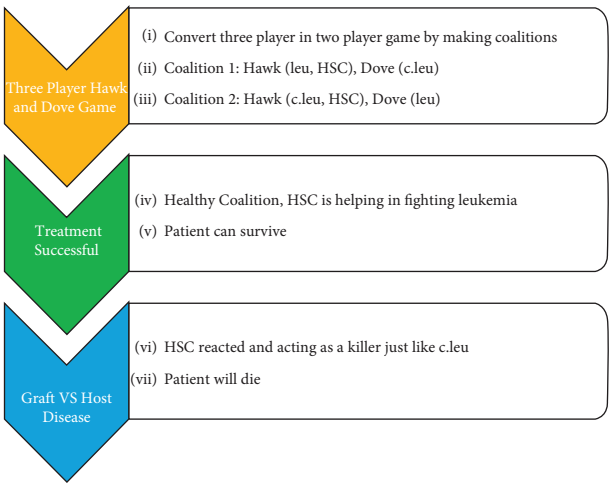

Figure 2: Flow chart of methodology for mathematical modeling of treatment of leukemia.

outcome of the game, and each player's goal, theoretically, is to yield maximum profit or value, theoretically.

(i) Their ethical and viable plan of action in view of the rules.

(ii) The outcome, that players are getting, represent every move they could possibly make given the vast array of strategies at their disposal.

Since acute or chronic leukemia are just different time scale cases theoretically, a case of acute leukemia is taken in consideration in this research (see [36]). Leukocytes, or white blood cells, are a part of the immune system that protect the body from diseases or external invaders (see Figure 3).

While in leukemia, some of these healthy leukocytes get defected and works against the host body and do not let the healthy cells work either. That is the point when tumours are

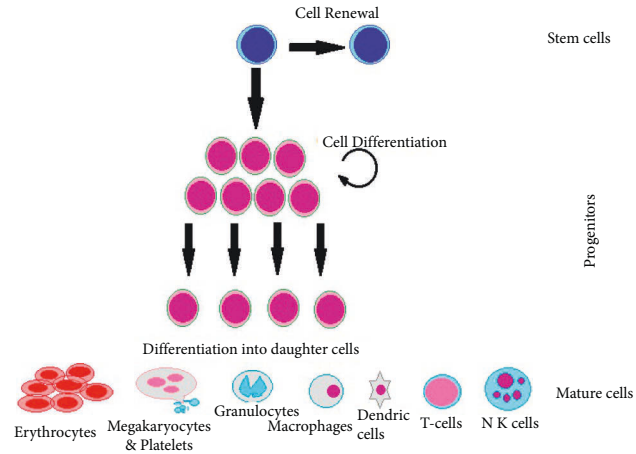

Figure 3: Stem-cell proliferation showing the ability of self renewal and replication into mature cells. This is an infinite process and stem-cells are the only ones who can replicate themselves many times unlike other cells. Unusual proliferation or accelerated cell division can cause leukemia or tumours.

formed called neoplasm. Two types of replicating cells are investigated in this work i.e., cancerous leukocytes (c.leu) and normal leukocytes cells (leu). There will be lower but equal probabilities for *leu* to further multiply into large numbers, resulting in the ability to work as *leu*. In the process, the capacity to sustain neoplastic growth is acquired mainly by those cells which enjoy the capacity for self-renewal. This model concludes that only a limited and restricted number of cells inside the tumour are expected to relaunch tumour development. As per the stochastic theory, the tumour cells are relatively homogeneous, all of these tumour cells undergo active genetic modifications and progress towards malignancy growth. The replicator model suggests that the biologically and functionally explicit population of tumour-launching cells is limited. Therefore the focus of research is on those *leu* breeds that support the progression of targeted treatment for leukemia and this will strongly prevent disease recurrence. Simple and incomplex hypotheses have been made, for the initial discussion of the replicator dynamics model in terms of leukemia. But for more detailed analysis, more and more complex variables that can simulate the reality will be used in the future model.A set of pay off matrix in the evolutionary game theory, i.e., sums, costs, and benefits, of a specific strategy are calculated in terms of success and failure of *leu* and *c.leu*. To begin with the test, let the specific (*c.leu*, *leu*) phenotypes be set as external stimuli, in the general context of the payoff matrix.

$$A = \begin{bmatrix} a_{11} & a_{12} \\ a_{21} & a_{22} \end{bmatrix}. \quad (1)$$

Here, a_{ij} is the player's payoff using the i plan as opposed to the j plan player, since the matrix occupancy acquired in the form as seen in Table 1 is applied in this case, assuming that the interaction between the same type of cells stays neutral, which is why only diagonals are zeros. On the other hand, the *leu*-*c.leu* interplay capitulates into a negative payoff.

Table 1: General form of the payoff matrix for cell to cell interaction.

	$c.l\,(c.leu)$	$I\,(leu)$
$c.l\,(c.leu)$	0	$a_{11} - a_{21} = -a$
$I\,(leu)$	$a_{22} - a_{12} = b$	0

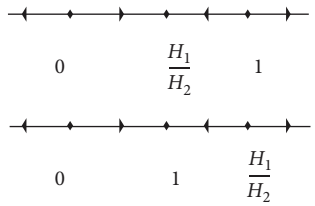

Figure 4: For $n = 2$, the replicator dynamic phase plane showing the three equilibrium points as 0, 1 and a dimorphic equilibrium x^*.

In particular, for evolutionary game theory, this scenario exactly resembles the Hawk and Dove game, where *leu* denotes the Doves and *c.leu* denotes the Hawks. Let the total number of cells be denoted by p in time t and this further can be classified into two types *c.leu* are $P_L(t)$ and *leu* are $P_I(t)$. The cell masses selecting S_i strategy i.e., $S_i = \{s_1, s_2, \ldots, s_k\}$ where $i = 1, 2$ at t. Let $x_1'(t)$ and $x_2'(t)$ denote the cells proportion of Hawk and Dove strategies, respectively.

$$\begin{aligned} x_1'(t) &= \frac{P_L(t)}{p(t)}, \\ x_2'(t) &= \frac{P_I(t)}{p(t)} \\ &= 1 - x_1'(t). \end{aligned} \tag{2}$$

The normalized symmetric matrix in Table 1 gives the general replicator dynamics equation as follows:

$$\begin{aligned} x_1'(t) &= (ax_1 - bx_2)x_1x_2, \\ x_2'(t) &= (bx_2 - ax_1)x_1x_2. \end{aligned} \tag{3}$$

Fitness is referred as the payoff in replicator dynamics. H_i is the fitness of the i phenotype, represented in terms of the A fitness and payoff matrix phenotypes, where the cell population's fitness function is $H_i = (Ax)i$ and $\overline{H}$ is the average fitness of the population of cells i.e., $\overline{H} = \sum_i x_i H_i = x^T Ax$. Taking $x1 + x2 = 1$ and with some algebra, the growth rate of *c.leu* and *leu* by selecting a strategy is *Si*: $x(1-x)(H1 - H2)$ at any time t, here x is the frequency of cells. There are the three stationary points i.e., $0, 1$, and d frac $H1H2 = x*$. For $H_1 < H_2$ it can be stated that x^* is dimorphic. Also, for $(1 - (H_1/H_2))leu$ and $(H_1/H_2)c.leu$, population cells is the polymorphic and stationary point is asymptotically stable. If $H_1 > H_2$, which means $x^* = 1$ then the stationary point is asymptotically stable, which means there are only *c.leu*.

In Figure 4 the unique symmetric mixed Nash equilibrium is asymptotically stable i.e., (H_1/H_2). Also, both pure Nash equilibrium of *leu* and *c.leu* are asymptotically stable. The risk-dominant one has the larger basin of attraction which is true in general because $x^* > (1/2)$ for games with an efficient equilibrium and a risk dominant one.

In this paper, the dynamical behaviour of the cells in mathematical models, is illustrated with the help of Mathematical software. These portraits are within the standard ranges of *leu* and *c.leu* blood samples of patients recently diagnosed with leukemia, see [37]. In leukemia, *leu* counts differ rarely or sometimes at regular intervals ranging from 30 to 200×10^9 cells/liter. This variance was recorded during the 40 to 80 days time frame, which is a significantly long time relative to the *c.leu* life span and maturation acquisition.

In these portraits, the white zigzag trajectory shows *c.leu* and pink dotted line shows *leu*. In Figure 5 *c.leu* is greater in number than *leu* and if not treated soon *c.leu* will make *leu* extinct and the patient will die with the passage of time. Also, the trajectory shows an unstable node as the direction is moving away from the point. *c.leu* is much larger in amount than *leu* in Figure 6 and with the passing time, *c.leu* makes *leu* extinct and the patient dies. As the path shifts away from the point, the trajectory also shows unstable nodes. So this is the point where the cell population is monomorphic, which is that there will be just *c.leu*. It is studied by using fast-scale techniques that if not treated, how quickly a patient will die of acute leukemia.

3. Leukemia Dynamics by Leslie Predator Prey Model

The Leslie Predator-Prey Model has a significant impact on the field of mathematical biology and ecology. If the cancerous leukocytes (predator) density is $l(t)$ and the leukocytes (prey) density is $i(t)$, then Leslie's model can be represented by systems of nonlinear differential equations as follows:

$$\frac{\mathrm{d}i}{\mathrm{d}t} = (r_1 - c_1 l - bi)i, \tag{4}$$

$$\frac{\mathrm{d}l}{\mathrm{d}t} = \left(r_2 - c_2\frac{l}{i}\right)l. \tag{5}$$

In equation (5), the factor $c2\,(l/i)$ is defined as Gower Term. The reason for adding the Gower word comes from the leukocyte growth rate factor, as countless $(i \longrightarrow \infty)$ rise relative to the per capita growth of the cancerous leukocytes reaches their maximum growth i.e., $((1/l)(\mathrm{d}l/\mathrm{d}t) \longrightarrow r_2)$. On the other hand, when leukocyte population declines i.e., $(i \longrightarrow 0)$, then $(1/l)(\mathrm{d}l/\mathrm{d}t) \longrightarrow -\infty$ (i.e., cancerous leukocytes must vanish). Both cells have logistic growth. r_1 is the growth rate of *leu* with carrying capacity (r_1/b_1) and r_2 is the growth rate of *c.leu* with carrying capacity (c_2/i) in proportion to the population size of leukocytes. c_1 and c_2 provides the estimate of the quantity of transformation of *c.leu* and *leu* into each other respectively. The constant b signifies the effectiveness of *c.leu* in eliminating *leu*. In Leslie's model it was suggested that the carrying capacity of a predator should be equal to prey. Also, it should be

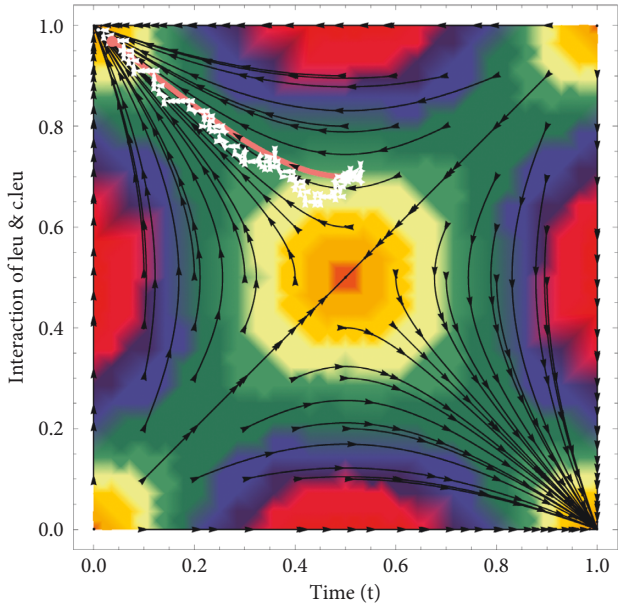

Figure 5: Diagnosis of leukemia is shown through the replicator dynamic phase plane.

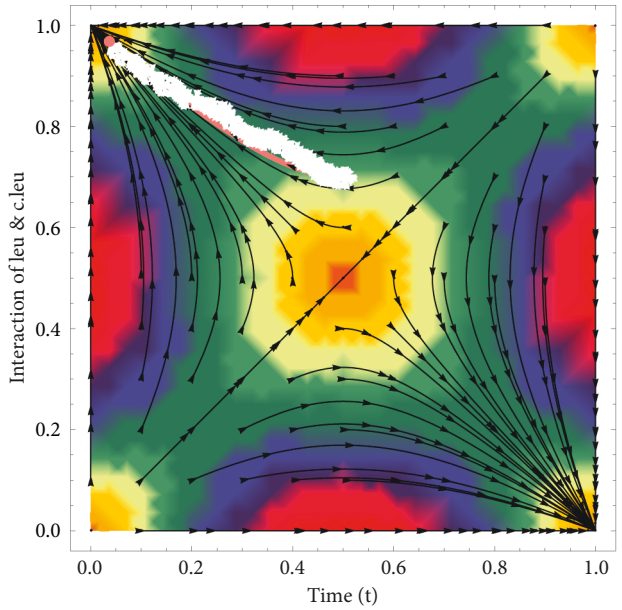

Figure 6: *leu* and *c.leu* phase plane of interaction. At the time of the spread of the disease when the patient is near death.

emphasized that the upper limits associated with predator prey together are met under the following conditions:

(i) For Predators: when there are more predators than prey in the population ratio

(ii) For Prey: when the ratio of Prey to Prey population is high

To estimate the level of success of the design function for achieving the set targets, take into consideration another type of function that acts as a fitness function and intends to represent the net outcome as a single merit value as follows:

$$H_1 = \frac{r_1}{k_1}(k_1 - i) - bl, \tag{6}$$

$$H_2 = r_2\left(1 - \frac{l}{cbi}\right), \tag{7}$$

where H_1 and H_2 are the fitness functions of *leu* and *c.leu*, respectively. For a detailed derivation of equation (6) please see [36]. In contrast with *c.leu*, equation (7) defines the increased death rate of *leu*. c is the nutritional value constant of *leu*, which is proportional to *c.leu*. The densities of *leu* and *c.leu* at t time are i and l. Also, r_1 & r_2 are the intrinsic growth rate of *leu* and *c.leu*, k is the carrying capacity. The assumptions of this model are that a predator is intruding into each other's behavior. This intervention has a negative effect on the predators themselves and increases the mechanism to bring the dramatic shifts in equilibrium, stability, and strength in the population of *c.leu* and *leu*. Consider the difference equation of equations (6) & (7) to be interpreted to understand this phenomenon more closely,

$$\begin{aligned} i(t+1) &= i\left(1 + \frac{r_1}{k_1}(k_1 - i) - bl\right), \\ l(t+1) &= l\left(1 + r_2\left(1 - \frac{l}{cbi}\right)\right). \end{aligned} \tag{8}$$

Solving equation (5) the following equilibrium point is obtained $E = r_1c_2/(bc_2 + c_1r_2)$, $r_1r_2/(bc_2 + c_1r_2)$. The Jacobian matrix of equation (5) at this equilibrium point is given by the following equation:

$$J_{(i,l)} = \begin{bmatrix} \dfrac{-r_1bc_2}{bc_2 + c_1r_2} & \dfrac{-r_1c_1c_2}{bc_2 + c_1r_2} \\ \dfrac{r_2^2}{c_2} & -r_2 \end{bmatrix}. \tag{9}$$

Therefore the characteristic equation is

$$\lambda^2 + \frac{r_1bc_2 + (bc_2 + c_1r_2)r_2\lambda}{bc_2 + c_1r_2} + \frac{r_1br_2c_2 + r_1c_1r_2^2}{bc_2 + c_1r_2} = 0. \tag{10}$$

Obviously, $\lambda_1\lambda_2 = (r_1br_2c_2 + r_1c_1r_2^2/bc_2 + c_1r_2) > 0$ and $\lambda_1 + \lambda_2 = -(-r_1bc_2 + (bc_2 + c_1r_2)/bc_2 + c_1r_2) < 0$. Hence equilibrium $E = (r_1c_2/(bc_2 + c_1r_2))$, $(r_1r_2/(bc_2 + c_1r_2))$ is an asymptotically stable node if $(\sqrt{r_1} - \sqrt{r_2})^2 \geq (r_1c_1r_2/bc_2 + c_1r_2)$ or focus if $(\sqrt{r_1} - \sqrt{r_2})^2 < (r_1c_1r_2/(bc_2 + c_1r_2))$. Also, the positive equilibrium (x^*, y^*) of system equation (5) is globally stable, where $x^* = (r_1c_2/(bc_2 + c_1r_2))$ & $y^* = (r_1r_2/(bc_2 + c_1r_2))$.

Parameters, i.e., modest intraspecific competition, are shown on the left side of Figure 7. Leukemia was the patient's original diagnosis. As can be seen in the graph on the left, *leu* and *c.leu* coexist in the body. The stable node is thus present during this time interval.

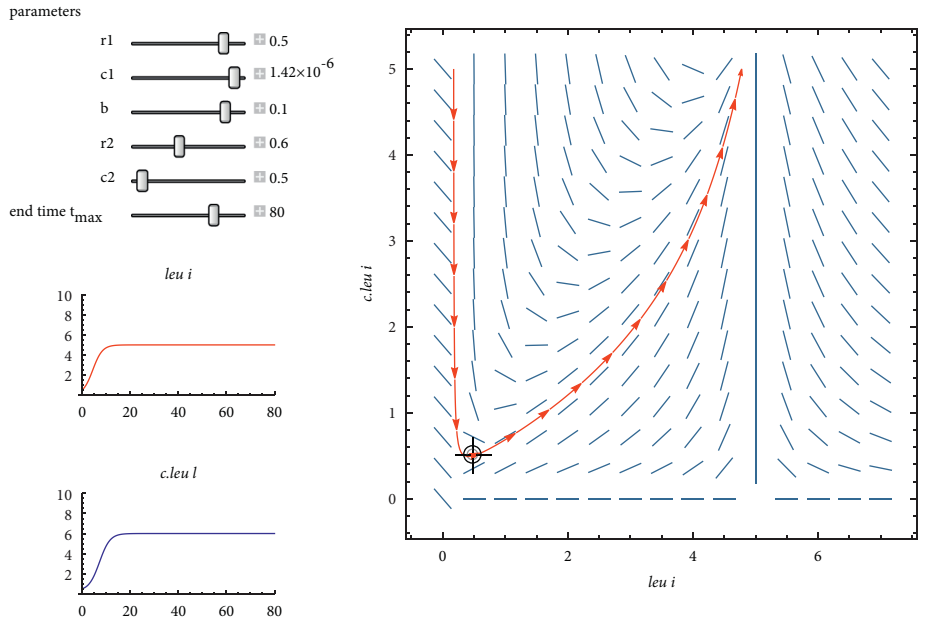

Figure 7: A phase plane of a two-dimensional Leslie predator-prey model that demonstrates the cohabitation of *leu* & *c.leu*.

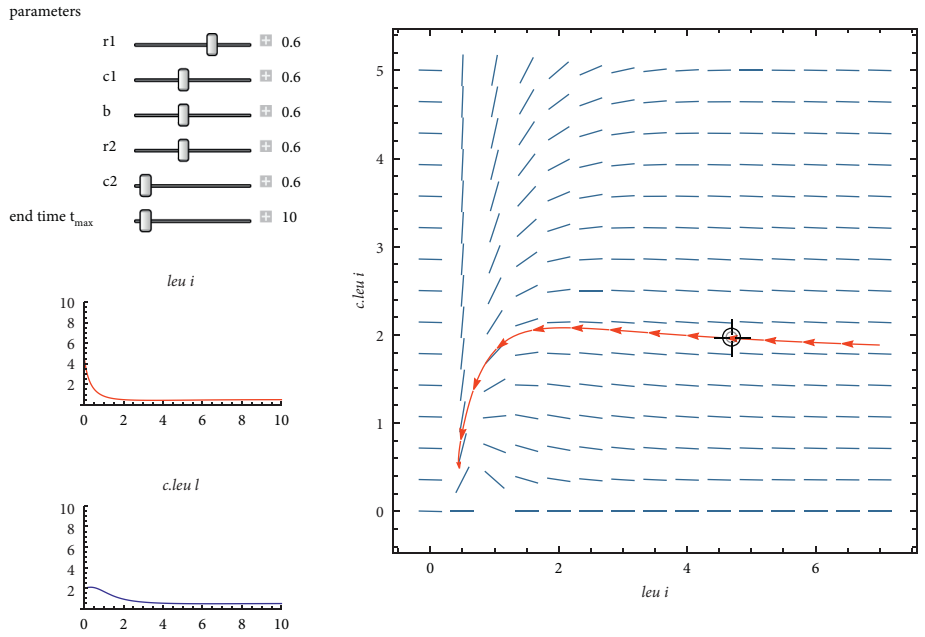

Figure 8: Phase plane for a two-dimensional Leslie predator-prey model.

An interspecific competition with high saddles. The parameters are displayed on the left. As an example, acute leukemia *leu*has a typical range of 0 to 6; however, when acute leukemia flares up, the graph shows that *c.leu*climbs to 6 or higher and *leu*becomes scarce. This node is unstable.

Figure 8 illustrates how chronic leukemia, or *leu* and *c.leu*, can coexist in a patient's body for a very long time. The parameters are displayed on the left. While there is an equilibrium point between $x = 0$ to 2 and $y = 0$ to 4, it is a globally unstable node because the trajectory is moving away gradually. As mentioned above, there are three symptoms that a person with leukemia could encounter. They are all globally stable nodes since all of the estimated critical points are positive.

Typically, a blood sample is taken when a patient has no symptoms yet the disease is present in his blood. Similar to the previous portraits, they are unstable nodes since both healthy and cancerous leukocytes are present in the blood, and in this model, the equilibrium stable point or node occurs when one cell population prevails or survives with a high rate. By utilizing a few algebraic procedures and the mathematical software Mathematica, two different scale

models of various areas have been developed and studied. Although different results were found, the scenario remained the same. So let's talk about leukemia treatment in the section afterwards.

4. Hematopoietic Stem-Cell Transplantation (HSC)

In this section, a speculative patient who has already been given high chemotherapy measurements and has been transplanted with *HSC*. Since this is a mathematical study and a hypothetical patient is considered here (assumed parameter values are closer to the real patients data described in Section 5.1) so it is important to clarify here that the sole purpose of this study is to show the applicability of a powerful model such as "replicator dynamics" on a complex disease such as "leukemia." Hence the complications occurring due to chemotherapy and its medicine have not been included in this study. Only the after effects of chemotherapy on blood count is considered in this work.

To understand the interaction of *HSC*, *leu*, and *c.leu* after the transplant, game theory have been used. Here are three players, namely, *HSC*, *c.leu*, and *leu*, with two execution strategies: kill or not kill. In such a case, there are two cell reaction possibilities when *HSC* enters the body of the patient. One is that, with them, *leu* will react and produce graft versus host disease that is not favourable for the patient and therefore can be said to be grouped with *c.leu*. And secondly, to boost the patient's immune system, *HSC* creates a group of *leu* to help destroy the remaining *c.leu* to support him in recover.

There is one and only one coalition that could conceivably occur in two-individual games, particularly the coalition between the two players. The amount of possibilities is, obviously greater in games with more than two players, called n–individual games. As with this case, the following segments of the players in coalitions could occur in a game with three players:

(a) For any player on his own

(b) A coalition between Player 3 and Players 1 & 2

(c) Players 1 & 3 versus 2

(d) Players 2 & 3 versus 1

(e) the grand alliance, all three players included, see [36]

So on the basis of the *HSC* decision, this case has two clear coalitions to decide if it applies to *leu* to fight against the remaining *c.leu* or to collate with *c.leu* against *leu* i.e.,

(i) Favourable (HSC, leu) unfavourable $(c.leu)$

(ii) Favourable (leu) unfavourable $(c.leu, HSC)$

It is presumed that interactions between cells of the same types are neutral, therefore, there are zeros on the diagonal, see Tables 2 and 3*). In the presence of the right stimuli that allow the cell to differentiate, while interacting with an unfavourable team,* the favourable team receives a positive payoff, while the unfavourable team receives a negative payoff. This implies not only that it is believed that the favourable team gets a greater payoff under the favourable environment, but also that an unfavourable team will get negative feedback under this environment, see Tables 2 and 3. In Tables 2 and 3 normalized matrices, F_1 stands for a favourable team and F_2 for an unfavourable team.

Table 2: General form of the payoff matrix for cell/cell interaction in *HSC* transplant (coalition (i)).

	F_1	F_2
F_1	0	$a - c = -a_1$
F_2	$d - b = a_2$	0

Table 3: General form of the payoff matrix for cell/cell interaction in *HSC* transplant (coalition (ii)).

	F_1	F_2
F_1	0	$e - g = -b_1$
F_2	$h - f = b_2$	0

5. Replicator Dynamics and Nash Equilibrium of *HSC* Transplantation

If there are n distinct behaviour patterns called "Pure Strategies," $E_1, E_2, \ldots, E_n$ where $n = 1, 2$. The state of a population of cells concerning this conflict is fully described by a vector $x_i = [x_1, x_2, \ldots, x_n] \in R^n$, where x_i represents the frequency of *leu* and *c.leu* with behaviour $E_i, i = 1, 2, \ldots, n$. Consequently, $x_i \geq 0$ for all i and $\sum_i x_i = 1$ the set of all such $x's$ is denoted by S^n. If an E_i individual cell contends with an E_j individual cell then the payoff will be a_{ij}. Let A be the matrix of all those a_{ij}'s. Then, assuming random encounters of cells as,

$$e_i.Ax = \sum_i a_{ij} x_j, \tag{11}$$

is the average payoff for an E_i-cell in a cell population x and

$$\begin{aligned} x.Ax &= \sum_i x_i e_i.Ax \\ &= \sum_i \sum_j a_{ij} x_i x_j, \end{aligned} \tag{12}$$

is the mean average payoff within cell population x. Taylor and Jonker [38] assumed that the growth rates $(\dot{x}_1 / x_i) = ((dx_i/dt)/x_i)$ of the frequency of strategy E_i are equal to the payoff difference $e_i.Ax - x.Ax$, This yields the replicator equation

$$\dot{x}_1 = x_i [e_i.Ax - x.Ax]; \quad i = 1, 2, \ldots, n, \tag{13}$$

on the invariant set S^n. If the game begins with $x_i(t_\circ) = 0$, so for all t, the strategy is $x_i(t) = 0$. And if there are no favourable cells or unfavourable cells that play strategy from the beginning, then there are no cells that can replicate that approach. The general replicator dynamics equation for normalized symmetric matrix from Tables 2 and 3 is

$$x_1' = (a_1x_1 - a_2x_2)x_1x_2,$$
$$x_2' = (a_2x_2 - a_1x_1)x_1x_2. \quad (14)$$

After some algebra, these equations become

$$x_1' = x_1(1 - x_1)(a_1 - (a_1 + a_2)x_2). \quad (15)$$

Also,

$$x_1' = (b_1x_1 - b_2x_2)x_1x_2,$$
$$x_2' = (b_2x_2 - b_1x_1)x_1x_2. \quad (16)$$

After some algebra these equations become

$$x_2' = x_2(1 - x_2)(b_1 - (b_1 + b_2)x_1). \quad (17)$$

Which gives five solutions for equations (15) and (17) i.e., the pure strategy unstable solutions are $(0,0)$, $(1,1)$, $(1,0)$, $(0,1)$ or a mixed strategy solution $((a_1/a_1 + a_2), (b_1/b_1 + b_2))$. Clearly, system has positive equilibrium hence the Jacobian matrix at equilibrium is given by the following equation:

$$J^* = \begin{bmatrix} (1 - 2x_1^*) \times (a_1 - (a_1 + a_2)x_2^*) & -x_1^*(1 - x_1^*)(a_1 + a_2) \\ -x_2^*(1 - x_2^*)(b_1 + b_2) & (1 - 2x_2^*) - (b_1 - (b_1 + b_2)x_1^*) \end{bmatrix}. \quad (18)$$

For easier calculation let $a_1 = a, b_1 = b$, $(a_1 + a_2) = m$, $(b_1 + b_2) = n$ then a mixed strategy equilibrium occurs when $0 < (a/m), (b/n) < 1$ where $x_1^* = (b/n), x_2^* = (a/m)$. From this, it can be deduced that this system has a positive equilibrium. Therefore, its Jacobian matrix at this equilibrium point becomes

$$J^* = \begin{bmatrix} 0 & \frac{-bm}{n}\left(1 - \frac{b}{n}\right) \\ \frac{-an}{m}\left(1 - \frac{a}{m}\right) & 0 \end{bmatrix}. \quad (19)$$

Now, further this matrix describes two cases:

(i) if a_1 & b_1 have different sign, then after solving equations (15) & (17), it is observed that the function shows closed spirals and is monotonic if the following conditions are satisfied:

(a) $a_1 \leq (a_1 + a_2)$ & $b_1 > (b_1 + b_2)$
(b) $a_1 > (a_1 + a_2)$

(ii) if a_1 and b_1 have same sign than it is a saddle point which means an unstable point. Also, its equilibrium is hyperbolic i.e., (x_1^*, x_2^*), so from this, it can be observed that one monomorphic fixed point is asymptotically stable whereas the fixed points under replicator dynamics is a saddle.

5.1. Complete Description of Leukocytes (NK Cells, Peripheral CD34+cells):. The number of *Nk* cells after chemotherapy is given in parameters see [37] where 2.08×10^{-7} *Nk* cells and 5.00×10^{8} *leu* are remaining cells in the body. The mean value of the peripheral *CD*34+ cells infused was 9.19×10^{6} cells/*kg* recipient's body weight and the mean *CD*34+ cell number was 3.47×10^{4} cells/*kg*. Whereas Pillis et.al [37] shows remaining *c.leu* i.e., 4.31×10^{-1} and 1.42×10^{-6} cells/*kg*.

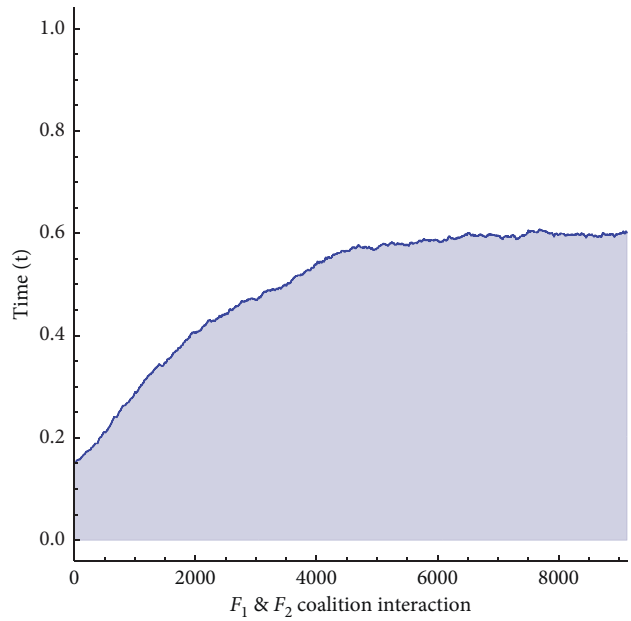

Figure 9: Phase portrait of replicator dynamics after stem-cell transplantation for (*leu*) and (*HSC*, *c.leu*).

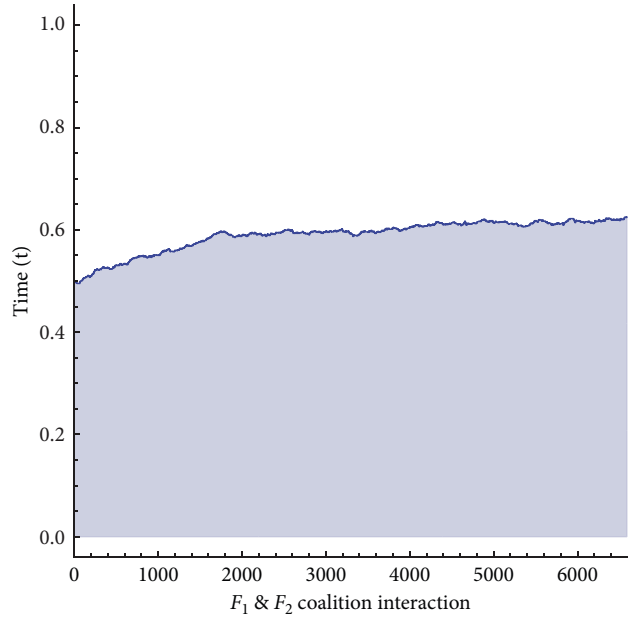

Figure 10: Phase portrait of replicator dynamics after stem-cell transplantation for favourable (*HSC*, *leu*) and unfavourable (*c.leu*).

Figure 9 shows how badly this coalition can affect the patient's life as at the time of chemotherapy the number of

Table 4: Description of parameters for leukemia patient for different stages of disease.

Description	Early prognosis value	Acute leukemia	Chronic leukemia
r_1	0.5	0.7	0.6
c_1	1.42×10^{-6}	0.7	0.6
b	0.1	0.25	0.6
r_2	0.6	0.75	0.6
c_2	0.5	0.4	0.6

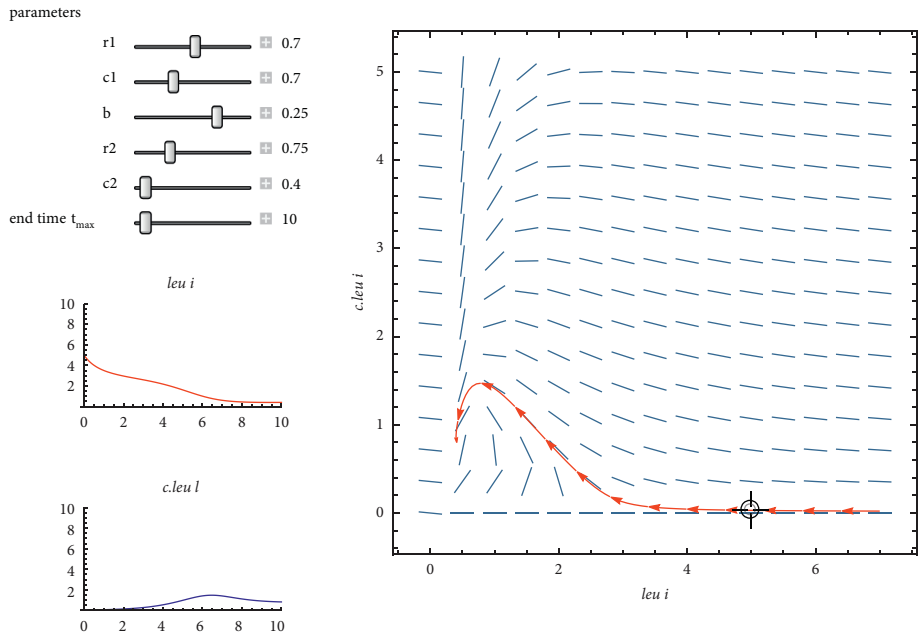

Figure 11: Leslie's predator-prey phase plane depicts the onset of the disease or the decrease in leukocytes following an increase in cancerous leukocytes.

c.leu was minor but after transplantation if graft versus host disease occurs, it can kill the patient. The rise can be observed in an unfavourable coalition of cells. The payoff matrix for this simulation becomes

$$J^* = \begin{bmatrix} 0 & 5 \times 10^8 \\ 9.2247 \times 10^6 & 0 \end{bmatrix}. \quad (20)$$

Interaction of favourable and unfavourable coalition of *leu* and *c.leu* with *HSC* is described in Figure 10. As it can be seen after a small oscillation the unfavourable group has stopped rising, whereas *leu* is approaching infinity. Payoff matrix for this simulation becomes

$$J^* = \begin{bmatrix} 0 & 1009224700 \\ 0.431001 & 0 \end{bmatrix}. \quad (21)$$

Equations (20). And (21). Gives real and distinct eigen values as they have opposite signs. Equation (20). Have $\det(J^*) = -4.61235 \times 10^{15} < 0$, $\tau^2 - 4\det(J^*) > 0$ shows a saddle point. Equation (21). Also, have distinct and real eigen values and $\det(J^*) = -434976854.9 < 0$, $\tau^2 - 4\det(J^*) = 83424.39498 > 0$ which means its also a saddle point.

6. Discussion of Results

According to the calculations, it showed that replicator dynamics has three stationary points, 0, 1 and $(H_1/H_2) = x^*$. Also, it showed that x^* is dimorphic for $H_1 \leq H_2$ which means that in blood, both cell populations (i.e., *leu*and c.leu) exist.

For asymptotically stable stationary point, it showed that the cell population is polymorphic i.e., $1 - (H_1/H_2)$*c.leu*and (H_1/H_2) leu.

For monomorphic cell population i.e., only *c.leu*exists, where $x^* = 1$, for $H_1 \geq H_2$ which implies that x^* is asymptotically stable.

By considering the data of a patient who has been diagnosed with leukemia, the two-dimensional Leslie predator prey model of equation (10). Shows in Figure 7 a stable node, that is, $(\sqrt{r_1} - \sqrt{r_2})^2 = 4.5548 \times 10^{-3}$ and $(r_1 c_1 r_2/bc_2 + c_1 r_2) = 8.519876 \times 10^{-6}$.

The coexistence equilibrium point with parameters given in Table 4 is obtained as $x^* = 4.99$ and $y^* = 5.99$. At this point the patient can survive for some time period.

Also, from Figure 11 if $(\sqrt{r_1} - \sqrt{r_2})^2 \geq (r_1 c_1 r_2/bc_2 + c_1 r_2)$ with parameters in Table 4 it gives $(\sqrt{r_1} - \sqrt{r_2})^2 = 8.623253 \times 10^{-4}$, $(r_1 c_1 r_2/bc_2 + c_1 r_2) = 0.588$ then both the

eigenvalues are positive i.e., $\lambda_1 + \lambda_2 = 0.638, \lambda_1\lambda_2 = 0.525$ so it is unstable knot. This situation describes an acute leukemia i.e., variation of parameters shows a drastic change in patients condition.

For a chronic leukemia patient, the parameters are given in Table 4 and the critical point is $x^* = 0.5$ and $y^* = 0.5$. As it can be observed in Figure 8, in this case, the patient condition does not change drastically but still, it is an unstable node due to the positive eigen values i.e., $\lambda_1 + \lambda_2 = 0.3, \lambda_1\lambda_2 = 0.36$

In the last section, a three player game interaction is described after the *HSC* transplantation between human normal *leu*, *c.leu*, and *HSC*. It is shown by taking two coalitions i.e., favourable and unfavourable. Different results have been obtained to show the accuracy and applicability of replicator dynamics to this disease. The phase portrait Figure 10 for the first coalition between favourable and unfavourable cells depicts the rise in *leu*. Which means that chemotherapy is being successful in eliminating the *c.leu*, the transplant have been successful and patient will surely survive.

The portrait in Figure 9 indicates the increase in unfavourable cell coalitions. The second coalition indicates how badly it can affect the life of the patient because the amount of cancerous leukocytes are limited at the time of chemotherapy, but if graft versus host disease happens after transplantation, it can destroy all the remaining leukocytes that cause the patient to die.

7. Conclusion & Future Work

This paper concludes that even a complex disease such as leukemia can be described using population dynamics and evolutionary game theory. These techniques have been implemented and their results provided. These models successfully deduce steady states and their stability. These models individually permit the existence of two types of stationary states:

(1) State of no disease, with no cancerous leukocytes

(2) State of coexistence where a cancerous leukocyte persists against the background of the immune response

The state of no disease is asymptotically stable and a state of leukemia is unstable. Both models are in complete agreement about stable and unstable situations. It was found from the study, that the state of no disease represents the immune state.

In this research, a two person zero-sum game of evolutionary game theory is used to describe the patient's condition having leukemia. Different results have been obtained for this situation by incorporating a mathematical software Mathematica. Then leukemia dynamics is studied by an ecological model Lesli predator prey model. Different results have also been obtained for this situation as well by incorporating a mathematical software Mathematica. The treatment of leukemia i.e., HSC is then studied by using a three player zero sum game as it was observed that evolutionary game theory gives a better understanding of leukemia than the ecological model. This study is a sincere effort to show another perspective of game theory that it can also define the complex dynamics of leukemia. By adding more complex factors, these calculations can give more realistic and accurate results.

The game is based on the number of leukocytes in this paper, but in future work, we may investigate evolutionary game theory for leukemia into specific cell types and their count to better determine which cell types should specifically be targeted and can result in eradicating the disease. Because current treatment advancements remove both healthy and malignant cells from the body, patients suffer greatly and are more susceptible to getting infected by a virus.

Data Availability

No data were used to support this study.

Conflicts of Interest

The authors declare that they have no conflicts of interest.

References

[1] J. Furth and M. C. Makhn, "The transmission of leukemia of mice with a single cell," *American Journal of Cancer*, vol. 31, pp. 276–282, 1937.

[2] E. P. Cronkite and P. C. Vincent, "Granulocytopoiesis," *Series Haematologica*, vol. 2, pp. 3–34, 1969.

[3] S. I. Rubinow, "A simple model of steady state differentiating cell system," *Journal of Cell Biology*, vol. 43, no. 1, pp. 32–39, 1969.

[4] S. I. Rubinow and J. L. Lebowitz, "A mathematical model of neutrophil production and control in normal man," *Journal of Mathematical Biology*, vol. 1, no. 3, pp. 187–225, 1975.

[5] S. I. Rubinow and J. L. Lebowitz, "A mathematical model of the chemotherapeutic treatment of acute myeloblastic leukemia," *Biophysical Journal*, vol. 16, no. 11, pp. 1257–1271, 1976.

[6] H. Moore and N. K. Li, "A mathematical model for chronic myelogenous leukemia (CML) and T cell interaction," *Journal of Theoretical Biology*, vol. 227, no. 4, pp. 513–523, 2004.

[7] S. Thomas, D. H. Anthony, and M. C. Anna, "Mathematical modeling of the impact of cytokine response of acute myeloid leukemia cells on patient prognosis," *Scientific Reports*, vol. 8, pp. 1–11, 2018.

[8] M. Á. Medina, "Mathematical modeling of cancer metabolism," *Critical Reviews in Oncology*, vol. 124, pp. 37–40, 2018.

[9] D. Rodrigues, P. Mancera, T. Carvalho, and L. F. Gonçalves, "A mathematical model for chemoimmunotherapy of chronic lymphocytic leukemia," *Applied Mathematics and Computation*, vol. 349, pp. 118–133, 2019.

[10] S. Chulián, A. Martínez-Rubio, M. Rosa, and V. M. Pérez-García, "Mathematical models of leukaemia and its treatment: a review," *SeMA Journal*, vol. 79, no. 3, pp. 441–486, 2022.

[11] P. T. Hamilton, B. R. Anholt, and B. H. Nelson, "Tumour immunotherapy: lessons from predator-prey theory," *Nature Reviews Immunology*, 2022.

[12] H. F. Kiwumulo, H. Muwonge, C. Ibingira, J. B. Kirabira, and R. T. Ssekitoleko, "A systematic review of modeling and simulation approaches in designing targeted treatment technologies for Leukemia Cancer in low and middle income

countries," *Mathematical Biosciences and Engineering*, vol. 18, no. 6, pp. 8149–8173, 2021.

[13] T. Stiehl, "Using mathematical models to improve risk-scoring in acute myeloid leukemia," *Chaos*, vol. 30, no. 12, Article ID 123150, 2020.

[14] M. I. Salman and B. Wang, "Boosting performance for software defined networks from traffic engineering perspective," *Computer Communications*, vol. 167, pp. 55–62, 2021.

[15] M. I. Salman and B. Wang, "Near-optimal responsive traffic engineering in software defined networks based on deep learning," *Future Generation Computer Systems*, vol. 135, pp. 172–180, 2022.

[16] B. Almarri, A. H. Ali, K. S. Al-Ghafri, A. Almutairi, O. Bazighifan, and J. Awrejcewicz, "Symmetric and non-oscillatory characteristics of the neutral differential equations solutions related to p-laplacian operators," *Symmetry*, vol. 14, no. 3, p. 566, 2022.

[17] B. Almarri, A. H. Ali, A. M. Lopes, and O. Bazighifan, "Nonlinear differential equations with distributed delay: some new oscillatory solutions," *Mathematics*, vol. 10, no. 6, p. 995, 2022.

[18] B. Almarri, S. Janaki, V. Ganesan, A. H. Ali, K. Nonlaopon, and O. Bazighifan, "Novel oscillation theorems and symmetric properties of nonlinear delay differential equations of fourth-order with a middle term," *Symmetry*, vol. 14, no. 3, p. 585, 2022.

[19] O. Bazighifan, A. H. Ali, F. Mofarreh, and Y. N. Raffoul, "Extended approach to the asymptotic behavior and symmetric solutions of advanced differential equations," *Symmetry*, vol. 14, no. 4, p. 686, 2022.

[20] A. H. Ali, G. A. Meften, O. Bazighifan, M. Iqbal, S. Elaskar, and J. Awrejcewicz, "A study of continuous dependence and symmetric properties of double diffusive convection: forchheimer model," *Symmetry*, vol. 14, no. 4, p. 682, 2022.

[21] G. Abed Meften, A. H. Ali, K. S. Al-Ghafri, J. Awrejcewicz, and O. Bazighifan, "Nonlinear stability and linear instability of double-diffusive convection in a rotating with LTNE effects and symmetric properties: brinkmann-forchheimer model," *Symmetry*, vol. 14, no. 3, p. 565, 2022.

[22] B. Qaraad, O. Bazighifan, T. A. Nofal, and A. H. Ali, "Neutral differential equations with distribution deviating arguments: oscillation conditions," *Journal Of Ocean Engineering And Science*, 2022.

[23] S. S. Santra, T. Ghosh, and O. Bazighifan, "Explicit criteria for the oscillation of second-order differential equations with several sub-linear neutral coefficients," *Advances in Difference Equations*, vol. 2020, no. 1, p. 643, 2020.

[24] O. Bazighifan, "An approach for studying asymptotic properties of solutions of neutral differential equations," *Symmetry*, vol. 12, no. 4, p. 555, 2020.

[25] O. Moaaz, D. Chalishajar, and O. Bazighifan, "Some qualitative behavior of solutions of general class of difference equations," *Mathematics*, vol. 7, p. 585, 2019.

[26] M. W. AbdulRidha and H. A. Kashkool, "Space-time petrov-discontinuous galerkin finite element method for solving linear convection-diffusion problems," *Journal of Physics: Conference Series*, vol. 2322, no. 1, Article ID 012007, 2022.

[27] A. Pappenheim, "Prinzipien der neuen morphologischen Haematologie nach zytogenetischer Grundlage," *Folia Haematologica*, vol. 21, pp. 91–101, 2017.

[28] J. M. Main and R. T. Prehn, "Successful skin homografts after the administration of high dosage X radiation and homologous bone marrow," *Journal of the National Cancer Institute*, vol. 15, no. 4, pp. 1023–1029, 1955.

[29] C. Southam and A. Brunschwig, "Quantitative studies of autotransplantation of human cancer," *Cancer*, vol. 14, pp. 461–463, 1961.

[30] T. Lapidot, C. Sirard, J. Vormoor et al., "A cell initiating human acute myeloid leukaemia after transplantation into SCID mice," *Nature*, vol. 367, no. 6464, pp. 645–648, 1994.

[31] C. Cobaleda, N. Gutierrez-Cianca, J. Perez-Losada et al., "A primitive hematopoietic cell is the target for the leukemic transformation in human Philadelphia-positive acute lymphoblastic leukemia," *Blood*, vol. 95, no. 3, pp. 1007–1013, 2000.

[32] A. Boni, C. Stallo, T. Rossi, M. Ruggieri, and P. Di-Nardo, "Application of Evolutionary Game Theory on stem cells interaction in bio-active scaffolds," in *Proceedings of the IEEE 3rd International Symposium on Applied Sciences in Biomedical and Communication Technologies (ISABEL)*, Roma, Italy, Nov 2010.

[33] S. Mneimneh, S. Bhunia, F. Vázquez-Abad, and S. Sengupta, "A game-theoretic and stochastic survivability mechanism against induced attacks in cognitive radio networks," *Pervasive and Mobile Computing*, vol. 40, pp. 577–592, 2017.

[34] A. Torkaman, N. M. Charkari, M. A. Pour, M. Bahrololum, and E. Hajati, "An expert system for detection of leukemia based on cooperative game theory," in *Proceedings of the IEEE 35th Annual Northeast Bioengineering Conference*, Boston, MA, USA, Apr 2009.

[35] A. Torkaman, N. M. Charkari, and M. Aghaeipour, "An approach for leukemia classification based on cooperative game theory," *Analytical Cellular Pathology*, vol. 34, no. 5, pp. 235–246, 2011.

[36] S. K. Fareeha, "Mathematical Modeling of Stem-Cell Transplantation Using Evolutionary Game Theory," M. P.. Thesis, Federal Urdu University of Arts, Science & Technology, Romania, Pakistan, 2014.

[37] L. G. de Pillis, W. Gu, and A. E. Radunskaya, "Mixed immunotherapy and chemotherapy of tumors: modeling, applications and biological interpretations," *Journal of Theoretical Biology*, vol. 238, no. 4, pp. 841–862, 2006.

[38] P. D. Taylor and L. B. Jonker, "Evolutionary stable strategies and game dynamics," *Mathematical Biosciences*, vol. 40, no. 1-2, pp. 145–156, 1978.

Hindawi
Computational Intelligence and Neuroscience
Volume 2022, Article ID 9879259, 14 pages
https://doi.org/10.1155/2022/9879259

Research Article

Remote Monitoring of COVID-19 Patients Using Multisensor Body Area Network Innovative System

Israa Al-Barazanchi,[1,2] **Wahidah Hashim**,[1] **Ammar Ahmed Alkahtani**,[3] **Haider Rasheed Abdulshaheed**,[2,4] **Hassan Muwafaq Gheni**,[5] **Aparna Murthy**,[6] **Elika daghighi**,[7] **Shihab A. Shawkat**,[8] **and Zahraa A. Jaaz**[1,9]

[1]*College of Computing and Informatics, Universiti Tenaga Nasional (UNITEN), Kajang, Malaysia*
[2]*Computer Engineering Techniques Department, Baghdad College of Economic Sciences University, Baghdad, Iraq*
[3]*Institute of Sustainable Energy, Universiti Tenaga Nasional (UNITEN), Kajang 43000, Selangor, Malaysia*
[4]*Department of Medical Instrumentation Technical Engineering, Medical Technical College, Al-Farahidi University, Baghdad, Iraq*
[5]*Computer Techniques Engineering Department, Al-Mustaqbal University College, Hillah 51001, Iraq*
[6]*Professional Engineers in Ontario, North York, Toronto, Ontario M2N 6K9, Canada*
[7]*Technical and Vocational University, Tehran, Iran*
[8]*University of Samarra, Samarra, Iraq*
[9]*Computer Department, College of Science, Al-Nahrain University, Jadriya, Baghdad, Iraq*

Correspondence should be addressed to Israa Al-Barazanchi; israa44444@gmail.com

Received 24 May 2022; Revised 12 July 2022; Accepted 16 July 2022; Published 15 September 2022

Academic Editor: Mohammed Al-Sarem

As of late 2019, the COVID19 pandemic has been causing huge concern around the world. Such a pandemic posed serious threats to public safety, the well-being of healthcare workers, and the overall health of the population. If automation can be implemented in healthcare systems, patients could be better cared for and health industries could be less burdened. To combat such challenges, e-health requires apps and intelligent systems. Using WBAN sensors and networks, a doctor or medical professional can advise patients on the best course of action. Patients' fitness could be assessed using WBAN sensors without interfering with their daily activities. When designing a monitoring system, system performance reliability for competent healthcare is critical. Existing research has failed to create a large device capable of handling a large network or to improve WBAN topologies for fast transmitting and receiving patient data. As a result, in this research, we create a multisensor WBAN (MSWBAN) intelligent system for transmitting and receiving critical patient data. To gather information from all cluster nodes and send it to multisensor WBAN, a novel additive distance-threshold routing protocol (ADTRP) is proposed. In small networks where data are managed by the transmitting node and the best data route is determined, this protocol has less redundancy. An edge-cutting-based routing optimization (ES-EC-R ES-EC-RO) is used to find the best route. The Trouped blowfish MD5 (TB-MD5) algorithm is used to encrypt and decrypt data, and the encrypted data are stored in a cloud database for security. The performance metrics of our proposed model are compared to current techniques for the best results. End-to-end latency is 63 ms, packet delivery is 95%, security is 95.7%, and throughput is 9120 bps, according to the results. The purpose of this article is to encourage engineers and front-line workers to develop digital health systems for tracking and controlling virus outbreaks.

1. Introduction

The ongoing COVID-19 endemic, poor lifestyle choices, insufficient stress relief, rising healthcare costs, and an aging population all posed significant challenges to governments and healthcare organizations around the world. The growing number of patients has necessitated the use of advanced technologies to enable doctors to remotely monitor patients via

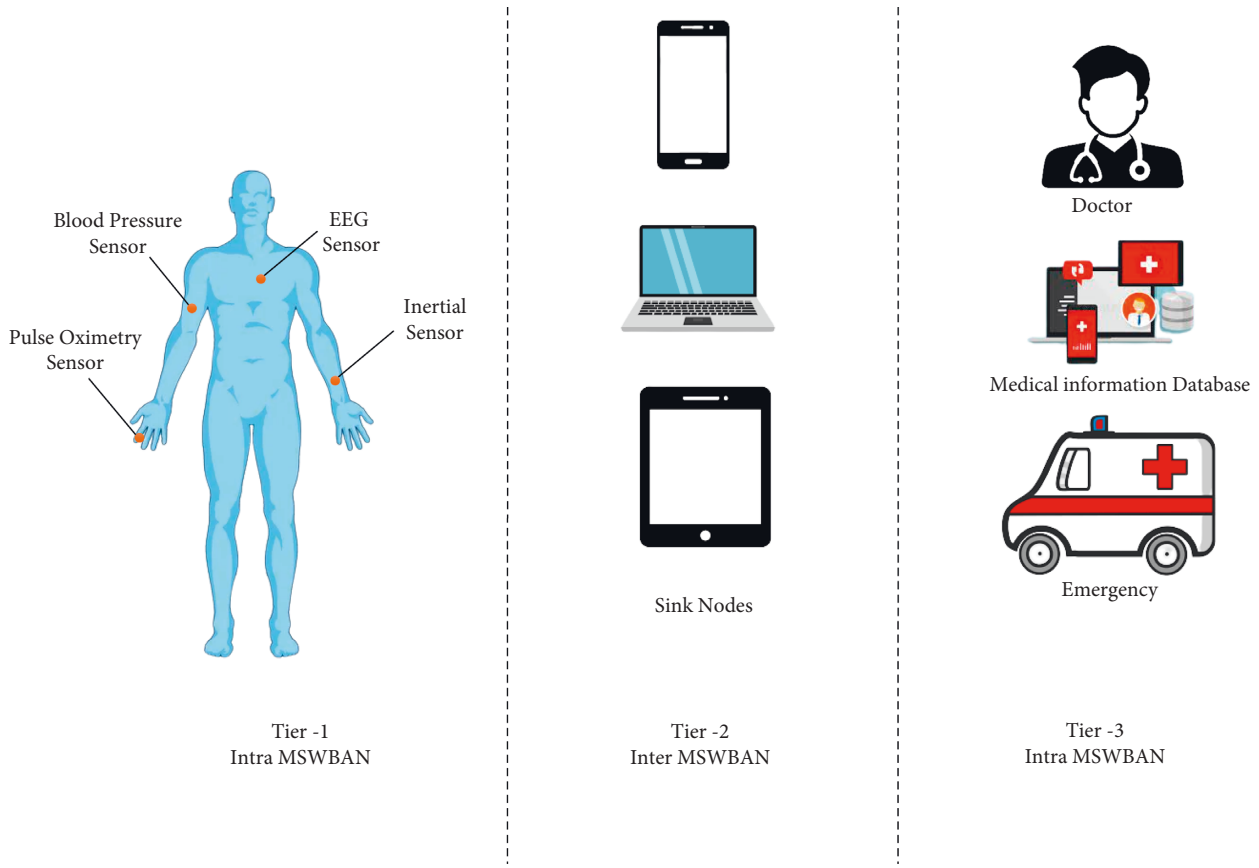

Figure 1: Architecture of MSWBAN.

wireless body area network (WBAN) sensors [1]. However, because WBAN networks involve remote access and sensitive and critical data, they necessitate extremely high levels of security and privacy during storage and processing. As a result, the installed WBAN infrastructure should always include a variety of security elements to ensure data protection, privacy, integrity, and confidentiality. Existing wearable device platforms are constrained by hardware capabilities, parameter estimation techniques, and software design [2].

An outbreak of a virus such as COVID19 can alter the worldwide health and economic landscape. It can result in massive monetary damages both locally and globally. To protect the healthcare systems from collapsing, the world urgently needs to use the Internet of medical things (IoMT) technologies to help monitor patients and save many lives. MSWBAN plays an essential part in IoMT in the healthcare sector, where multiple sensors are used to monitor various medical symptoms of patients [3]. WBAN necessitates the collection of data from sensor nodes in an effective and efficient manner in order to ensure the network's dependability. The cluster head selection scheme is one of the key schemes that contribute to the WBAN network's increased efficiency. From a group of nodes, a few are chosen as cluster heads (CHs). The data are then obtained by the CHs from "contributing nodes," which are nodes that are linked to one another. The nodes that send their readings to CH are typically located near the CH [4]. To be used in the clustering approach, the data collected by each sensor must be sent to the sink via the cluster head. When it comes to WSN power usage, clustering algorithm-based hierarchy routing protocols elect and rotate CHs at random. Inefficient CH, regardless of network size, may be chosen in certain circumstances, resulting in variable cluster sizes. Clustering algorithm-dependent hierarchical routing protocols employ a single cluster formation parameter and a probabilistic cluster selection approach. As a result, choosing CHs and building clusters is difficult in clustering algorithm-based hierarchy routing protocols [5].

Figure 1 depicts the MSWBAN's architecture. It has three levels. Wearable or implanted biosensors (ECG, EEG, temperature, blood pressure) capture the data through ZigBee and Bluetooth wireless technologies and transmit it to the body coordinator (BC). Intra-MSWBAN is another name for Tier 1. A BC in Tier 2—also referred to as Inter-MSWBAN—transmits patient data to a nearby access point or sink node. This gateway is a conduit for sharing patient data from Tier-1 to Tier-3. Using the Internet, the sink nodes transfer the gathered data to a distant medical facility or doctor in Tier 3 (also known as Beyond MSWBAN). Figure 2 shows the WBAN flowchart.

This paper proposes remote monitoring of COVID-19 patients using additive distance threshold routing protocols in the MSWBAN innovative system. The rest of the paper proceeds as follows; Part II contains the relevant literature as

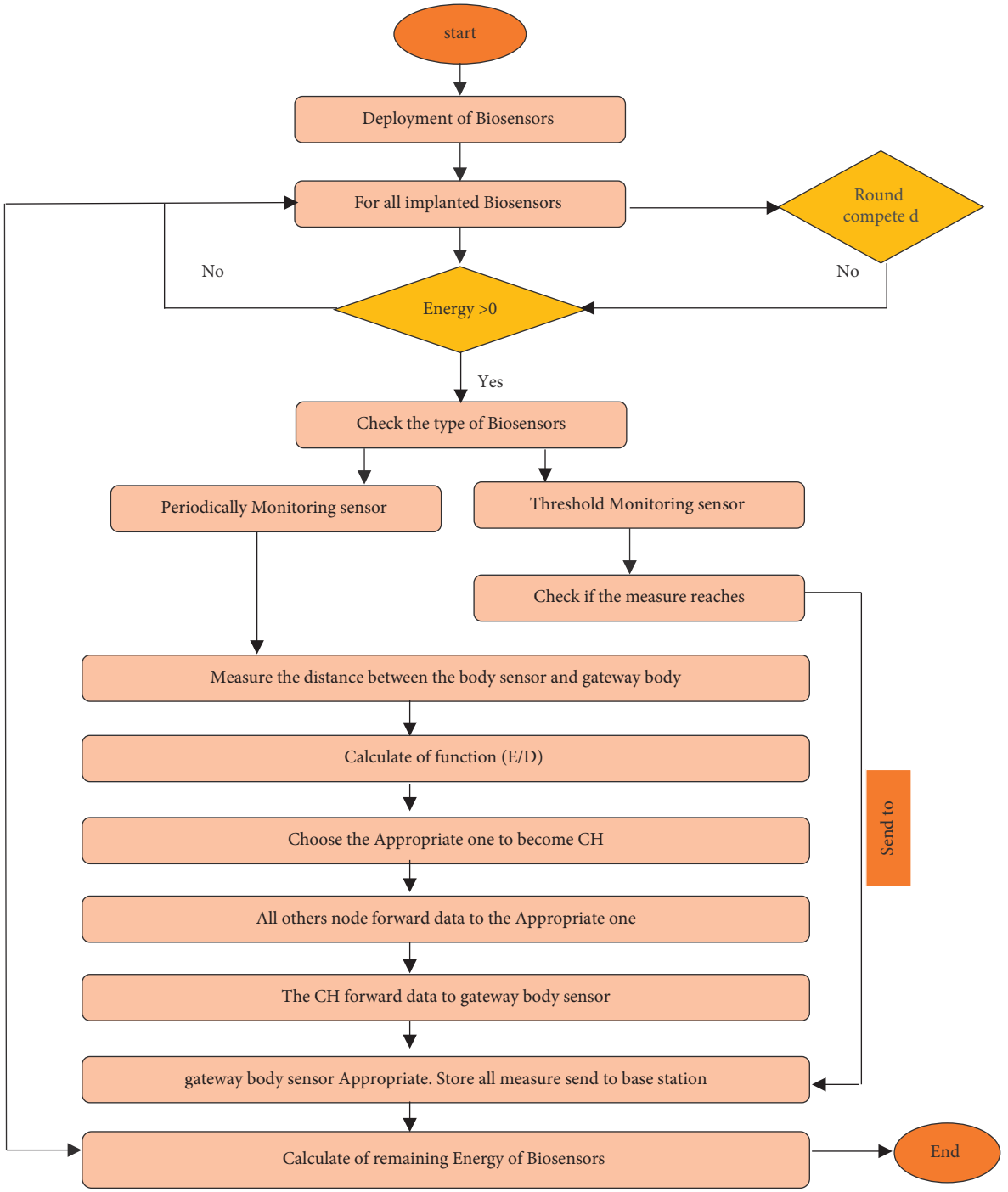

Figure 2: WBAN flowchart.

well as the problem research gaps. Part III explains the flow of the proposed form. Part IV investigates and compares the behaviour of the proposed method to previously established methods. Finally, Part V concludes the paper.

2. Related Works

Singla et al. [6] defined many security criteria for WBANs and conducted a comprehensive evaluation of current secure routing techniques. Many secure routing protocols have been evaluated in terms of security and performance, and an assessment based on these characteristics has been produced, while a comprehensive review of concern about security and privacy is presented about WBAN in [7]. A strategy to bridge the gap between current technological developments and the healthcare system has been presented in [8], in which WBAN sensors and networks may enable a doctor to assist a COVID-19-infected patient in making the best possible decision for themselves at the appropriate time. This situation enables the community to maintain social

distance while keeping hospitalized patients in a comfortable atmosphere. Nanosensors are employed in the wireless WBAN to continuously monitor a patient's medical health because of resource constraints and essential applications, improving security and privacy to a high degree offers various challenges. Majumder et al. in [9] conducted a thorough survey in the domain of WBAN. WBAN is a technological breakthrough that has made remote patient monitoring possible. When medical personnel is in low supply, and some patients need 24-hour monitoring, BAN is an important tool for such a scenario.

WBANs are used in both medical and nonmedical applications [10]. It has also thoroughly explored the different wireless technologies that WBAN can support. Routing protocols have affected one of the essential factors of assessing network efficiencies, such as power consumption, throughput, and delay. Researchers may compare routing protocols to help in the development of a certain protocol for a given application. In addition, wireless technologies that employed WBAN systems were investigated in [11]. It comprises miniature sensors that gather and send data across a wireless network, allowing medical professionals to monitor patients in their everyday lives and provide real-time medical diagnoses. Several wireless technologies have already shown value in WBAN applications, while others are still in the research phase. According to Jin et al. in [12], fever, cough, and expectoration were the early symptoms in 36 patients (80%), 23 patients (51%), and 15 patients (33%), respectively, at the commencement of illness. Senior patients (58) and their concomitant chronic diseases were independent predictors of a severe and critically sick population with a higher fatality rate. COVID-19 has the potential to harm a variety of organs in the human body. Treatment of COVID-19 patients with glucocorticoids is well-accepted. Furthermore, Basiri established in [13] that the coronavirus is an encapsulated virus of the RNA virus family. Fever, cough, and shortness of breath are present in the patients, and no definitive therapy or vaccination is available. Due to the body's generation of antibodies, the viral infection progressively becomes self-limiting. Using a novel lab test developed by the Centres for Diseases Control and Prevention, the SARS coronavirus, which causes "severe acute respiratory syndrome," has been identified. Traditional medicine seems to be beneficial in the treatment COVID-19 sufferers as well.

The major purpose of the framework is to bridge the gap between the current technologies and healthcare systems. WBAN, fog, cloud, and clinical decision support systems are combined to give a comprehensive paradigm for sickness diagnosis and monitoring. The framework is a powerful tool, and they expect it to have a significant impact on the spread of COVID-19 as well as a considerable reduction in healthcare costs [14]. WBSN and contemporary advances in the field were discussed in [15], which emphasized the need for remote monitoring for the elderly and chronically ill. The scientific notion of WBSN architecture, problems, healthcare applications, and their needs was conducted to meet the scientific idea of WBSN. Following that, the key critical part of the WBSN, such as data collection, fusion, risk assessment, and decision-making, is explored. Finally, the article suggests that increasing awareness of critical concerns and the future growth of WBSNs is a great way to monitor a patient's life. According to Qu et al. in [16], the introduction of WBSN has brought hope and a new era in the battle against population aging, chronic illnesses, and a lack of medical facilities. WBANs necessitate the development of routing protocols, which play a crucial role in communication stacks and have a significant impact on network performance. Furthermore, WBSN present issues, applications, and discoveries, and performance difficulties were discussed in [17]. The study covers WBAN Signal processing, network reliability, spectrum management, and security. As a result, they conclude the study by identifying various current and future research directions. On the other hand, a framework for evaluating COVID-19 prevention and protection strategies in hospitals was discussed in [18]. COVID-19 recommendations for preventative and protective measures, tight procedures, frequent audits, staff education and training, and active monitoring should emphasise the case hospital management. During the COVID-19 period, this suggested evaluation model is a novel effort in in-hospital assessment in preventative and safety actions in the healthcare industry. This methodology will serve as a continual evaluation tool for hospital management looking to enhance their COVID-19 prevention efforts. Then, Rahman et al. in [19], demonstrated that WSN frameworks are widely utilised in applications such as healthcare and smart cities to collect and analyse real-time data and take appropriate actions based on demand of the application. Application-specific demands and requirements might play a significant role in deciding on a routing protocol for a WSN. In order to design an inefficient routing protocol, the networking infrastructure must be generalized, while application-specific limitations are ignored. During the quarantine period, a wearable gadget prototype is intended to remotely monitor the COVID-19 health symptoms of potentially infected patients (PIP). The 3D prototype incorporates a three-layer wearable body sensor, a web API layer, and a mobile front-end layer for an automated healthcare system to lessen stress and create a communication channel between physicians, medical authorities, and family responders [20]. WBANs provide information-based sickness diagnosis, allowing for early treatment. If attackers access the web, the whole network will become wasteful. Using biometric and digital signature technologies, this research proposes an integrated security framework that counters intruder assaults and improves network security, resulting in a more trustworthy network and stability [21]. Sangeetha Priya et al. in [22] propose a security-conscious trustworthy cluster established routing protocol for WBS. Many human-centric applications rely on large-scale deployments of wireless body sensor networks. Sensor hubs' vitality reserve funds are among the most crucial components of such systems to extend their life spans. The wireless body area sensor system must also include secure routing to reduce the risk of information leakage. Furthermore, new security concerns has

Table 1: Summary of related works.

Reference	Methods	Advantages	Drawbacks
Singla et al. [6]	Secure routing technique	The pricey secure data transfer is not required if no incident is found.	Bandwidth is wasted. It requires a high computational cost for encryption and needs more RAM.
Jabeen et al. [8]	Nanosensors	It gives a high surface area/volume ratio by increasing their sensitivity.	These sensors always adopt a similar fundamental process.
Majumder et al. [9]	Remote patient monitoring	Increasing communication options strengthen the patient-provider connection and raise customer loyalty and satisfaction.	It relies on technology, which some people may not be able to afford. Reliable Internet connections are required for RPM systems.
Kaur et al. [10]	Routing protocol	No route setup delay for connections over small distances. Reactive routing for farther-off destinations results in reduced routing overhead.	They depend on routable network protocols to function. Compared to other network devices, they are expensive.
Thomas and Suresh [18]	Hospital management	Every piece of data is accessible by approved login from anywhere in the globe. This form of communication has become considerably less expensive.	User interface and user experience (UI/UX design) are complex designs concerned with a data breach.
Rahman et al. [19]	WSN	Because it is scalable, any additional nodes or devices may be added at any moment.	Due to its limited speed architecture, it cannot be utilised for high-speed communication.
Paganelli et al. [25]	Multistage fuzzy rules	Fuzzy logic systems have a straightforward and reasonable structure. The fuzzy logic is typically applied in practical and business contexts.	In the large organization industry, it is used for dynamic, emotionally supporting networks and individual assessments.

been introduced by WBANs and the services, so that WBAN is evolving to suit these demands [23]. Detection method of COVID-19 is based on a multistage fuzzy rules' technique, with the CART algorithm used to generate the fuzzy rules [24]. The suggested strategy distinguished the growth of illness prediction accuracy according to the implementation outcomes. This study provides detailed specifications of an IoT-based [25] conceptual design for a COVID-19 patient monitoring system. The solution contains method for modifying this assessment approach, as well as ensuring the individualization of evaluations, and a legitimate and widely utilised early-warning score system for evaluating and monitoring hospitalized patients. Table 1 shows the related works.

3. Proposed Work

Figure 3 depicts a schematic illustration of the proposed approach. It includes the process of analysing the fuzzy logic dependent cluster head selection, multisensor wireless body area network deployment, sending node, receiving node, encryption using the trouped blowfish MD5 algorithm, cloud database, key generation, and authentication, decryption, distant monitoring of COVID-19 patients using additive distance-threshold routing protocol in MSWBAN innovative system.

3.1. Data User. This component collects personal information as well as serves illness symptoms. There are 493 COVID-infected and 206 noninfected individuals with symptoms, and the data are used to build a threshold routing protocol model. Following that, each new user inputs their information and signs into the system, and the suggested trouped blowfish MD5 algorithm model is used to safeguard COVID-19 patients' data [26].

3.2. Fuzzy Logic-Based Cluster Head Selection

3.2.1. CH Selection. Cluster-based routing is an energy-efficient strategy in which high-energy nodes process and transport data as clusters form. Low-energy nodes are in charge of detecting and transmitting data to the cluster heads. The cluster information routing protocol improves scalability, energy efficiency, and security. The longevity of the network should be maximized.

3.2.2. Cluster-Head Selection Using Fuzzy Logic. The FLCH-based clustering technique uses three input parameters to choose wireless sensor networks CHs [27]. Input variables for the model include remaining energy (RE), nodes centrality (NC), and distance to the base station (DBS). The residual energy of a node must be considered while determining whether it belongs to a CH or not. BS receives the information acquired by CH nodes, compiles it, and then sends it on to other nodes. One-hop adjacent nodes in R_c are are called Node Degrees (ND) based on the total number of one-hop neighbours. Neighbour-centricity (NC) describes a node when it is located between two other nodes in a ring. When the NC value is low, a node has a better chance of being selected as a CH.

$$NC = \frac{\sqrt{\sum_{i=1}^{ND} dis_i^2 / ND}}{\text{Ntk} - \text{Dimension}}. \quad (1)$$

The counting of neighbours in node's transmitting radius R_c is denoted in equation (1). In the $M \times M$ field region, "M" is the value *Ntk—Dimension*, and the distance between ith neighbouring nodes is represented by $dist_i^2$. The amount of energy consumed in data transmission increases the distance between the transmission and reception nodes. When selecting CH, the remaining energy in the sensors, as well as their maximum and minimum distances from the BS, are taken into consideration

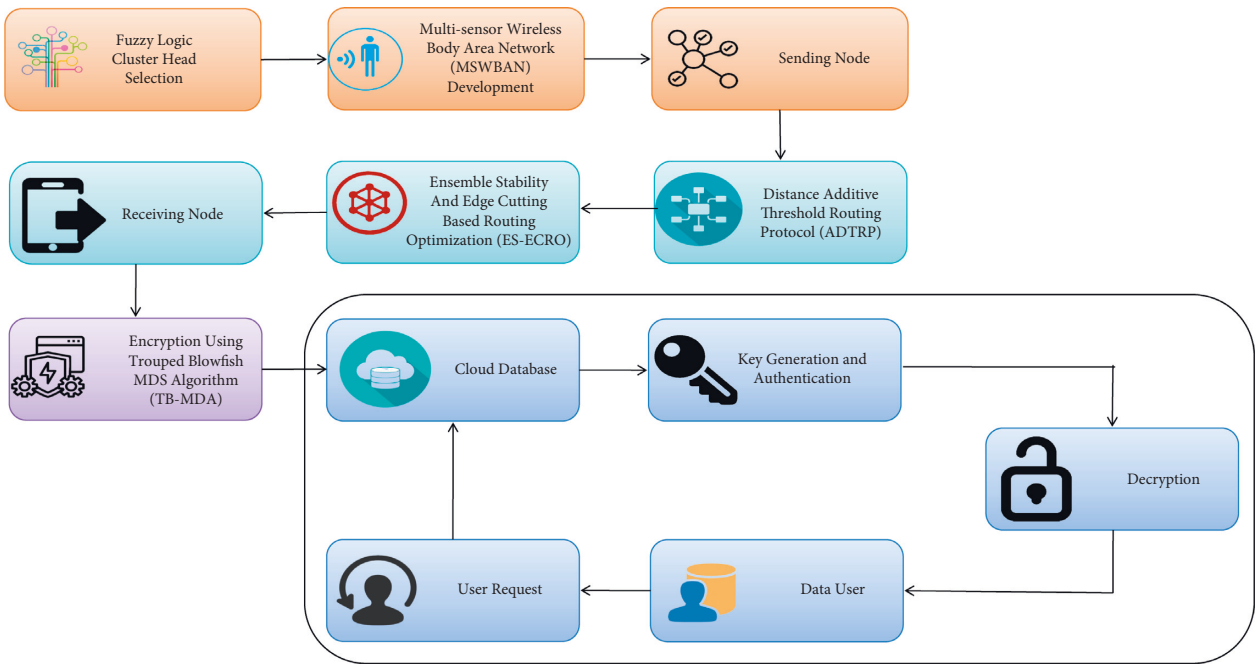

Figure 3: Schematic representation of the suggested methodology.

$$\text{Distance to } BS = \frac{d_i}{\alpha.\text{Ntk} - \text{Dimension}}, \tag{2}$$

$$\alpha = \frac{d_{\max}}{\text{Ntk} - \text{Dimension}}. \tag{3}$$

The distance between nodes i and the BS is denoted by d_i and the maximum length among a network node, and BS is $d_{\max}$ indicated by max. In contrast, α implies the network dimensional constant. When selecting the CHs, the remaining energy of the sensor is taken into account, as well as the sensors' and BS's maximum and minimum distances, the amount of energy used by each cluster of sensors, the quality criteria for collections, the sensor distribution, the group mean distance, and the cluster density. The four overall energy levels we proposed are low, medium, and high. They are the energy's "fuzzy linguistic variables" in their totality.

$$\text{Low} \begin{cases} 1 & \text{Energy} \le 0.25 \\ \dfrac{0.35 - \text{Energy}}{0.1} & 0.25 < \text{Energy} \le 0.35 \end{cases}, \tag{4}$$

$$\text{Medium} \begin{cases} \dfrac{\text{Energy} - 0.25}{0.25} & 0.25 < \text{Energy} \le 0.5 \\ \dfrac{0.6 - \text{Energy}}{0.1} & 0.5 < \text{Energy} \le 0.36 \end{cases}, \tag{5}$$

$$\text{High} \begin{cases} \dfrac{\text{Energy} - 0.5}{0.3} & 0.5 < \text{Energy} \le 0.8 \\ \dfrac{0.89 - \text{Energy}}{0.09} & 0.8 < \text{Energy} \le 0.89 \end{cases}, \tag{6}$$

$$\text{Very High} \begin{cases} \dfrac{\text{Energy} - 0.8}{0.09} & 0.8 < \text{Energy} \le 0.89 \\ 1 & \text{Energy} > 0.89 \end{cases}. \tag{7}$$

The following are the membership functions for the distance parameters:

$$\text{Near} \begin{cases} 1 & x \le c_1 \\ \dfrac{L - x}{L - c_1} & c_1 < x \le L \end{cases}, \tag{8}$$

$$\text{Average} \begin{cases} \dfrac{x - c_1}{L - c_1} & c_1 < x \le 1 \\ \dfrac{c_2 - x}{c_2 - L} & L < x \le c_2 \end{cases}, \tag{9}$$

$$\text{Far} \begin{cases} \dfrac{x - l}{L - c_1} & L < x \le c_2 \\ 1 & x > c_2 \end{cases}. \tag{10}$$

In the equations above, the BS minimum and maximum sensor distances are c_1 and c_2, respectively, and an average distance to the BS is denoted by L, which is calculated as follows,

$$L = \frac{(c_1 + c_2)}{2}. \tag{11}$$

The CHs are chosen to have the most energy and the shortest distance to the BS. As a result, numerous sensors in each cluster have the potential to be a CH, and the final CH is determined by which sensor best satisfies the set criteria. Figure 4 depicts the cluster head.

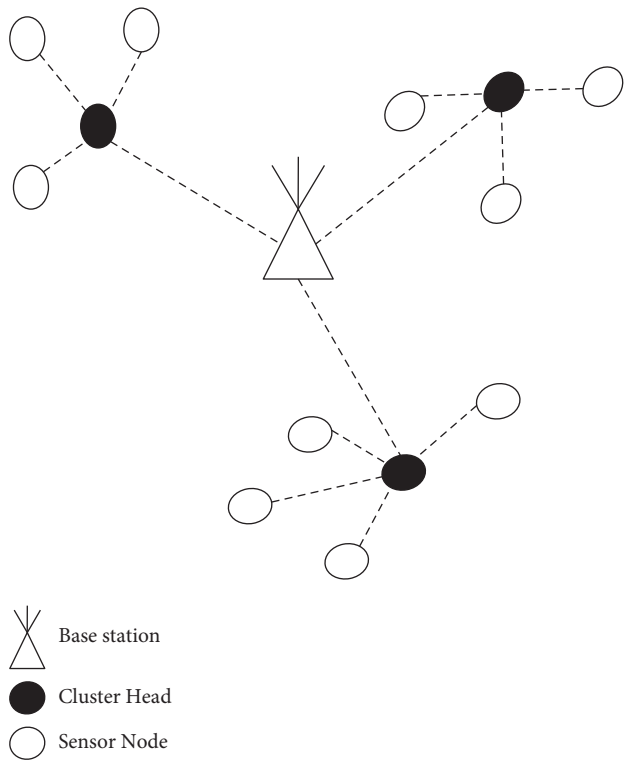

Figure 4: Cluster head.

(1) MSWBAN Development: the wireless body sensor connects or implants each sensor in multisensor WBAN. These devices monitor electrocardiograms, blood pressure, temperature, heart rate, pulse oximetry, and steps. The MSWBAN architecture may be divided into three subsystems: information capturing, transmitting, and processing. Body sensors oversee collecting physiological data and transferring it to the gateway, which then sends the data to a distant server for analysis. To construct sophisticated MSWBAN systems, the first step is to detect and acquire physiological data about the patient and his surroundings. There has been a rise in the need for a greater depth of information from sensors. Fusing the outputs from many sensors may be the only method to access that breadth of knowledge when a single sensor modality is insufficient. However, in the context of our proposed system, different sensors employ different physical principles, cover distinct information spaces, and provide data in various forms at various sampling rates. The data collected have a various resolution, accuracy, and dependability characteristics. It is essential to utilise a technique that can appropriately fuse data from diverse sources considering these impacts to get the required detection to work successfully. To coordinate a peripheral module and execute the data processing function, data collecting capabilities are equipped with several sensors, wireless data transmitting modules, electricity supply modules, and a microcontroller. MSWBAN's application-based design is inherently static. Infrastructure and application are inextricably linked. The sensors platform, gateway, and server would all have to be updated if the application intelligence were to be changed. Developing a sensor platform, gateway, and remote server from the ground up will need a distinct physical structure for each application. However, deploying a new application is not simple; instead, it involves a lengthy period. Therefore, future application innovations are hampered. Patients using MSWBAN in healthcare typically enjoy complete freedom of movement when body sensors are linked to their bodies. They are occasionally in proximity or within the nearby MSWBAN in such cases. Because of this movement, packets are lost, and the error rate rises. As a result, in MSWBAN, a robust handover mechanism should be provided [27].

(2) COVID19 Patient Monitoring Via MSWBAN: MSWBAN is a kind of external monitoring health care system (eHealth), which is a type of continuous health monitoring system that provides local monitoring and control. To treat the ill, these systems do not need frequent hospitalizations. It's a win-win situation since it prevents last-minute scrambling and saves time.

For MSWBAN, most major challenge is its energy consumption since the biosensors it employs have a charging leakage issue and must be replaced after a set of time. An IoT system for the real-time healthcare monitoring systems for the prediction of a preliminary phase of COVID-19 is shown in this study using wearable sensors, including temperature, heartbeat, and pressure sensors. Body temperature, respiratory symptoms, and oxygen levels may all be measured with these biosensors. This gadget communicates biosensor data to the cloud utilizing low-power LoRa technology using Arduino, My Signal hardware, and LoRa technology. To simulate and monitor patients, back-end servers show real-time data, while cloud servers gather, handle, and transport that data [28].

3.3. Distance Additive Threshold Routing Protocols. In MSWBAN, there are two types of threshold routing systems: data transmission and data reception. During the threshold routing of aggregated data from CHs to the BS, the routing protocol [6] utilizes an election energy threshold, T_{nhCH}, to choose the next CHs.

$$E_{Uy}(k,d) = E_{\text{elec}} \cdot k + E_{\text{amp}} \cdot K.\, d^2, \tag{12}$$

$$E_{sy}(k) = E_{\text{elec}} \times k, \tag{13}$$

where the per-bit dissipation of transmitter circuits is denoted by E_{elec}, the transmitter amplifier dissipation is denoted by E_{amp}, the bit length is given by k, whereas the transmission line length among the sender and receiver is given by d.

Threshold routing in an MSWBAN is the process of transmitting detected data to the Base station through various protocols rather than sending it directly to the Base station. Every round, threshold routing across CHs involves passing aggregated data via many CHs to the BS. When the CH is next to the BS, information is sent directly to the base station; however, when the distance between BS and CH is significant, high energy is spent in transferring the sensed data to the BS via the radio energy mode. During network

configuration, all sensor networks communicate their residual energy (RE) levels and locations to the base station (BS). As a result, the BS has comprehensive awareness of the whole network region. During data routing to the BS, the threshold is utilised to decide which CH should serve as the next protocol.

$$E_{nhCH} = \frac{\sum_{n=1}^{l} \mathrm{RE}\,(\mathrm{neighbour}\,CHs)}{t}, \tag{14}$$

where E_{nhCH} that is, the election energy threshold, the residual energy of neighbour CHs is denoted by RE, and t is the number of neighbour CHs.

$$d_0 = \sqrt{\frac{E_{amp1}}{E_{amp2}}}. \tag{15}$$

The threshold value, together with the estimated distances of the nearby CHs, is utilised to determine the following protocol in the threshold route's creation. A distance threshold value, the maximum transmission distance, is determined by d_0.

3.4. Encryption Using Trouped Blowfish md5 Algorithm. Blowfish md5 algorithm is a symmetric technique, and the same key is used for encryption and decryption. It is utilised in the encryption process because it is substantially quicker than DES and has a strong encryption rate with no practical cryptanalysis method.

3.4.1. Blowfish Algorithm. Blowfish's cryptographic calculation is productive and customizable, with several parameters ("key size, square size, number of rounds") that may be utilised to combine certain quality with power consumption and computational overhead. With the right conditions, this blowfish calculation might work well for MSWBAN applications with varying data quantities. The blowfish computation had a positive influence on the cryptography business when compared to algorithms. The author also proposed a multipurpose security system that uses near-field communication to connect the physical and logical worlds, as well as remote sensor organisers for data and vaccination security [29]. (Algorithm 1 shows the Pseudocode for blowfish, and algorithm 2 shows the Pseudocode for MD5.)

3.4.2. MD5 Algorithm. A 512 bit block of information (each of which has sixteen 32 bit subblocks) makes up an MD5 message (Message-Digest algorithm). There are four connected 32 bit barriers to document honesty in MD5's 128 bit message processing.

3.5. Key Generation and Authentication. As soon as the patient register, a physician will be assigned. For initial password-based validation, physicians and patients use a secure password (MD5)-based technique. When a doctor logs into the system and views patient data, the system compares the doctor's palm/thumb picture scan reading to the recorded information. Access to the system will be granted after the doctor's ID is validated to ensure authenticity. The patient's palm/thumb is used to produce a biological key for security purposes.

3.6. Decryption. Decryption will begin only once authentication has been performed by extracting an authentication code or frame value from the previously created frame and completing the whole method for building an authentication code as specified. An encrypted version of the patient's data is stored in the MSWBAN Client, which comprises a collection of sensors and a control unit. Data consumers may check the cypher text's authenticity and decode the data if they have the decryption characteristics defined by the signature access structure when accessing data from the MSWBAN client [30].

3.6.1. Performance Analysis. We conducted extensive simulation experiments using Castalia-3.2 simulator, built on the OMNeT++ platform, to verify our proposed work. Figures 5–8 shows the comparison of performance metrics, namely packet delivery ratio, security level, throughput, and end-to-end delay. The approaches include the Geographic Routing Protocol (GRP), Optimized Energy Efficient Secure Protocol (EESR), Secure and energy-efficient framework-Internet of Medical Things (SEF-IoMT), Energy Efficient Routing Protocol (EERP), and (ADTRP + TD-MD5) additive distance threshold routing with trouped blowfish MD5. Table 2 shows the comparative analysis of metrics for existing and proposed methods, and Table 3 represents the simulation parameters.

End-to-end latency is determined by calculating the total amount of time needed for data transmission from the sender node to the destination node. Then, the delay in normal mode is determined using the following formula:

$$D = \frac{1}{n} \sum_{i=1}^{n} \left(Tr_i - Ts_i\right) \times 1000\ [ms], \tag{16}$$

where D is the average end-to-end delay, i is the packet identifier, Tr_i is the reception time, Ts_i is the send time, n is the number of packets successfully delivered.

Figure 5 represents the end-to-end delay results with proposed and existing approaches. Every millisecond a packet travels from the sender to the receiver is counted as an end-to-end latency measurement (mS). From the above figure, compared to the existing methods such as the dual sink approach using WBAN, novel framework for software-defined WBAN, fragmentation through MAC IEEE 802.15.4 to delay performance, efficient and reliable direct diffusion routing protocol in WBAN, and the proposed method of ADTRP + TB-MD5 has low end-to-end delay. The previous approaches like GRP has 35%, OEESR has 30%, SEF-IMOT has 25%, and EERP has 20% for the packet delivery ratio. The proposed ADTRP + TB-MDS has an 18% of packet delivery ratio.

The sum of the number of packets received to the number of packets issued is known as the packet delivery ratio. The following formula is used to determine the packet delivery ratio:

Step 1: Input (64 bit) X as the text.
Step 2: In the text, there are two 32 bit halves: X_L and X_R.
Step 3: For $I = 1$ to 16:
$X_L = X_L$ XOR PI.
$X_R = F(X_L)\text{XOR}\, X_R$
X_L And X_R is switched.
Next, I.
Again X_L and X_R are switched (The last switch was undone).
$X_R = X_R$ XOR P_{17}
$X_L = X_L$ XOR P_{18}
Combined X_L and X_R
Step 4: Calculate Function f:
X_L is split into four eight-bit quarters: A, B, C, and D $f(X_L) = ((S_1, A + S_2, B \bmod 232)$ XOR $S_3, C) + S_4, D \bmod 232$.
Decryption:
Instead, the decryption is similar, except the reverse order of $P_1, P_2 \ldots\ldots\ldots\ldots P_{18}$ is used.
Generation key:
Step 1: Initiated X boxes and P arrays.
Step 2: The 32 critical bits of the first P array are XOR'd with the 32 key bits of the second P array, and so on.
Step 3: The approach described above is used to encrypt all zero strings.
Step 4: new input is provided by P_1 and P_2
Step 5: Using sub-keys, a completely new P_1 and P_2 have been encrypted.
Step 6: P_3 and P_4 are the newly generated outputs.
Step 7: Repeating this method 512 times yields a fresh P array and four S-boxes to be calculated.

Algorithm 1: Pseudocode for blowfish.

Step 1: The no of input bits is verified.
Step 2: A process of adding additional bits to the messaging input (MI) such that the total data length is equivalent to 512 multiples
Step 3: m is the result of adding 64 bit MI to the output of step 2.
Step 4: The blocks from m to b are separated (512 bits each).
Step 5: This is a list of blocks, each with 32 bits, from b to x (16).
Step 6: The algorithm has four rounds, each with 16 steps (64 steps in total).
Step 7: There are four hex-encoded shift registers, each with a capacity of 32 bits.
reg a = [7 6 5 4 3 2 1 0] 32- bits $[a] = [d]'$
reg b = [f e d c 8 a 9 7] 32- bits $[b] = [c]'$
reg c = [8 9 a b c d e f] 32- bits $[c] = [d]'$
reg d = [0 1 2 3 4 5 6 7] 32- bits $[d] = [a]'$
Step 8: aa, bb, cc, & dd are used to temporarily store the a, b, and c values.
Step 9: Several variables f, g, h, and I are involved in the algorithm processing. Shown below is a one-step operation:
$a = b + (a + f(b, c, d)) + x_i[k] + t[i] <<< S$
where.
$x_i\ [k] \leftarrow$ is the 32 bit ck^{th} word of x_i
$<<<S \leftarrow$ left circular shift of S bits.
After each round's final output is added, the first round's input is used as the output.
Step 10: The output bit depth is increased to 128 bits

Algorithm 2: Pseudocode for MD5.

$$\text{Packet delivery ratio} = \frac{\sum \text{total packets received by all destination nodes}}{\sum \text{total packets send by all source nodes}} \times 1000. \tag{17}$$

Packet delivery ratio results with proposed and existing approaches are shown in Figure 6. Packet delivery ratio measures the proportion of sending packets to received packets. From the above diagram, compared to the current methods such as GRP, OEESR and SEF-IoMT, and EERP, the proposed method of ADTRP + TB-MD5 has a high packet delivery ratio. The earlier methods, such as GRP, OEESR and SEF-IoMT, and EERP, had packet delivery ratios of 28%, 25%, 29%, and 33%, respectively. The suggested ADTRP + TB-MD5 has a packet delivery ratio of 40%. The

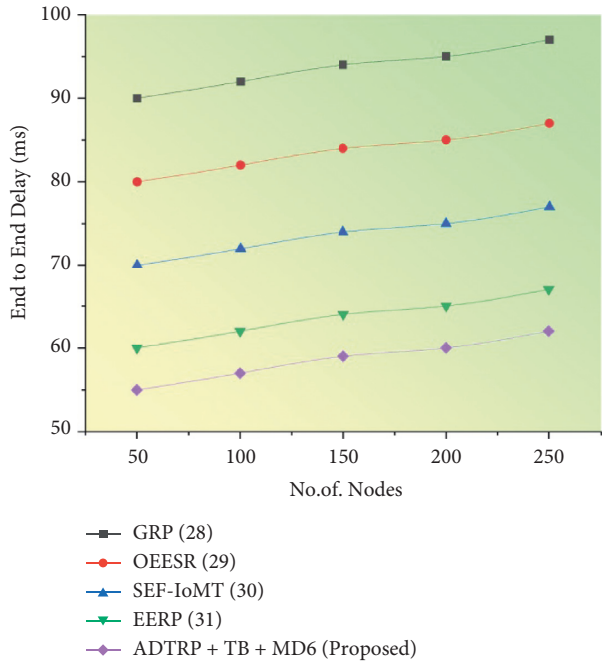

Figure 5: End-to-end delay results of the proposed methodology.

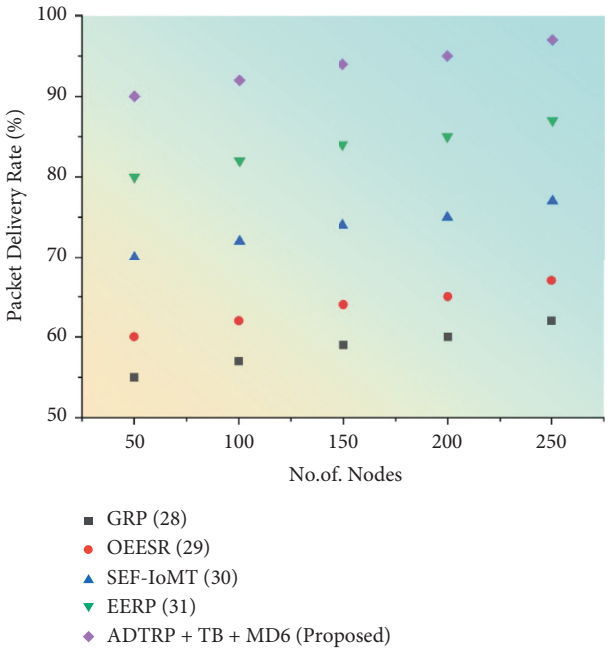

Figure 6: Packet delivery ratio results of the proposed methodology.

current technique has a larger overall packet loss percentage during certain data transmission times in the sensor network than our recommended alternative.

Figure 7 represents the security level results with proposed and existing approaches. In the above diagram, compared to the current methods such as GRP, OEESR, SEF-IoMT, and EERP, the proposed method of ADTRP + TB-MD5 has high security.

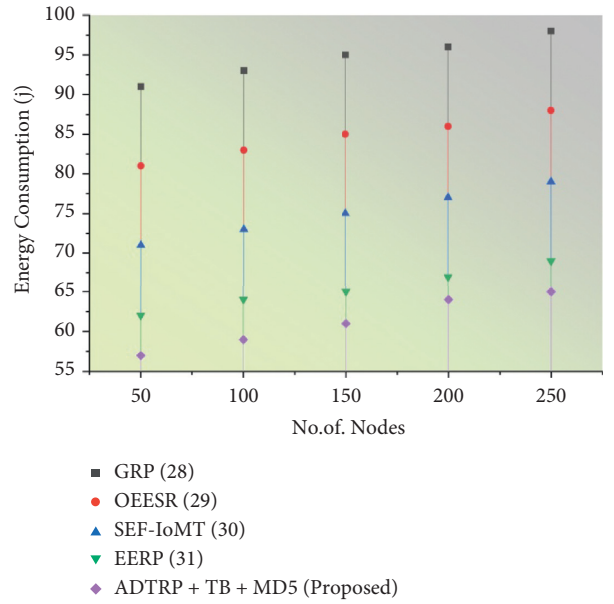

Figure 7: Energy consumption results of the proposed methodology.

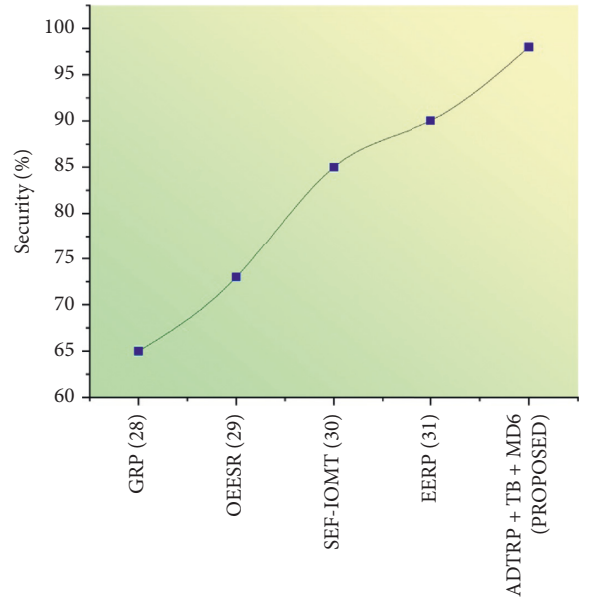

Figure 8: Comparison of security level for the existing and proposed methodology.

Security is a wide concept that incorporates many different technologies, tools, and procedures. It is a collection of guidelines and settings intended to safeguard the reliability, accessibility, and integrity of computer networks and data. Figure 8 shows the comparison of security levels for existing and proposed work. The security level of different encryption techniques is examined. GRP, OEESR, SEF-IoMT, and EERP, the proposed method of ADTRP + TB-MD5 has a high security level. The suggested approach of ADTRP + TB-MD5 has a high security level of 98%, whereas

Table 2: Comparative analysis of the proposed methodology.

S. no	Classification methods	End-to-end delay (ms)	Packet delivery rate (%)	Security level (%)	Throughput (bps)
(1)	GRP [31]	82	90	81	8460
(2)	OEESR [32]	7	93	88	8830
(3)	SEF-IoMT [33]	72	92	87	8786
(4)	EERP [33]	81	81	80	8086
(5)	ADTRP + TB-MD5 [proposed]	63	95	95.7	9120

Table 3: Simulation parameters.

S.no	Parameter	Value
(1)	No. of nodes	250
(2)	Time	270 s
(3)	Energy consumption	16.3 j
(4)	Transmission power	−15 dBm
(5)	No. of packets	250
(6)	Depth threshold	10 m
(7)	Min: and max: communication range	225 m, 255 m
(8)	Packet generation frequency	0.02 pkts/min
(9)	Transmission range	32 cm
(10)	Node displacement	0–5 m/s
(11)	Number of rounds taken for simulation	450 rounds
(12)	Number of sinks	1
(13)	Data processing rate	15,000 bits/s
(14)	Temperature threshold	45°C
(15)	SNR	16 dB

GRP achieves 65%, OEESR scores 73%, SEF-IoMT gets 85%, and EERP gets 90%.

The production rate of a specified process during a predetermined time period is known as throughput.

$$\text{Throughput} = \frac{\text{Number of units produced}}{\text{Time period}}. \quad (18)$$

The most apparent goal of any efficient system is to increase throughput. However, remember that precision is more important than speed. When errors are made, productivity is reduced. The amount of data transmitted in a communication environment is referred to as throughput. It refers to the quantity of information or packets sent from the source node to the destination node. Throughput is calculated as the amount of traffic received minus traffic transmitted divided by the total number of data packets received.

Figure 9 represents the throughput results with proposed and existing approaches. Bits-per-second (BPS) is a unit of measurement for the quantity of data sent by a network system. The suggested approach of ADTRP + TB-MD5 has a high throughput of 98 bps when compared to the current methods at the 250th node, where GRP attains 69 bps, OEESR attains 79 bps, SEF-IoMT attains 84 bps, and EERP attains 88 bps.

The encryption is the amount of time required to transform plaintext into ciphertext. In contrast, decryption time restores the plaintext from the received ciphertext. Decryption, on the other hand, recovers the plaintext from the received ciphertext. The speed of every algorithm is inversely related to the quantity of data it must process. For the encryption and decryption execution time, the suggested

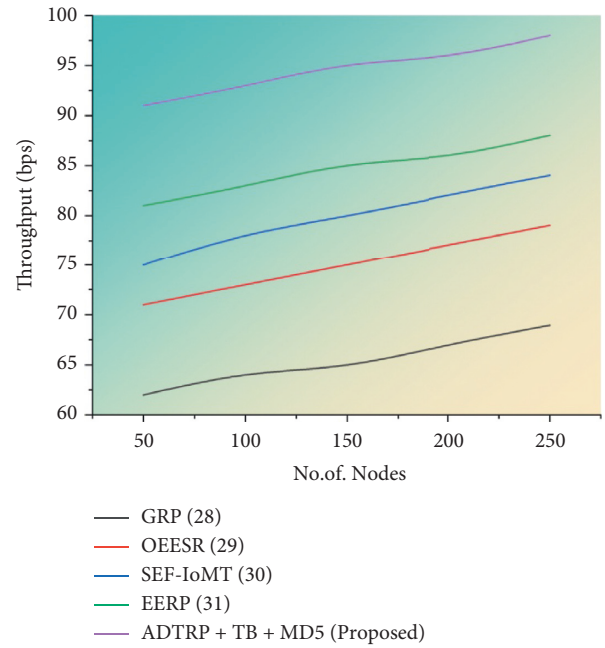

Figure 9: Throughput results of the proposed methodology.

method and existing approach were compared. Figures 10 and 11 illustrate the outcomes. The figures show that the suggested technique requires less calculation time for encryption and decryption.

The overall comparison of proposed and existing methods shows that the proposed methods are high in security levels, packet delivery, and throughput and low in end-to-end delay.

4. Discussion

Figures 5–8 compare throughput, end-to-end delay, packet delivery ratio, the security level for the existing method, and proposed plans. The current approaches are the dual sink approach using WBAN, a novel framework for software-defined WBAN, fragmentation through MAC IEEE 802.15.4 to delay performance, efficient, and reliable direct diffusion routing protocol in WBAN, and the proposed method is additive distance threshold routing protocols (ADTRP + TB-MD5). The proposed method, ADTRP + TB-MD5 has an end-to-end delay of 63 ms, and the existing techniques GRP has 82 ms, OEESR has 7 ms, SEF-IoMT has 72 ms, EERP has 81 ms. So, compared to existing methods, the proposed plans perform better in terms of end-to-end delay. The proposed method, ADTRP + TB-MD5, has a packet delivery ratio of

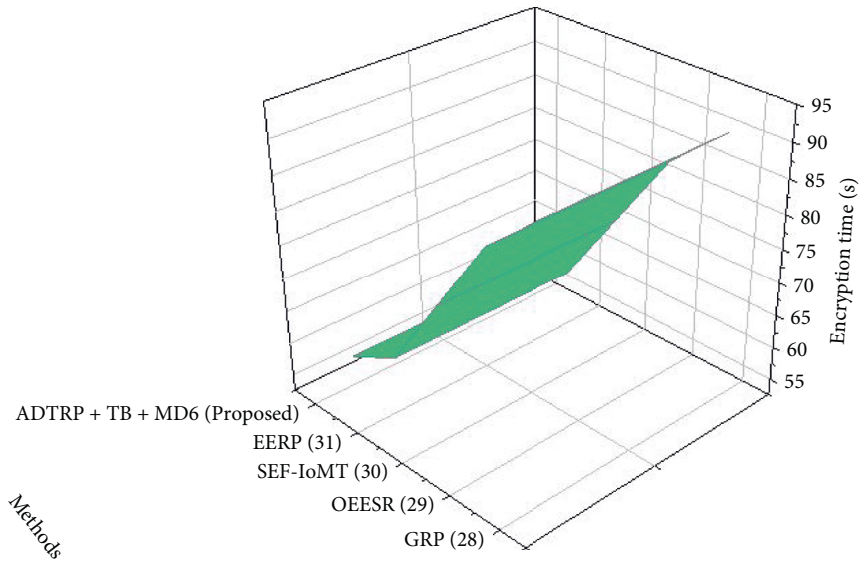

Figure 10: Encryption time results of the proposed methodology.

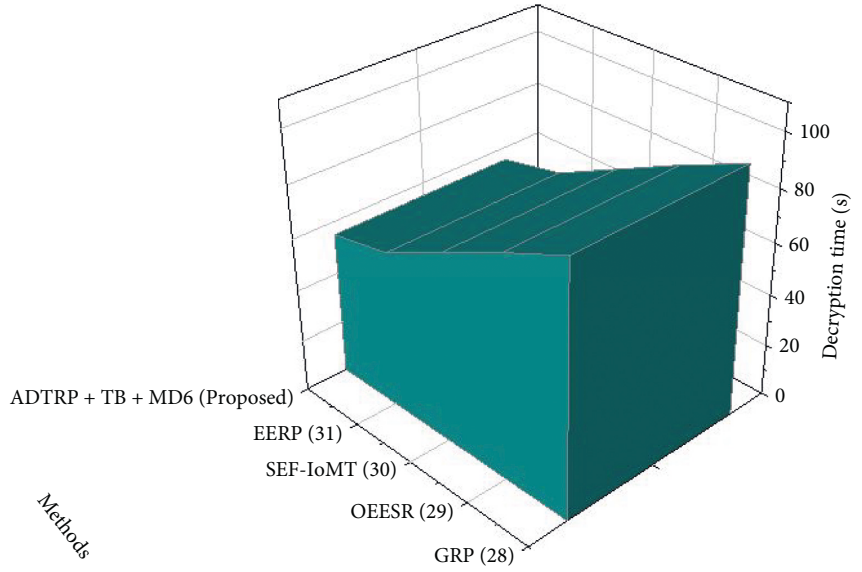

Figure 11: Decryption time results of the proposed methodology.

95% and the existing techniques, GRP, has 90%, OEESR has 93%, SEF-IoMT has 92%, EERP has 81%. So, compared to existing methods, the proposed technique performs better in terms of packet delivery ratio. The security level of the proposed method ADTRP + TB-MD5 is 95.7%, and in the existing process, GRP is 81%, OEESR is 88%, SEF-IoMT is 87%, and EERP is 80%. Hence, compared to existing methods, the proposed techniques perform better in terms of security level. In terms of throughput delay, the proposed method, ADTRP + TB-MD5, has 9120 Mbps, and the existing plans, and GRP has 8460 Mbps, OEESR has 8830 Mbps, SEF-IoMT has 8786 Mbps, and EERP has 8086%. So, compared to existing approaches, the proposed method is better in terms of throughput. The overall comparison of all parameters shows that the proposed method performs better.

5. Conclusion

The detection and prevention of COVID-19 are major concerns all over the world. As a result of this research, a model for an energy-efficient multisensor wireless body area network that is capable of monitoring COVID-19 patients has been developed. When a user reports symptoms to the cloud, the additive threshold routing protocol analyzes them to determine whether or not the user has COVID-19. If a user has been reported as infected with COVID-19, the MSWBAN will always keep a record of their infection status

in the database. It is possible that in the future, new categorization algorithms will be utilised to improve the MSWBAN's accuracy as well as its long-term viability. Using parallel and distributed processing based on microservices achieved through GPU grids, the proposed health application would be able to analyse multiple data flows coming from various devices for the purposes of machine learning and pattern recognition. In addition to that, and as was mentioned earlier, it will utilise federated learning approaches in order to monitor and artificially reason about data streams coming from a large number of MSWABNs.

Data Availability

The data used to support the findings of this study have been deposited at https://doi.org/10.1109/ISMS.2018.00031.

Additional Points

The schematic representation of the suggested technique includes the process of analysing the fuzzy logic dependent cluster head selection, wireless body area network deployment, sending node, receiving node, encryption using the trouped blowfish MD5 algorithm, cloud database, key generation, and authentication, decryption, distant monitoring of COVID-19 patients using additive distance-threshold routing protocol in WBAN innovative system.

Conflicts of Interest

The authors declare no conflicts of interest.

Acknowledgments

The authors would like to acknowledge the publication support through J510050002-BOLDREFRESH2025-CENTRE OF EXCELLENCE from the iRMC of Universiti Tenaga Nasional (UNITEN).

References

[1] H. R. Abdulshaheed, H. H. Abbas, E. Q. Ahmed, and I. Al-Barazanchi, "Big Data Analytics for large scale wireless body area networks; challenges, and applications," in *Proceedings of the International Conference of Reliable Information and Communication Technology*, pp. 423–434, Springer, Cham, March 2022.

[2] K. Siva Bharathi and R. Venkateswari, "Security challenges and solutions for wireless body area networks," in *Computing, Communication and Signal Processing*, pp. 275–283, Springer, Singapore, 2019.

[3] D. M. S. Bhatti, R. A. Khalil, N. Saeed, and H. Nam, "Detection and Spatial Correlation analysis of infectious Diseases using wireless body area network under Imperfect wireless channel," *Big Data*, vol. 10, no. 1, pp. 54–64, 2022.

[4] J. Jean Justus, M. Thirunavukkarasan, K. Dhayalini, G. Visalaxi, A. Khelifi, and M. Elhoseny, "Type II fuzzy logic based cluster head selection for wireless sensor network," *Computers, Materials & Continua*, vol. 70, no. 1, pp. 801–816, 2022.

[5] H. El Alami and A. Najid, "Fuzzy logic based clustering algorithm for wireless sensor networks," in *Sensor Technology: Concepts, Methodologies, Tools, and Applications*, pp. 351–371, IGI Global, 2020.

[6] R. Singla, N. Kaur, D. Koundal, and A. Bharadwaj, "Challenges and developments in secure routing protocols for healthcare in WBAN: a comparative analysis," *Wireless Personal Communications*, vol. 122, no. 2, pp. 1767–1806, 2022.

[7] M. S. Hajar, M. O. Al-Kadri, and H. K. Kalutarage, "A survey on wireless body area networks: architecture, security challenges and research opportunities," *Computers & Security*, vol. 104, Article ID 102211, 2021.

[8] T. Jabeen, I. Jabeen, H. Ashraf et al., "A Monte Carlo based COVID-19 detection framework for smart healthcare," *Computers, Materials & Continua*, vol. 70, no. 2, pp. 2365–2380, 2022.

[9] A. B. Majumder, S. Gupta, and D. Singh, "A survey paper on algorithms of wireless body area network," in *Applications of Networks, Sensors and Autonomous Systems Analytics*, pp. 335–342, Springer, 2022.

[10] R. Kaur, R. Pasricha, and B. Kaur, "A study of wireless body area networks and its routing protocols for healthcare environment," *Recent Advances in Electrical & Electronic Engineering (Formerly Recent Patents on Electrical & Electronic Engineering)*, vol. 13, no. 2, pp. 136–152, 2020.

[11] H. Taleb, A. Nasser, G. Andrieux, N. Charara, and E. Motta Cruz, "Wireless technologies, medical applications and future challenges in WBAN: a survey," *Wireless Networks*, vol. 27, no. 8, pp. 5271–5295, 2021.

[12] A. Jin, B. Yan, W. Hua et al., "Clinical characteristics of patients diagnosed with COVID-19 in Beijing," *Biosafety and Health*, vol. 2, no. 2, pp. 104–111, 2020.

[13] M. R. Basiri, "Theory about treatments and morbidity prevention of corona virus disease (Covid-19)," *J Pharm Pharmacol*, vol. 8, no. 3, pp. 89-90, 2020.

[14] N. El-Rashidy, S. El-Sappagh, S. M. R. Islam, H. M. El-Bakry, and S. Abdelrazek, "End-to-end deep learning framework for coronavirus (COVID-19) detection and monitoring," *Electronics*, vol. 9, no. 9, p. 1439, 2020.

[15] A. S. Jaber and A. K. Idrees, "Wireless body sensor networks: applications, challenges, patient monitoring, Decision making, and machine learning in medical applications," in *AI and IoT for Sustainable Development in Emerging Countries*, pp. 417–437, Springer, 2022.

[16] Y. Qu, G. Zheng, H. Ma, X. Wang, B. Ji, and H. Wu, "A survey of routing protocols in WBAN for healthcare applications," *Sensors*, vol. 19, no. 7, p. 1638, 2019.

[17] Q. Liu, K. G. Mkongwa, and C. Zhang, "Performance issues in wireless body area networks for the healthcare application: a survey and future prospects," *SN Applied Sciences*, vol. 3, no. 2, pp. 155–219, 2021.

[18] A. Thomas and M. Suresh, "Assessment of COVID-19 prevention and protection measures in hospitals," *Cleaner Engineering and Technology*, vol. 7, Article ID 100440, 2022.

[19] M. R. Rahman, M. M. Islam, A. I. Pritom, and Y. Alsaawy, "ASRPH: application specific routing protocol for health care," *Computer Networks*, vol. 197, Article ID 108273, 2021.

[20] N. Al Bassam, S. A. Hussain, A. Al Qaraghuli, J. Khan, E. Sumesh, and V. Lavanya, "IoT based wearable device to monitor the signs of quarantined remote patients of COVID-19," *Informatics in Medicine Unlocked*, vol. 24, Article ID 100588, 2021.

[21] K. Siva Bharathi and R. Venkateswari, "Development of an integrated security model for wireless body area networks," in

Applied Information Processing Systems, pp. 351–359, Springer, 2022.

[22] N. Sangeetha Priya, R. Sasikala, S. Alavandar, and L. Bharathi, "Security aware trusted cluster based routing protocol for wireless body sensor networks," *Wireless Personal Communications*, vol. 102, no. 4, pp. 3393–3411, 2018.

[23] S. Ayed, L. Chaari, and A. Fares, "A survey on trust management for WBAN: Investigations and future directions," *Sensors*, vol. 20, no. 21, p. 6041, 2020.

[24] V. Kakulapati, R. S. Sandeep, and V. Kranthikumar, "Predictive Analytics for early Detection of COVID-19 by fuzzy logic," in *Decision Sciences for COVID-19*, pp. 45–65, Springer, 2022.

[25] A. I. Paganelli, P. E. Velmovitsky, P. Miranda et al., "A conceptual IoT-based early-warning architecture for remote monitoring of COVID-19 patients in wards and at home," *Internet of Things*, vol. 18, Article ID 100399, 2022.

[26] N. Bilandi, H. K. Verma, and R. Dhir, "An intelligent and energy-efficient wireless body area network to control coronavirus outbreak," *Arabian Journal for Science and Engineering*, vol. 46, no. 9, pp. 8203–8222, 2021.

[27] A. A. Baradaran and K. Navi, "HQCA-WSN: high-quality clustering algorithm and optimal cluster head selection using fuzzy logic in wireless sensor networks," *Fuzzy Sets and Systems*, vol. 389, pp. 114–144, 2020.

[28] S. Juneja, S. Kendre, and U. Patkar, "Healthcare analysis via wireless sensor network," *IJSRSET Journal*, vol. 2, no. 2, pp. 2395–1990, 2016.

[29] B. Ji, M. Zhang, L. Xing et al., "Research on optimal intelligent routing algorithm for IoV with machine learning and smart contract," *Digital Communications and Networks*, 2022.

[30] K. Vengatesan, A. Kumar, T. S. Subandh et al., "Secure Data transmission through Steganography with blowfish algorithm," in *International Conference on Emerging Current Trends in Computing and Expert Technology*, pp. 568–575, Springer, 2019.

[31] S. Savaşcı Şen, M. Cicioğlu, and A. Çalhan, "IoT-based GPS assisted surveillance system with inter-WBAN geographic routing for pandemic situations," *Journal of Biomedical Informatics*, vol. 116, Article ID 103731, 2021.

[32] R. Singla, N. Kaur, D. Koundal, S. A. Lashari, S. Bhatia, and M. K. Imam Rahmani, "Optimized energy efficient secure routing protocol for wireless body area network," *IEEE Access*, vol. 9, pp. 116745–116759, 2021.

[33] T. Saba, K. Haseeb, I. Ahmed, and A. Rehman, "Secure and energy-efficient framework using Internet of Medical Things for e-healthcare," *Journal of Infection and Public Health*, vol. 13, no. 10, pp. 1567–1575, 2020.